ENERGY HARVESTING FROM HUMAN PASSIVE POWER

by

Mª Loreto Mateu Sáez

A dissertation submitted in partial fulfillment
of the requirements for the degree of

Doctor in Electronic Engineering
in the

Electronic Engineering Department

of

Universitat Politècnica de Catalunya

Thesis Advisor: Francesc Moll Echeto

2009

High Performance Integrated Circuits
Design Group
UNIVERSITAT POLITÈCNICA DE CATALUNYA

ENERGY HARVESTING
FROM HUMAN PASSIVE POWER

by
M.ª Loreto Mateu Sáez

Thesis Advisor: Dr. Francesc Moll

A dissertation submitted in partial fulfillment
of the requirements for the degree of
Doctor in Electronic Engineering
in Universitat Politècnica de Catalunya
2009

to my parents, Isabel and Josep, and to Duncan

ACKNOWLEDGEMENTS

I would like to thank first of all my thesis advisor, Dr. Francesc Moll, for all his support, motivation and exchange of ideas during these years. I would like to thank Ferran Martorell for listening to my ideas and for contributing with his own ideas during all the thesis and also for his unconditional support; and to the rest of the persons of the High Performance Integrated Circuits and Systems Design Group. I would also like to thank all the people of the Fraunhofer Institut Integrierte Schaltungen in Nurenberg, Germany, and specially to: Néstor Lucas, Cosmin Codrea, Javier Gutierrez, Markus Pollak, Santiago Urquijo, Peter Spies and Günter Rohmer for their support and cooperation in the accomplishment of this thesis. I would also like to thank Carlos Villavieja for helping me with the acceleration measurements here presented.

I express my thanks also to the Universitat Politècnica de Catalunya for giving me a UPC research grant for doing my PhD.

Contents

List of Figures

Part I

General Discussion

Chapter 1

Motivation and Objectives

This thesis deals with the topic of energy harvesting (also called energy scavenging) that is defined as the process by which energy is collected from the environment employing a generator that transforms the input energy into electrical energy to power autonomous electronic devices. A self-powered system based on environment energy harvesting is composed of several components, see Figure 1.1, that are:

- Energy transducer (also called energy harvesting generator), used to convert some available ambient energy into electrical energy. The environmental energy sources available for conversion may be thermal (thermoelectric cells), light (photovoltaic cells), RF (rectifying antennas), and mechanical (piezoelectric, magnetic induction, electrostatic converters).
- Storage capacitor. Some of the above energy transducers do not provide DC current, and in this case it is necessary to rectify the current and accumulate the energy into a capacitor.
- Voltage regulator, to adapt the voltage level to the requirements of the powered device.
- Optional battery, depending on the requirements of the application. In some applications the powered device can be completely switched off during certain intervals and a battery is not necessary, while in others a permanent powering is mandatory. In any case, this battery will have a lower weight, volume and capacity than a battery that is expected to supply power to an electronic device without an energy harvesting generator. It depends on the requirements of the application if a capacitor can be used instead of a battery.
- Electronic device that typically has different power consumption modes. This fact allows to operate the device frequently in a low-power consumption mode and to operate it in active mode only during limited time periods to decrease its energy consumption.

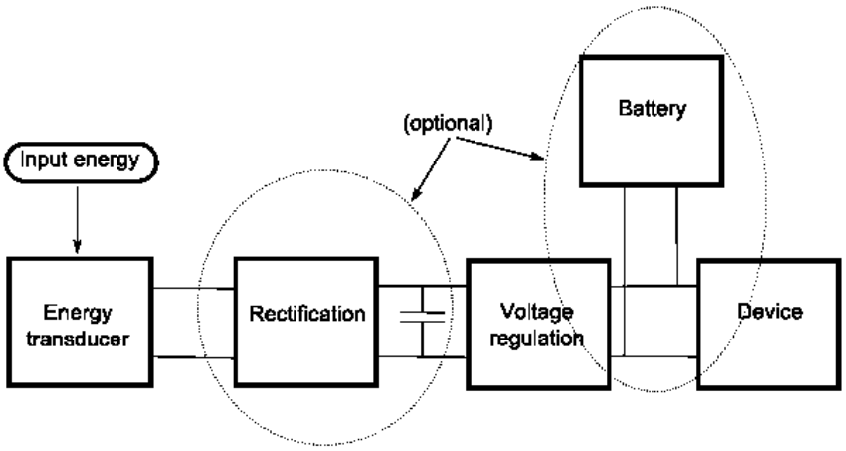

Figure 1.1: Schema of a generic self-powered device.

In this chapter, it is given the motivation of the thesis as well as the objectives accomplished. It also contains an introduction of the state of art of energy harvesting generators and energy storage elements.

1.1 Motivation

Portable equipments are the first evolution from fixed equipments that make possible that computers are part of our everyday lives. The trends in technology allow the decrease in both size and power consumption of complex electronic systems. This decrease in size and power rises the concept of wearable devices which are integrated in everyday personal belongings like clothes, watch, glasses, et cetera [4, 5]. The term wearable device receives several definitions in [4] and in the thesis is employed for a self-powered electronic device with low power consumption and communication capabilities integrated in smart clothes. Thus, if the complete energy harvesting system of Figure 1.1 would be integrated in clothes, it would be a wearable device.

Power supply is a limiting factor in wearable devices since the employment of a primary battery (a battery to be used only once) means that the user of the portable product has to carry an extra battery while the use of a secondary battery (rechargeable battery) means that the user has to plug in the portable product to grid to recharge it. This fact limits the mobility of the wearable device which is restricted to the lifetime of the battery. Furthermore, due to the costs and inaccessible locations, the replacement or recharging of batteries is often not feasible for wearable devices integrated in smart clothes. Moreover, the increasing number of battery-powered portable products is creating

an important environmental impact.

Wearable devices are distributed devices in personal belongings and thus, an alternative for powering them is to harvest energy from the user. Therefore, the power can be harvested, distributed and supplied over the human body. Wearable devices can create, like the sensors of a Wireless Sensor Network (WSN), a network called in this case, Personal Area Network (PAN) [6, 7], Body Area Network [8] or WearNET [9].

Nowadays, the main application for energy harvesting generators are Wireless Sensor Networks (WSNs) that harvest energy from the environment. There are several publications related with this topic [10–12]. Applications with very low power consumption electrical loads are the right ones to be powered by energy harvesting generators. The sensors that are part of a WSN can be powered using energy harvested from the environment. However, for powering wearable devices the human body seems to be a more trustworthy source since it is always available.

Electrical energy can be harvested from multiple sources (kinetic, solar, temperature gradient, et cetera). The physical principle of an energy harvesting generator is obviously the same no matter whether it is employed with an environmental or human body source. Nevertheless, the limitations related to low voltage, current and frequency levels obtained from human body sources bring new requirements to the energy harvesting topic that were not present in the case of the environment sources and that are mandatory to analyze properly. This analysis is the motivation for this thesis.

1.2 Objectives and Document Structure

The transducers (piezoelectric, electromagnetic and thermogenerator) and the electrical circuits used for conditioning the electrical energy in this thesis are well known. However, there is a gap between this specific and isolated knowledge and its application to the topic of energy harvesting from passive human power (see Section 2.2.2). An electrical model and the equations that govern the transducers operation are necessary when their energy source is the human body. The energy source must also be characterized and coupled to the transducer and this is the reason why the thesis is multidisciplinary, since in order to increase the efficiency of energy harvesting generators it is sometimes not only needed to improve the electric circuits but also the mechanical parts.

Furthermore, it is also necessary to characterize the electric output obtained from energy transducers. This output is a low power signal with a voltage in the order of units of volts and current in the order of units of microamps for piezoelectrics placed inside the insole of a shoe, hundreds of millivolts and units or tens of milliamps for thermogenerators, that employ the temperature gradient between human body and environment as thermal source, and tens or hundreds of millivolts and units of milliamps in the best case for inductive transducers.

In energy harvesting applications the control unit is powered with the harvested energy and this fact entails that no energy consuming control techniques

can be employed due to the low power levels harvested and that a starter circuit is mandatory to avoid the dependency on energy storage elements. Moreover, the electronic load operation must be adapted to the available energy. Thus, the dc-dc converter designed for the application with thermogenerators as energy harvesting transducers has been done taking these facts into consideration.

In energy harvesting applications, the energy harvested in a certain time is a more relevant magnitude than the instantaneous power harvested due to the discontinuous nature of energy harvesting sources. This is the reason for employing energy instead of power in most of the results of the thesis.

More specific objectives of the thesis for every component of the energy harvesting generator system are given in this section.

- A study of piezoelectric, inductive and thermoelectric generators that harvest passive human power is the main objective. A model of the complete energy harvesting system, including the transducer which is a component of critical importance, is necessary in order to simulate it and optimize its parameters [13]. This model can be done with electronic components and simulated with electronic simulators like SPICE or ADS. Alternatively, they can be described with hardware description language [14] like Verilog-A in combination with compatible simulators like SPICE or Spectre or using a generic system-level simulator, like Ptolemy [15]. Both Verilog-A and Ptolemy allow to simulate hybrid systems where mechanical and electrical disciplines are combined, like in our case of study. Therefore, it is necessary to obtain a model of the transducers with physical equations that describe how the input energy is converted into electrical energy.

- Before modeling the transducer, it is required to characterize them in a measurement stage. This stage is necessary for the comparison between measurements and simulations in order to evaluate the accuracy of the model. Furthermore, sometimes a measurement stage is required in order to extract the parameters employed in the model. The transducer is optimized for the activity from which the energy is harvested. Physical parameters of the transducers must be optimized in order to increase their efficiency. In summary, in the thesis, the following characterizations have been done:

  - voltage measurements of the energy harvesting generator based on piezoelectric films inserted inside a shoe,
  - acceleration measurements of different parts of the human body, for the case of the inductive transducers, in order to estimate the energy that can be harvested, the best location and the optimization of the energy harvesting generator,
  - voltage and current measurements at different temperature gradients to characterize the thermoelectrical generators.

- Increase of the mechanical coupling efficiency. Once the physical equations of the transducers are analyzed it can be studied if a better mechanical coupling between the transducer and the human body can be accomplished.

- Definition of the load requirements in terms of power consumption. The objective of the thesis does not include the design of the load to be powered by the energy harvesting generator. The data recollection of state of the art sensors and communication modules power consumption provides an idea about what can be done with the harvested energy. A wearable device can be composed by a sensor and a communication module (a microprocessor and a RF transceiver). Microprocessors and RF transceivers have different power consumption modes (sleep, standby, active,...). A model of the communication module in power consumption terms will determine an appropriate power consumption profile for the communication module, which ensures that the available energy harvested from the human body is enough to power it. Therefore, the model of the electronic load can be generated only taking into account the power consumption profiles of different working modes given by low power wireless communication modules [16, 17].

- The battery model. A battery or another storage element is used when permanent powering is mandatory. The objective in this field is simply the characterization of batteries using the battery model presented by Chen et al. [3].

- A more general objective and related with the different energy harvesting transducers and their locations on the human body is the quantification of the harvested energy. Once the energy is quantified, a further step is analyze what can be done with it.

1.3 Document Structure

The general objectives detailed above have been accomplished in the papers presented as part of the thesis.

* [18] provides several methods to design an energy harvesting device depending on the type of available energy. Nowadays, the trends in technology allow the decrease in both size and power consumption of complex digital systems. This decrease in size and power gives rise to new paradigms of computing and use of electronics, with many small devices working collaboratively or at least with strong communication capabilities. Examples of these new paradigms are wearable devices and wireless sensor networks. One possibility to overcome the power limitations of batteries is to harvest energy from the environment to either recharge a battery, or even to directly power the electronic device.

* In [19], the possibility to use piezoelectric film-bending beams inside a shoe in order to harvest part of the mechanical energy associated to walking activity is exposed. This study analyzes several bending beam structures suitable for the intended application (shoe inserts and walking-type excitation) and obtains the resulting strain for each type as a function of their geometrical parameters and material properties. As a result, the optimum structure for the application can be selected.

* [20] gives the optimal way to convert the mechanical energy generated by human activity (like walking) into electrical energy using piezoelectric films when it is collected in the form of charge accumulated in a storage capacitor. Under this scheme, the storage capacitor needs only to be connected to the load when it has enough energy for the requested operation. This time interval depends on several parameters: piezoelectric type and magnitude of excitation, required energy and voltage, and magnitude of the capacitor. This work analyzes these parameters to find an appropriate choice of storage capacitor and voltage intervals.

* [21] presents a study of a time-domain model of a magnetic induction microgenerator for energy harvesting applications. The model is based on a simple structure for which an analytical expression of the magnetic field distribution can be computed. From this analytical expression, geometric parameters that are not taken into account in the previous literature on microgenerators are considered. Starting from the magnetic field distribution in space of a circular current loop, the paper derives the induced electromotive force in a coil depending on the distance to the magnet. Simulations give insight into the validity of linear models implicitly assumed in frequency domain analysis of these systems.

* In [22], a low temperature thermal energy harvesting system to supply power to wireless sensing modules is introduced. The thermoelectric generator module (TEG) makes use of the temperature gradient between the human body (the heat source) and the ambient to deliver a low voltage output that is up converted by means of a power management circuit. This regulated power source is able to reliably supply a wireless communication module that transmits the collected temperature, current and voltage measurements.

* [13] presents a complete system simulation of a self-powered sensor. The components are described with the Verilog-A language, that allows a behavioral description based on the most important characteristics. The simulations here shown compare a battery-less versus a battery-powered RF transmitter module, in both cases with a piezoelectric device generating electrical energy. Results show how design choices of the system change the periodicity of the transmission and the ability to recharge the battery.

Chapter 2 is a summary of the state of the art of energy harvesting generators and their applications. This summary is centered in different kinds of energy harvesting generators with a classification that distinguishes between those that harvest the energy from the human body and those that harvest the energy from the environment. The state of the art of energy storage elements is also included in this chapter.

The results obtained during the realization of this thesis are highlighted and analyzed in Chapters 3 through 6 and Appendixes A through F. Thus, Chapter 3 presents the study of piezoelectric generators. An electromechanical model is obtained from constitutive piezoelectric equations for the case of PVDF piezoelectric material. Additional information related with piezoelectric constants and the electromechanical piezoelectric model is given in Appendixes A, B and C. It is analyzed how to maximize the electrical energy converted during walking activity and therefore, the use of bending beam structures is introduced . The contribution of the physical dimensions and constants of the material in the acquisition of the converted electrical energy is also analyzed. The direct discharge circuit is employed for walking activity and the calculation of the optimum storage capacitor is pursued in this chapter.

Chapter 4 presents acceleration measurements of the human body which are expanded in Appendix D. The setup employed for obtaining the measured data is presented as well as the calibration procedure done. These measurements were done in order to have real data to employ as input for the simulation of an inductive generator in the time domain. A comparison between the energy harvested from the different parts of the human body analyzed is done. Moreover, the values of the parameters of inductive generators that harvest more energy are analyzed.

Chapter 5 is focused on TEGs. First, a theoretical analysis and an equivalent circuit with the thermal and electrical parts is presented. Afterwards, the characterization of some TEGs and the calculation of their parameters, employed for the electrical model of TEGs, is shown and extended results are available in Appendix E. This characterization and the knowledge of the TEG parameters are used for the design of the power management unit which deals with low input voltages for indoor applications. A power management circuit that works with temperature gradients in the range of 3 K-5 K is introduced and characterized.

In additon, Chapter 6 explains the methodology employed to create an analytical model and simulate a complete energy harvesting system. In an energy harvesting system that employs an energy storage element, it can be calculated the minimum size of the energy storage element (e.g. named as capacity for the batteries) to assure that no energy generated by the energy harvesting power supply is going to be wasted. Moreover, the minimum amount of energy that must have the energy storage element to assure proper operation is also calculated.

Finally, Chapter 7 summarizes the conclusions obtained for the appropriate design of an energy harvesting generator from human body. In addition, an explanation about when a battery-less application is possible and when a

battery-powered application is necessary are given. The differences to take into account in the design of energy harvesting generators powered by environmental sources and by human body are included in this final chapter. The feasibility to integrate energy harvesting generators based on human power is also discussed.

Appendixes A, B and C are related with the topic of piezoelectric transducers. Appendix A contains the theoretical analysis of the relation between the piezoelectric constants calculated from the piezoelectric constitutive equations. Appendix B contains the same analysis applied to PVDF and ceramic piezoelectric materials for different working modes. Moreover, the working mode that harvests more energy is deduced as well as its relation with the dimensions of the material and their piezoelectric constants. Appendix C gives a detailed analysis of the electromechanical coupling circuits for PVDF piezoelectric materials in working modes 31 and 33 employing to sets of state variables: $\{F, \nu, V, I\}$ and $\left\{T, \dot{S}, E, \dot{D}\right\}$.

Appendix D shows additional acceleration measurements on the human body and its frequency spectrum.

Appendix E contains voltage measurements obtained for different thermogenerators connected to several resistors at different temperature gradients. Moreover, the Seebeck coefficient and the internal resistance have been calculated at different temperature gradients.

Appendix F shows the measurements done and results obtained to characterize a Lithium polymer battery employing the model presented by Chen et al. in [3].

Chapter 2

State of the art

2.1 Energy Harvesting Generators

There are several ways to convert different kinds of energy into electrical energy. This conversion is made by energy harvesting generator systems. In this section, the most usual types of conversion are presented and classified by the kind of energy harvesting transducer employed: solar cells, electromagnetics, electrostatics, piezoelectrics and thermoelectrics. Another classification that distinguishes between energy harvesting applications powered by environmental sources and by human body is made in Section 2.2.

2.1.1 Photovoltaic Cells

Light is an environmental energy source available to power electronic devices. A photovoltaic system generates electricity by the conversion of light into electricity. Photovoltaic systems are found from the megawatt to the milliwatt range producing electricity for a wide number of applications: from grid-connected PV systems to wristwatches. The application of photovoltaics in portable products could be a valid option under the appropriate circumstances.

The power conversion efficiency of a PV solar cell is defined as the ratio between the solar cell output power and the solar power (irradiance) impinging the solar cell surface. For a solar cell of 100 cm^2, 1 W can be generated, if the solar irradiation is 1000 W/m^2 and the efficiency of the solar cell is 10%. The PV solar cells have a lifetime around 20-30 years.

Outdoors, the solar radiation is the energy source for PV system. Solar radiation varies over the earth's surface due to the weather conditions and the location (longitude and latitude). For each location exists an optimum inclination angle and orientation of the PV solar cells in order to obtain the maximum radiation over the surface of the solar cell [23].

M. Veefkind et al. presented the Solar Tergo prototype, a charger for small portable products such as mobile telephones and MP3 players, for use in combination with a backpack. The Solar Tergo consists of PV cells and a cell battery

pack [24, 25].

UCLA University has developed a solar harvesting module to power sensor nodes called Heliomote. This module can power the most commonly sensor nodes like Crossbow's Mica2 and MicaZ. Heliomote employs commercial solar panels to harvest energy and manages the storage and the use of the harvested energy. The energy demands of sensors are adapted to the available energy [26]. A commercial edition of Heliomote is now available in ATLA Labs [27].

Solar energy is also a valid power source for pacemakers, and other implants and biosensors. Actual devices use lithium based batteries that power during a limited period, three years, the devices. The Instituto de Energa Solar from Unviersidad Politcnica de Madrid and the Grupo de Dispositivos Semiconductores from Universitat Politcnica de Catalunya have designed a system to power this class of devices with solar energy. The system consists on an optical fiber that is placed under the skin in an accessible situation by the sun. The optical fiber goes to the the implant in which it is placed a PV cell [28].

Nowadays, a new technology of solar cells is being developed. At the moment, solar power has required expensive silicon-based panels that produce electricity four to ten times more costly than conventional power plants. The new technology of solar cells provides cheap and flexible solar cells. Advances in material science, including nanomaterials, is the base of printable solar cells. General Electric, Konarka technologies, Nanosolar, Siemens and STMicroelectronics are working in the revolution of solar cells. Konarka is producing strips of flexible plastic that are converting the light into electricity. Siemens predicts that in a short period of time their printable solar cells will have an efficiency of 10%. Nanosolar is developing the idea of spraying nano solar cells onto almost any surface. This technology could enable Nanosolar to spray-paint photovoltaics onto building tiles, vehicles,etc. and wire them up to electrodes [29].

Power density of photovoltaic cells in indoor environments is lower than 10 $\mu W/cm^2$ which is a low value compared with other energy harvesting sources [11]. Moreover, long dark periods imply the need of an energy storage element since there is not enough power to operate the load continuously. Moreover, the capacity of the energy storage element is related to the time between operations of the electronic load [18, 30].

2.1.2 Mechanical Energy Harvesting Transducers

The principle behind kinetic energy harvesting is the displacement of a moving part or the mechanical deformation of some structure inside the energy harvesting device. This displacement or deformation can be converted to electrical energy by three different methods, that are explained in subsequent subsections: inductive, electrostatic and piezoelectric conversion.

Each one of these transducers can convert kinetic energy into electrical energy with two different methods: inertial and non-inertial transducers. Inertial transducers are based on a spring-mass system. In this case, the proof mass vibrates or suffers a displacement due to the kinetic energy applied. The energy obtained will depend on this mass, and therefore this type is called inertial

converters. Mitcheson et al. have classified inertial converters in function of the force opposing the displacement of the proof mass [31]. These converters resonate at a particular frequency and many of them are designed to resonate at the frequency of the mechanical input source at input mechanical vibrations frequency since at this frequency (resonance frequency), the energy obtained is maximum. However, as the converters are miniaturized to integrate them on microelectronic devices, the resonance frequency increases, and it becomes much higher than characteristic frequencies of many everyday mechanical stimuli associated to human body. For example, typical acceleration frequencies of the human body in movement are below 20 Hz [32].

For non-inertial converters, an external element applies a pressure that is transformed into elastic energy, causing a deformation that is converted to electrical energy by the converter. In this case, there is no proof mass and the obtained energy depends on mechanical constraints or geometric dimensions [19]. The following sections give an overview of inductive, electrostatic and piezoelectric inertial generator whereas the case of non-inertial piezoelectric generator is detailed in Section 2.2.2.

Inductive (micro)Generators

Inductive generators are also called Voltage Damped Resonant Generators (VDRG). This transducer is based on Faraday's Law. The analysis of an inductive generator in the frequency domain is given in [31].

Table 2.1 shows a summary of inductive inertial generators with the reference of the design, the frequency and amplitude of the mechanical input, the output power generated at a certain output voltage and the dimensions of the transducers.

Table 2.1: Summary table of Inductive Inertial Generators.

Design Author	Mechanical excitation	Output power	Dimensions
Williams et al. [33]	$f = 4\ kHz$ Amplitude = 300 nm	$0.3\mu W$	mm^3
Li et al. [34]	$f = 64Hz$ Amplitude = $1000\mu m$	10 μW @ 2 V	$1cm^3$
Ching et al. [35]	$f = 104Hz$ Amplitude = $190\mu m$	5 μW	-
Amirtharajah et al. [36]	$f = 2\ Hz$ Amplitude = 2 cm	400 μW @ 180 mV	-
Yuen et al. [37]	$f = 80\ Hz$ Amplitude = 250 μm	120 μW @ 900 μV	2.3 cm^3

Electrostatic (micro)Generators

The physical principle of electrostatic generators is based on the fact that the moving part of the transducer moves against an electrical field, thus generating electrical energy. The energy conversion principle of electrostatic generators is summarized in [31].

Electrostatic generators are also called Coulomb-damped resonant generators (CDRGs) based on electrostatic damping. Meninger et al. present an electrostatic generator that employs a variable micro-machined capacitor with two different designs: a parallel capacitor operated with a constant charge and a comb capacitor operated with a constant voltage [38]. If the charge on the capacitor is maintained constant while the capacitance decreases (reducing the overlap area of the plates or increasing the distance between them), the voltage will increase. If the voltage on the capacitor is maintained constant while the capacitance decreases, the charge will decrease. The mechanical energy converted into electrical energy is greater when the voltage across the capacitor is constrained than when the charge across the capacitor is constrained. However, the initial voltage source needed to place an initial charge on the capacitor plates has a smaller value, if the charge across the capacitor is constrained. A way to increase the electrical energy for the charge constrained method is adding a capacitor in parallel with the MEMS capacitor. The disadvantage of this solution is that the initial voltage source has to increase its value. The energy is transduced through a variable capacitor and generates 8 μW from a 2,520 Hz excitation input [38]. Roundy et al. called this topology in-plane overlap converter since the capacitance variation is produced by the change in the overlap area of the interdigitated fingers [39,40]. When the plate moves, the capacitance changes as a consequence of the overlap area of the interdigitated fingers. Roundy et al. designed three different topologies of a MEMS CDRG with constant charge [41].

Table 2.2 shows a summary of electrostatic inertial generators with the reference of the design, the frequency and amplitude of the mechanical input, the output power generated at a certain output voltage and the dimensions of the transducers.

Table 2.2: Summary table of Electrostatic Inertial Generators.

Design Author	Mechanical excitation	Output power	Dimensions
Meninger et al. [38]	$f = 2.52\ kHz$	$8\mu W$	$0.075\ cm^3$
Sterken et al. [42]	$f = 1,200Hz$ Amplitude = 20 μm	100 μW@2V	-
Miyazaki et al. [43]	$f = 45\ Hz$ Amplitude = 1 μm	120 nW	-

Piezoelectric Generators

Piezoelectric materials are materials that are physically deformed in the presence of an electric field or that produce an electrical charge when they are mechanically deformed. Piezoelectric generators combine most of the advantages of both inductive and electrostatic generators. However, piezoelectric converters are difficult to implement on micromachined processes.

S. Roundy designed and fabricated a bimorph PZT generator with a steel center shim [12]. The cantilever structure has an attached mass and the volume of the total structure is 1 cm^3. A model of the developed piezoelectric generator was made and validated (Design 1). For an input vibration of 2.25 m/s^2 at about 120 Hz, power from 125 μW to 975 μW was generated depending on the load. More piezoelectric inertial generators are summarized in Table 2.3 where the mechanical excitation is described in terms of its frequency and acceleration.

Table 2.3: Summary table of Piezoelectric Inertial Generators.

Design Author	Mechanical excitation	Output power	Dimensions
S. Roundy et al. [12] Design 1	$a = 2.25\ m/s^2$ $f = 85\ Hz$	207 μW @ 10 V	1 cm^3
S. Roundy et al. [12] Design 2	$a = 2.25\ m/s^2$ $f = 60\ Hz$	335 μW @ 12 V	1 cm^3
S. Roundy et al. [12] Design 3	$a = 2.25\ m/s^2$ $f = 40\ Hz$	1700 μW @ 12 V	4.8 cm^3
H. Hu [44]	$a = 1\ m/s^2$ $f = 50\ Hz$	246 $\mu W/cm^3$ @ 18.5 V	-

A comparison between piezoelectric, electrostatic and inductive inertial transducers is given in [12]. Piezoelectric and inductive transducers don't need an external voltage source while the electrostatic does. However, the voltage levels obtained with electromagnetic generators are in the order of hundreds of millivolts. Another advantage of piezoelectric transducers is that the output voltage obtained is large enough to not need a transformer like in the case of inductive transducers. However, piezoelectric transducer is the most difficult to integrate on chip whereas electrostatic is the easiest to integrate on chip [12]. Roundy et al. compare also these three kinds of transducers from the point of view of the energy storage density obtained and the results show that the values for piezoelectric generators are greater than for the other generators [11].

Ottman et al. presented a circuit with a piezoelectric element connected to a diode bridge with a tank capacitor wired to a switch-mode dc-dc converter. An analysis is realized in order to obtain the optimal duty cycle of the converter that maximizes the harvested power of the piezoelectric element. This power management unit was designed for recovering energy from environmental vibrations. The use of the proposed system increases the harvested power by 325 % as compared to when the battery is directly charged with the piezoelectric rectified source. In the analysis done the piezoelectric source is supposed to

be a sinusoidal waveform. The switch-mode dc-dc converter is placed in order to control that voltage across the tank capacitor will be the optimum value to ensure that energy transferred from the piezoelectric element to the charging battery is maximum [45,46]. Mitcheson et al. describe different power processing circuits for electromagnetic, electrostatic and piezoelectric inertial energy scavengers [47]. A complete explanation for the power management unit presented in [47] for the case of electrostatic energy scavengers is given in [48].

2.1.3 Thermogenerators

Figure 2.1 illustrates a thermoelectric pair (thermocouple). The thermoelectric module consists of pairs of p-type and n-type semiconductors forming thermocouples that are connected electrically in series and thermally in parallel. The thermogenerator, based on the Seebeck effect, produces an electrical current proportional to the temperature gradient between the hot and cold junctions. The output voltage obtained for N thermocouples is N times the voltage obtained for a single thermocouple whereas the current is the same as for a single couple [49, 50]. The Seebeck coefficient is positive for p-type materials and negative for n-type materials. The heat that enters or leaves a junction of a thermoelectric device has two reasons: the presence of a temperature gradient at the junction and the absorption or liberation of energy due to the Peltier effect [49].

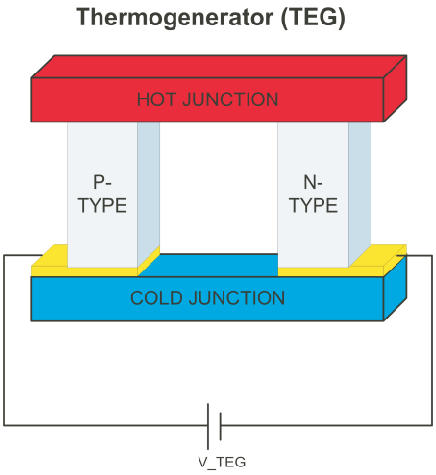

Figure 2.1: Thermoelectric module.

The figure of merit of thermoelectric modules, Z, is a measure of the cross-effect between electrical and thermal effects that takes place in TEGs (see Chapter 5). The figure of merit is sometimes represented multiplied by the temperature, ZT. A large value of ZT corresponds to a high efficiency in the conversion

of thermal to electric power [49,51]. Ryan et al. predict a specific power around 0.5 W/cm^2 for a 10 K temperature gradient at room temperature with a figure of merit, ZT, equal to 0.9 [51]. Starner [52] estimates that the Carnot efficiency at this temperature conditions is 5.5%. Thermoelectric microconverters are expected to provide milliwatts of power at several volts. Microconverters can be employed to convert rejected heat to electric power, providing electric power and passive cooling at the same time. Ryan et al. also expound that manipulating electrical and thermal transport on the nanoscale it is possible to improve conversion efficiency and ZT is predicted to increase by a factor of 2.5-3 near room temperature [51].

Carnot efficiency sets an upper theoretical limit to the heat energy that can be recovered. The human body is a heat source and the temperature gradient between the body and the environment, e.g. room temperature (20°C), can be employed by a TEG to obtain electrical energy. In a warmer environment the Carnot efficiency drops while it rises in a colder one. The previous calculations are made assuming that all the heat radiated by the human body can be recovered and transformed into electrical power, so that the obtained power is overestimated. A further issue of interest is the location of the device dedicated to capture human body heat. Starner recommends the neck as a good location for the TEG since it is part of the core region, those parts of the body that always must be warm. Moreover, the neck is an accessible part of the body and the engine can be easily removed by the user without creating discomfort. It is estimated that approximately a power between 0.2W-0.32W could be recovered by a neck brace.

Leonov et al. presented a thermal circuit used for modeling a TEG with multiple stages placed on the skin [53, 54]. Moreover, their analysis is oriented to the necessity of thermal matching between the TEG and the environment to obtain output voltages around 1 V with electrical matched load.

Stordeur and Stark developed in 1997 a Low Power Thermoelectric Generator (LPTG) for the D.T.S. GmbH company [55]. The LPTG of D.T.S. is a small compact thermoelectric generator whose output is compatible to the requirements of micro electronic systems in terms of dimensions and output power. The working range of LPTG is near room temperature with hot side temperature of the TEG not higher than 120°C. The LPTG provides a power output of 20 μW and a voltage of about 4 V under load at ΔT=20K [56]. A new approach was presented two years after the previous work that is capable of converting 15 $\mu W/cm^2$ from a 10 K temperature gradient [57]. Other energy harvesting TEGs are presented in Table 2.4 including applications oriented to energy harvesting from human body that are more detailed in Section 2.2.2.

Several power management methods can be employed with TEGs. A boost converter or a charge pump [62, 63] is usually necessary due to the low output voltage of TEGs (in the range of mV) in applications with temperature gradients around 5K at room temperature. Higher output voltages can be obtained connecting more thermocouple of the TEG in series but this involves an increase in its size.

Table 2.4: Summary table of Thermogenerators

Author	Output power	ΔT	Absolute temperature
Stordeur et al. [56]	20 μW@4 V	$20K$	room temperature to 120°C
Stordeur et al. [57]	15 $\mu W/cm^2$	$10K$	-
Stevens [58]	-	10 K	-
Seiko [59, 60]	1.5 μW@1.5 V	$1-3$ K	-
ThermoLife [61]	28 μW@2.6 V	$5K$	30°C
Leonov et al. [54]	250 μW 20 $\mu W/cm^2$@0.9 V	-	room temperature

2.1.4 Other Energy Harvesting Sources

Other ambient energy sources with their respective energy harvesting transducers like RF sources [64, 65], air flow sources, triboelectricity, pressure variations or radioactive specks,are available. A. Lal and J. Blanchard harvest the energy released naturally by tiny bits of radioactive materials [66]. The designed device is called nuclear micro-battery and it is composed by a radioactive source and on top of it, a rectangular piezoelectric cantilever is placed. When electrons fly spontaneously form the radioactive source to the copper sheet , the cantilever is charged negatively whereas the radioactive source is charged positively. Then, the source attracts the cantilever. The top of the cantilever has piezoelectric material so the mechanical stress of the bend produces a voltage across the electrodes attached. When the cantilever bends to the point where the cooper sheet touches the radioactive source, electrons flow back to the source and the electrostatic attraction finishes. At this moment, the cantilever oscillates and produces a series of electric pulses.

Another possible source is triboelectricity. The charge process associated to triboelectricity can be produced by surface contact. The net charge obtained when two surfaces are separated is directly proportional to its surface contact. Moreover, the net charge obtained by a material is related to friction and the break of bonds that gives as result free electrons [67, 68].

2.2 Energy Harvesting Sources

A second classification of energy harvesting applications distinguishes between the source of energy: the environment or the human body. In this section, some energy harvesting systems are summarized and classified. An environmental energy source is usually employed to power Wearable Sensor Networks (WSNs) whereas human body power is used for supplying low power wearable devices, RF tags, networks of sensors distributed on smart textiles.

2.2.1 Environment

The application of a WSN will determine the energy source (solar energy, vibrations, thermal gradient,...) to use. The main environmental energy sources employed to supply power to WSNs are solar energy and mechanical vibrations. The main application of WSNs is to sense the environment in order to collect data that are employed to improve the comfort and health of intelligent buildings. One of the most famous WSNs hardware platforms is the Mica. Mica Motes are nodes created by Crossbow Technology Inc. [69]. These nodes employs TinyOS as operating system [70]. They are modular with a processing and communication board and a sensing board. The first board includes a microcontroller (μC), an antenna, a flash memory, a power connector , an expansion connector and a CC1000 single chip transceiver. The sensor board has a light sensor, a temperature sensor, a sounder, a microphone, a tone detector, an accelerometer and a magnetometer. All these motes are designed to be battery powered.

S. Roundy et al. estimated that assuming an average distance between wireless sensor nodes of 10 m, the peak power consumed by the radio transmission will be around 2 to 3 mW whereas the peak power consumed during the reception is less than 1 mW [11]. It is estimated a maximum peak power of 5 mW taking into account the processor and communication units as well as the sensing and peripheral circuitry. The microcontroller and the communication transceiver modules have low power consumption modes (sleep mode, standby mode, ...) where the power consumption is reduced to the range of tens of μW. Assuming that the nodes will be active 1% of the time, it is calculated an average power consumption around 100 μW. Taking into account this average power consumption, a Lithium battery of 1 cm^3 must be replaced once every nine months. Thus, batteries are not a recommended power source for wireless sensors since the power source would limit the lifetime of the sensor [40]. Energy harvesting generators that employ vibrational energy sources have a power density around 375 $\mu W/cm^3$. In the case of energy harvesting generators based on solar energy it is generated 15,000 $\mu W/cm^2$ and 10 $\mu W/cm^2$ for outdoor and indoor solar source [11].

2.2.2 Human body

A.J. Jansen employs the term human power as short for human powered energy systems in consumer products [71]. The Personal Energy System (PES) research group of the Delft University of Technology distinguishes between active and passive energy harvesting method. The active powering of electronic devices takes place when the user of the electronic product has to do a specific work in order to power the product that otherwise the user would not have done. The passive powering of electronic devices takes place when the user does not have to do any task different to the normal tasks associated with the product. In this case, the energy is harvested from the user's everyday actions (walking, breathing, body heat, blood pressure, finger motion, ...).

Active Human Power

Some examples of electronic devices supplied from active human power extracted for activities like pedaling, walking, ... are given in this section. The access to Internet via bicycle-powered computer and a Wi-Fi network from a Laos Village is presented in [72]. The computer is an ultra-efficient Linux PC that sends signals via a wireless connection to a solar-powered relay station. The PC power is supplied by a car battery charged by a person pedaling a stationary bike. 1 minute of pedaling generates around 5 minutes of power.

Windstream Power Systems Incorporated offers human power generators like MkIII, HPG MkIII which can be pedaled or cranked by hand and it can generate an average continuous power about 125 W by pedaling and 50 W by hand-cranking. The Bike Power Module consists on a generator, bearings, and frictional wheel all mounted on a steel bracket in order to generate 100-300 W [73].

T. Baylis designed a low cost radio, BayGen Freeplay, that worked on a hand crank. The BayGen Freeplay requires only a couple of human calories to work. If the user wind up to the hand crank during 30 seconds, the radio stores enough power in a fully wound-up spring to listen to the radio during 30 minutes [74]. Freeplay continued to develop their radio adding a capacitor and later a rechargeable batteries and solar panels [75]. The company also has introduced another products powered by arm motion while has continued innovating in the radio market [76]. Another portable radio powered by an alternative system is the Dynamo & Solar (D&S) radio, produced in China [77].

Another company offering human powered products is Atkin Design and Development, AD&D. Their prototype Sony radio delivers 1.5 hours play time for a 60 second wind. Their Motorola phone charger prototype provides 2 hours standby and 10 minutes talk time for every 60 seconds wind. The Professional torch model shine for 15 minutes on a 60 second wind and can be used as attachable charger unit for the radio and phone [78].

The Nissho's Allandinpower is a hand-powered device that one cranks by squeezing. It produces 1.6 W of power when the handle is squeezed at 90 times per minute. The device is capable of providing energy to general applications like a phone or flashlight. One minute of powering gives one minute of talk time when a mobile phone is powered [75, 79]. Nissho has also a stepcharger that is powered by the movement of the feet and can generate up to 6 W [75, 79]. Freeplay has also developed a similar product called Freecharge Portable Marine Power that can be also powered by solar and wind energy [76].

Passive Human Power

The option to parasitically harvest energy from everyday human activity (passive power) implies that an unobtrusive technique has to be adopted. Some passive human power generators are summarized in this section. Starner presented human power as possible source for wearable computers [52]. He analyzed power generation from breathing, body heat, blood transport, arm motion, typ-

ing, and walking and provides the power dissipated by the human body during several activities. A more recent study appears in [80] where it is explained the state of the art of passive human power to power body-worn mobile electronics.

Walking is one of the usual human activities that have associated more energy [52] and [81]. Piezoelectric materials, dielectric elastomers and rotatory generators have been employed in order to harvest energy from human walking activity.

The MIT Media Lab developed a full system that harvests parasitic power in shoes employing piezoelectric materials. The low-frequency piezoelectric shoe signals are converted into a continuous electrical energy source. The first system consisted on harvesting the energy dissipated in bending the ball of the foot, placing a multilaminar PVDF bimorph under the insole. The second one consisted on harvesting the foot strike energy by flattening curved, prestressed spring metal strips laminated with a semiflexible form of PZT under the heel. Both devices were excited under a 0.9 Hz walking activity. The PVDF stave obtained an average power of 1.3 mW in a 250 kΩ load whereas the PZT bimorph obtained an average power of 8.4 mW in a 500 kΩ load. Therefore, the electromechanical efficiency for the PVDF stave is 0.5% and for the bimorph is 20% [82].

Shenck et al. presented two electronic circuits to convert the electrical output of the piezoelectric element into a stable dc output voltage. The first circuit consisted on a diode bridge connected to the piezoelectric element to rectify its output. The charge is transferred to a tank capacitor since the moment that the charge exceeds a voltage value. At that moment the tank capacitor is connected to a linear regulator that provides a stable output voltage. In the second circuit, the linear regulator was substituted by a high-frequency forward-switching regulator in order to improve efficiency. The control and regulation circuitry was not activated until voltage across the tank capacitor, C_b, exceeded a certain voltage value. A starter circuit was included in order to accumulate charge on C_b while there was not enough charge to activate the switches of the circuit. The converter's electrical efficiency was 17.6% [83].

Dielectric elastomers are electroactive polymers (EAPs) that can produce electric power from human activity. The main development area of EAPs are artificial muscles since EAPs hold promise for becoming the artificial muscles of the future. The electrostatic forces due to the electrodes voltage difference squeeze and strech the film [84]. Dielectric elastomers can grow by as much as 400% of their initial size and produce electric power when working in generator mode. When a voltage is applied across the dielectric elastomer which is deformed by an external force, the effective capacitance of the device changes and with the appropriate electronic circuits, electrical energy is generated [85] following the same principles of electrostatic generators as explained in Section 2.1.2. The energy density of these materials is high, some of them can generate about 21 times the specific energy density of single-crystal piezoelectrics [84]. DARPA and the U.S. Army funded the development of a heel-strike generator based on dielectric elastomers to power electronic devices in place of batteries. The claimed power generated is 1 W during normal walking activity [85].

The Media MIT Laboratory also developed another technique for extracting energy from foot pressure: an electromagnetic generator. Kymissis et al. analyzed an electromagnetic generator made by the Fascinations Corp. of Seattle that was mounted in the outside of a shoe. The first design obtained an average power of 0.23 W in a 10 Ω load, which matched its impedance, for a 3 cm stroke which interferes with walking [86]. J.Y. Hayashida et al. present an unobtrusive magnetic generator system integrated into common footwear [87]. The average power obtained was 58.1 mW, with a peak power reaching 1.61 W, in a 47 Ω load. The width of the pulses is around 110 ms. The average power is lower than in the previous design due to the fact that for the 90% of the stride, no power is harvested by the generator.

T. von Büren et al. optimize inertial micropower generators also for human walking activity obtaining power densities in the range of $8.7 - 2100\ \mu W/cm^3$ depending on the kind of generator, its size and its location on the human body [88].

The number of commercial products that employ human power and more specifically arm motion has significantly increased since the 1990s. In 1992, Seiko introduced the Kinetic, a wrist watch powered by a micro generator that converts the motion of the watch while it is worn by its user into electrical energy stored in a capacitor. The idea was not new but Seiko improved the technology. The average power output generated when the watch is worn is 5 μW. However, when the watch is forcibly shaken, the power generated is 1 mW. After Seiko Kinetic, the Swatch Group launched another watch that is self-powered, the ETA Autoquartz Self-Winding Electric Watch that is discontinued since 2006 [89].

The Seiko Thermic watch, also discontinued, employs a thermoelectric generator to convert heat from the wrist into electrical energy. The watch absorbs body heat through the back of the watch. It was the first watch powered by energy generated between the body and environment temperature. The watch was first produced in December 1998 but nowadays it is no longer manufactured. The system consists on a thermoelectric generator converts the temperature difference into electricity to power the watch. The thermoelectric generator produces a power of 1.5 μW or more when the temperature difference is 1°C-3°C. A boosting and controlling circuit connects the thermoelectric generator to the titanium-based lithium-ion rechargeable battery of 1.5 V. The battery supplies power to the motors of the watch and the movement driver that controls them. For this device, Seiko Instruments Inc. developed at the time the world's smallest π-type Peltier cooling element [59].

Applied Digital Solutions (ADS) developed in 2001 a miniature thermoelectric generator that converts body heat flow into 1.5 V. The thermoelectric generator known as Thermo Life has several applications: attachable medical devices, electronic wrist watches, self powered heat sensors, and mobile electronics [90]. Thermo Life has a volume of 95 mm^3 and delivers with a $\Delta T = 5K$ a maximum power of $28\mu W$ at 2.6 V. The material employed for this TEG is Bi_2Te_3 which presents the best thermoelectrical properties to work in the range of room temperature [61].

Leonov et al. also showed an application where a watch-size thermoelectric wrist generator powers a radio transmitter [54]. It is also explained a simple thermal equivalent circuit for the TEG placed on the skin and different ways for increasing the output voltage given by the TEG. It is obtained a power of 250 μW which corresponds to about 20 $\mu W/cm^2$ when the output load matches the internal resistance of the TEG with $\Delta = 20K$. The open circuit voltage obtained with these conditions is 1.8 V (an output voltage of 0.9 V for a matched load). This result implies that more power per square centimeter can be generated with TEGs than with solar cells in indoor applications [54].

It can be concluded that some efforts have been done in the last years in the human passive energy harvesting topic. However, most of the work done in the energy harvesting field is related with harvesting energy from the environment instead of doing it from the human body. Moreover, an exhaustive formal analysis for the energy harvesting transducers that allows to increase the mechanical coupling with the human body and the electrical coupling with the power management unit is not available. The analysis of the energy harvesting transducers is centered on their formal equations and electrical equivalent circuits. Furthermore, an analytical study allows to generate a simulation environment for energy harvesting power supplies where it is possible to size the mechanical and electrical components as a function of the power requirements of the electronic load. In summary, the thesis deals with the energy harvesting topic from the formal side.

2.3 Energy Storage Elements

The two parameters employed to evaluate a storage element are energy and power density. Both of them are expressed in terms of weight or volume. Thus, energy density is the measure of the available energy in terms of weight (gravimetric energy density) or volume (volumetric energy density). The expression for gravimetric energy density is given by Equation (2.1) and for volumetric energy density by Equation (2.2):

$$\text{Gravimetric Energy Density} = \frac{\text{Capacity} \times \text{Nominal Voltage}}{\text{Cell Weight}} \tag{2.1}$$

$$\text{Volumetric Energy Density} = \frac{\text{Capacity} \times \text{Nominal Voltage}}{\text{Cell Volume}} \tag{2.2}$$

Therefore, the energy density defines the amount of energy that can be stored in a certain volume or weight whereas the power density is a measure of the speed of the energy storage element to be charged or discharged. High values of power density indicates that the charge and discharge of the energy storage element is fast whereas low values of power density indicates that the charge and discharge is slow. The ideal energy storage element must have both high energy and power density. In batteries, energy density is high whereas power density

is low. On the other hand, capacitors are the opposite case of batteries with high values of power density and low values of energy density. An alternative to capacitors and batteries are supercapacitors (or ultracapacitors) since they are a compromise between batteries and capacitors offering both a high energy and power density. Some gravimetric, volumetric energy density and power density values for secondary batteries, capacitors and supercapacitors are summarized in Table 2.5 [91, 92].

Table 2.5: Energy and power density of energy storage elements

Parameter	NiCd	NiMH	Li-ion	Capacitor	Supercapacitor
Volumetric Energy Density ($Whl^{-}1$)	90-150	160-310	200-280	-	-
Gravimetric Energy Density ($WhKg^{-}1$)	30-60	50-90	90-115	0.02-0.08	1-9
Gravimetric Power Density ($WKg^{-}1$)	150		1800	6000-8000	1000-7000

2.3.1 Batteries

Primary (non rechargeable) batteries compared to secondary (rechargeable) batteries are relatively long lasting. However, a large-scale adoption would result in important environmental issues. Rechargeable batteries require that the user can access to the electrical grid to recharge them which is not always available even in urban areas.

The demand of primary and secondary batteries is rising due to the generation of energy-hungry portable devices like digital cameras, camera phones, PDAs, etc. Lithium-ion (Li-Ion) batteries are nowadays (and probably also in the future) the secondary batteries leader of the market for powering portable devices. NiCd batteries market is shrinking and is being replaced by NiMH for environmental reasons [93].

Battery Terminology

Definitions concerning battery terminology are given to properly understand the behavior and characteristics of batteries [91, 93, 94]:

- Ampere-hour. It is the amount of electric charge carried by a current of 1 A flowing during 1 hour.
- Capacity (C) or Nominal Capacity (NC). It is the amount of charge expressed in Ampere-hour that can be delivered by a battery. It is usually specified at room temperature and at a low discharge current (0.1C).
- Charge rate. A charge or discharge current of a battery is measured in C-rate. A discharge current of 1C draws a current equal to the rated

capacity. For example, a battery rated at 1000mAh provides 1000mA for one hour if discharged at 1C rate.

- Cycle life. The number of cycles that a battery can be charged and discharged. Primary batteries or non-rechargeable batteries have a unitary cycle life whereas secondary batteries also called rechargeable batteries have a cycle life greater than one, dependent on the battery chemistry.

- Cut-off-voltage. The lowest voltage of a discharged battery. When the battery voltage is equal to this value, the discharge process has to finish to assure the integrity of the battery. It is also known as the end of discharge voltage (EODV) or the end of life (EOL) voltage by some manufacturers.

- Nominal voltage. The nominal voltage also called average discharge voltage is defined as the mid-point voltage of the battery voltage range during charge or discharge. For example, a battery with a voltage range of 1.8V to 2.8V has a nominal voltage of 2.3V.

- State of charge (SOC). Is the percentage of the maximum possible charge that is present inside the battery.

- Self-discharge. Capacity loss during storage due to the internal leakage. The self-discharge of Li-Ion batteries is not relevant.

It is usual to present the capacity of a battery in a figure where it appears the voltage as a function of the percentage of the nominal capacity for different discharge rate values, see Figure 2.2. The discharge curve of Li-Ion batteries can be considered flat during almost all the battery voltage range and is flatter for low discharge C-rates. Therefore, employing Li-Ion batteries the electronic device to power must tolerate less voltage variations of the supply source. For low discharge currents, the capacity of the battery is greater (an approximately equal to the nominal capacity of the battery) than for high discharge currents [95]. This unexpected variation of the energy dispensed by the battery as a function of the discharge C-rate is due to energy loss that occurs inside the battery and a drop in voltage that causes the battery to reach the low-end voltage cut-off sooner. The internal resistance of the battery is the cause of the discrepancy in the capacity for different discharge C-rates. If the battery has a low internal resistance, the differences in the nominal capacity for different discharge C-rates is in the range of only a few percentage points whereas if the battery has a high internal resistance, the difference in the capacity is around a 10 percent or more.

Another factor that has an influence over the battery capacity is the temperature. Temperatures near the room temperature (23 °C) with a discharge rate of 0.1C have a capacity around the 100 percent of the nominal capacity. For higher temperatures, the capacity is even greater than the 100 percent of the nominal capacity (but only a few percentage) whereas for lower temperatures, the capacity is reduced in the range of tens of percentage. However, using the batteries at high temperatures decreases their cycle life.

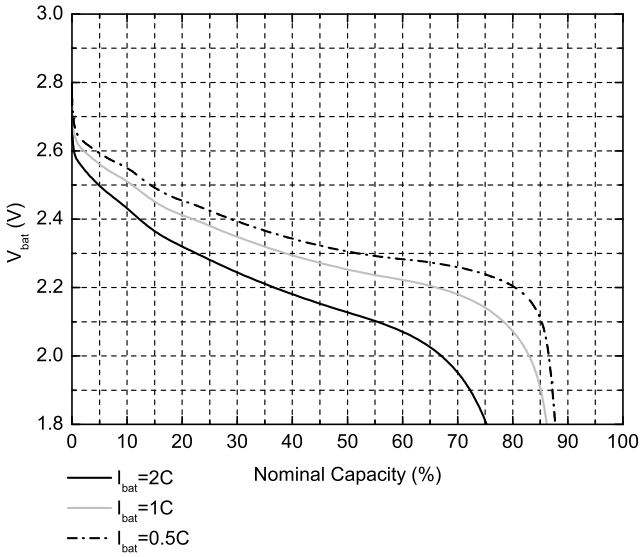

Figure 2.2: Li-Ion battery capacity for different discharge currents.

Battery Management

The behavior of batteries is characterized by the charge and discharge curves. There are several methods employed to charge and discharge batteries without damaging them. This section is focused in Li-Ion batteries since they are the most common rechargeable batteries for portable devices.

There are three different voltage regulator topologies to use in devices powered by batteries: switching regulators, linear voltage regulators and charge-pumps [96]. The use of linear voltage regulators is appropriate for batteries with a flat discharge curve during almost all the battery voltage range. Nevertheless, a higher conversion efficiency is obtained by switching regulators [97] in the case of batteries with steep discharge curves. For the case of Li-Ion batteries, discharge curves are more flat with low discharge currents than with high discharge currents, see Figure 2.2. There are also battery chargers for Li-ion batteries that employ charge-pump technique [98]. Moreover, switching regulators are very popular to recharge battery powered devices [97].

It is better for Li-ion battery partial discharge cycles than deep discharge cycles. Up to 1000 cycles can be achieved if the battery is only partially discharged. Besides cycling, the performance of the Li-ion is also affected by aging. Different discharge methods, notably pulse discharging, also affect the longevity of some battery chemistries. While NiCd and Li-ion are robust and show min-

imal deterioration when pulse discharged, the NiMH exhibits a reduced cycle life when powering a digital load [99].

2.3.2 Capacitors and Supercapacitors

The following table summarizes a comparison between batteries and capacitors.

Table 2.6: Comparison between batteries and capacitors

	Batteries	Capacitors
Advantages	+ High capacity	+ High power density
	+ Flat discharge curve	+ No charging circuit needed
Disadvantages	- Voltage as a function of chemistry	- Low energy density
	- Charging circuit needed	- Voltage proportional to the stored energy

Supercapacitors are rated in units of 1 F and higher. The gravimetric energy density is 1 to 10Wh/kg. This energy density is high in comparison to the electrolytic capacitor but lower than batteries. The supercapacitor provides the energy of approximately one tenth of the NiMH battery. Whereas the electrochemical battery delivers an almost constant voltage during the discharge cycle, the voltage of the supercapacitor drops linearly from full voltage to zero volts without the flat voltage discharge curve that characterizes most of chemical batteries. Due to this linear discharge behavior, the supercapacitor is unable to deliver the full charge to the load. The percentage of charge that is available to give depends on the supply voltage of the load to power [99].

A supercapacitor is modeled as a constant capacitor, C_o, with a parallel capacitor, C_u, which has a linear dependence on the voltage u. Two other parameters are conventional for a supercapacitor model. The first one is the series resistor, R_s that induces voltage drops during charge and discharge. Its value influences the energy efficiency of the component and its power density. The second conventional parameter is the leakage resistor, R_l that induces load losses when the component is in a stand-by mode [100].

Generally, the charge of supercapacitors is realized with a constant current from a dc voltage source. In particular cases, the charge, but most currently the discharge are realized with a constant power.

Table 2.7 summarizes the advantages and limitations of supercapacitors.

Table 2.7: Advantages and disadvantages of supercapacitors.

Advantages	Disadvantages
+ Virtually unlimited cycle life (not subject to the wear and aging experienced by the electrochemical battery).	- Unable to deliver the full energy stored since the voltage discharge curve is not flat.
+ Low impedance (enhances pulse current handling by paralleling with an electrochemical battery).	- Low energy density (typically holds one-fifth to one-tenth the energy of an electrochemical battery)
+ Rapid charging (low-impedance supercapacitors charge in seconds).	- Cells have low voltages (serial connections are needed to obtain higher voltages. Voltage balancing is required if more than three capacitors are connected in series).
+ Simple charge methods (voltage-limiting circuit compensates for self-discharge; no full-charge detection circuit needed).	- High self-discharge (the self-discharge is considerably higher than that of an electrochemical battery).
+ Cost-effective energy storage(lower energy density is compensated by a very high cycle count).	

Chapter 3

Piezoelectric Energy Harvesting Generator

Piezoelectric materials have multiple applications due to their properties. They are employed as sensors, actuators and energy harvesting generators. The piezoelectric effect was discovered by Jacques and Pierre Curie in 1880. Curie's brothers found that certain materials, when subjected to mechanical strain, suffered an electrical polarization that was proportional to the applied strain. If the electrodes are not short-circuited, a voltage associated with the charge appears. This is the piezoelectric effect used for mechanical to electrical energy conversion. Therefore, piezoelectrics are materials that allow conversion between mechanical and electrical energy. This property is used for harvesting energy from the environment. The materials which have this property also have the inverse piezoelectric effect that consists of the deformation of the material when an electrical field is applied.

There is previous research related with the topic of piezoelectric energy harvesting generators from different approaches. Applications for WSNs employ piezoelectric generators to convert mechanical vibrations to electrical energy at the resonance frequency of the piezoelectric material. Another approach is made by J. Paradiso et al. that transform the mechanical strain suffered by a piezoelectric material inserted inside a shoe into electrical energy [83]. Papers [13, 19, 20] focus on energy harvesting from walking activity since it has a high amount of energy associated [52, 80]. However, some of the results that appear in [13, 18–20] can be extrapolated to other mechanical activities associated with the human body (like the movement of the arm, knee, et cetera).

This section continues the approach to the generation of electrical energy from passive human power employing piezoelectric materials. Additional and extended results related with each paper presented in the thesis and related with this topic are included in this section.

3.1 Piezoelectric Equivalent Model

Section *4.2 Piezoelectric generator* [18] explains the piezoelectric effect and the piezoelectric constitutive equations employing Einstein notation. These general equations are expressed in a matrix form.

$$\begin{aligned} S_i &= s_{ij}^E T_j + d_{li} E_l \\ D_m &= \varepsilon_{mn}^T E_n + d_{mk} T_k \end{aligned} \qquad \text{for } i,j,k = 1,\ldots,6 \text{ and } l,m,n = 1,2,3 \tag{3.1}$$

There are three other ways to express the piezoelectric phenomenon. Each case differs from the others in the independent state variables and the piezoelectric constants employed:

$$\begin{aligned} S_i &= s_{ij}^D T_j + g_{li} D_l \\ E_m &= -g_{mk} T_k + \beta_{mn}^T D_n \end{aligned} \qquad \text{for } i,j,k = 1,\ldots,6 \text{ and } l,m,n = 1,2,3 \tag{3.2}$$

$$\begin{aligned} T_i &= c_{ij}^D S_j - h_{li} D_l \\ E_m &= -h_{mk} S_k + \beta_{ml}^S D_l \end{aligned} \qquad \text{for } i,j,k = 1,\ldots,6 \text{ and } l,m,n = 1,2,3 \tag{3.3}$$

$$\begin{aligned} T_i &= c_{ij}^E S_j - e_{li} E_l \\ D_m &= e_{mk} S_k + \varepsilon_{mn}^S E_n \end{aligned} \qquad \text{for } i,j,k = 1,\ldots,6 \text{ and } l,m,n = 1,2,3 \tag{3.4}$$

In these equations, T [N/m^2] is the applied mechanical stress matrix, E [N/C] is the applied electric field matrix, D [C/m^2] is the electric displacement matrix and S [m/m] is the mechanical strain matrix. Table 3.1 gives a definition of the piezoelectric constants employed in the four different piezoelectric constitutive equations shown. The bold characters are employed to represent the matrix notation. Comparing the four different possible ways to express the piezoelectric constitutive equations, the relations between the different constants of the piezoelectric materials can be obtained. These general relations are deduced in Appendix A and summarized in Table 3.2.

The relation between the piezoelectric constants depends on the kind of piezoelectric material employed and the direction of the mechanical stress and the electrical displacement as it is shown in Appendix B. Piezoelectric materials have different working modes related with the axis where the mechanical excitation and the electrical response are obtained. For example, working mode 31 corresponds to a mechanical excitation along axis 1 whereas the electrical response is obtained in the plane perpendicular to axis 3. Table 3.3 shows the relation between the piezoelectric constants for PVDF material in the particular case of working mode 31 that is deduced in Appendix B. In Table 3.3, it is introduced a new piezoelectric constant k_{31} that is the piezoelectric coupling constant for PVDF. Appendix B shows the piezoelectric constitutive equations for the specific case of PVDF and ceramic materials.

Table 3.1: Definition of the piezoelectric constants.

Constant	Definition	S.I. units
d, piezoelectric charge constant	Dielectric displacement developed when a mechanical stress is developed. E=constant	$\left[\frac{C}{N}\right]$
	Strain developed when an electric field is applied. T=constant	$\left[\frac{m}{V}\right]$
g, piezoelectric voltage constant	Electric field developed when a mechanical stress is applied. D=constant	$\left[\frac{Vm}{N}\right]$
	Strain developed when a dielectric displacement is applied. T=constant	$\left[\frac{m^2}{C}\right]$
e	Dielectric displacement developed when a mechanical strain is applied. E=constant	$\left[\frac{C}{m^2}\right]$
	Mechanical stress developed when an electric field is applied. S=constant	$\left[\frac{N}{Vm}\right]$
h	Electric field developed when a mechanical strain is applied. D=constant	$\left[\frac{V}{m}\right]$
	Mechanical stress developed when a dielectric displacement is applied. S=constant	$\left[\frac{N}{C}\right]$
$\mathbf{s}^E$, compliance	Mechanical strain developed when a mechanical stress is applied. E=constant	$\left[\frac{m^2}{N}\right]$
$\mathbf{s}^D$, compliance	Mechanical strain developed when a mechanical stress is applied. D=constant	$\left[\frac{m^2}{N}\right]$
ε^T, permittivity	Dielectric displacement developed when an electric field is applied. T=constant	$\left[\frac{CV}{m}\right] = \left[\frac{F}{m}\right]$
ε^S, permittivity	Dielectric displacement developed when an electric field is applied. S=constant	$\left[\frac{CV}{m}\right] = \left[\frac{F}{m}\right]$
$\mathbf{c}^E$	Mechanical stress developed when a mechanical strain is applied. E=constant	$\left[\frac{N}{m^2}\right]$
$\mathbf{c}^D$	Mechanical stress developed when a mechanical strain is applied. D=constant	$\left[\frac{N}{m^2}\right]$
β^T	Electrical field developed when a dielectric displacement is applied. T=constant	$\left[\frac{m}{CV}\right] = \left[\frac{m}{F}\right]$
β^S	Electrical field developed when a dielectric displacement is applied. T=constant	$\left[\frac{m}{CV}\right] = \left[\frac{m}{F}\right]$

Table 3.2: Relation between piezoelectric matrix constants.

Relation between piezoelectric constants
$[\mathbf{s}]^E = \left[\mathbf{c}^E\right]^{-1}$
$[\mathbf{d}] = \left[\mathbf{c}^E\right]^{-1}[\mathbf{e}] = [\mathbf{s}]^E[\mathbf{e}]$
$\left[\boldsymbol{\varepsilon}^{\boldsymbol{T}}\right] = \left[\boldsymbol{\beta}^{\boldsymbol{T}}\right]^{-1}$
$[\mathbf{d}] = \left[\boldsymbol{\beta}^T\right]^{-1}[\mathbf{g}] = \left[\boldsymbol{\varepsilon}^T\right][\mathbf{g}]$
$\left[\mathbf{s}^D\right] = \left[\mathbf{c}^D\right]^{-1}$
$[\mathbf{g}] = \left[\mathbf{c}^D\right]^{-1}[\mathbf{h}] = \left[\mathbf{s}^D\right][\mathbf{h}]$
$\left[\boldsymbol{\varepsilon}^S\right] = \left[\boldsymbol{\beta}^S\right]^{-1}$
$[\mathbf{e}] = \left[\boldsymbol{\beta}^S\right]^{-1}[\mathbf{h}] = \left[\boldsymbol{\varepsilon}^S\right][\mathbf{h}]$
$\left[\mathbf{s}^D\right] = \left[\mathbf{s}^E\right] - [\mathbf{d}]\left[\boldsymbol{\varepsilon}^T\right]^{-1}[\mathbf{d}]$
$\left[\mathbf{c}^D\right]^{-1} = \left[\mathbf{c}^E\right]^{-1} - [\mathbf{d}]\left[\boldsymbol{\varepsilon}^T\right]^{-1}[\mathbf{d}]$
$\left[\boldsymbol{\beta}^S\right]^{-1} = \left[\boldsymbol{\beta}^T\right]^{-1} - [\mathbf{d}]\left[\mathbf{s}^E\right]^{-1}[\mathbf{d}]$

Table 3.3: Relation between piezoelectric constants for PVDF in mode 31.

Relation between piezoelectric constants
$d_{31} = g_{31}\varepsilon_{33}^T$
$s_{11}^E = 1/c_{11}^E$
$d_{31} = e_{31}/c_{11}^E = e_{31}s_{11}^E$
$s_{11}^D = 1/c_{11}^D$
$g_{31} = h_{31}/c_{11}^D = h_{31}s_{11}^D$
$e_{31} = h_{31}\varepsilon_{33}^S$
$\varepsilon_{33}^S = \varepsilon_{33}^T\left(1 - d_{31}^2/\left(s_{11}^E\varepsilon_{33}^T\right)\right) = \varepsilon_{33}^T\left(1 - k_{31}^2\right)$
$s_{11}^D = s_{11}^E\left(1 - d_{31}^2/\left(s_{11}^E\varepsilon_{33}^T\right)\right) = s_{11}^E\left(1 - k_{31}^2\right)$

From the piezoelectric constitutive equations, an electromechanical model can be derived. This model consists of a circuit where mechanical and electrical variables present in the piezoelectric effect are related. Figures 3.1(a) and 3.1(b) show an electromechanical piezoelectric model presented in [101] and [102] where the state variables are F, ν, V, and I instead of the state variables (T, $\dot{S}$, E, and $\dot{D}$) employed in the model that appears in [18]. For example, Table 3.4 shows the relation between the variables that appear in Figure 3.1(a) and 3.1(b) and the piezoelectric constants for the particular working mode 31. Similar results can be obtained for other working modes and piezoelectric materials. A detailed analysis of the electromechanical piezoelectric model is done in Appendix C.

The analysis done gives as a result an electromechanical piezoelectric model that employs only electrical components (e.g. the force applied over the piezoelectric material is a voltage source). Thus, it is possible to use this model in an electrical simulator, like HSPICE, both the mechanical and the electrical part

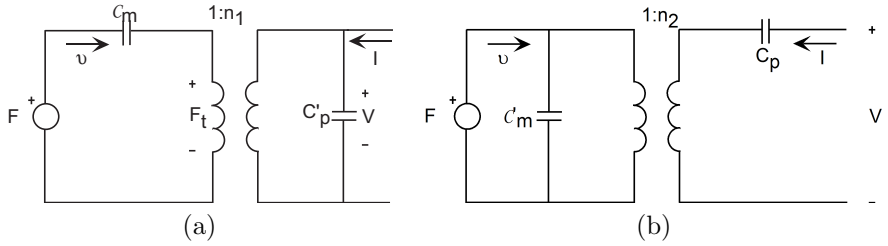

Figure 3.1: Piezoelectric coupling circuits, relating mechanical and electrical magnitudes.

Table 3.4: Relation between piezoelectric constants for PVDF in mode 31.

Relation between piezoelectric constants
$\mathcal{C}_{m31} = \frac{Ls_{11}^{E}}{Wt_c}$
$C'_{p31} = C_{p31} - \frac{d_{31}^2 L^2}{t_c^2 \mathcal{C}_{m31}} = C_p\left(1 - \frac{d_{31}^2}{s_{11}^{E}\varepsilon_{33}^{T}}\right) = C_{p31}\left(1 - k_{31}^2\right)$
$n_1 = \frac{V}{F_t} = -\frac{\mathcal{C}_{m31} t_c}{d_{31} L}$
$\mathcal{C}'_{m31} = \mathcal{C}_{m31}\left(1 - \frac{L^2 d_{31}^2}{t_c^2 C_p \mathcal{C}_{m31}}\right) = \mathcal{C}_{m31}\left(1 - k_{31}^2\right)$
$C_{p31} = \frac{\varepsilon_{33}^{T} A}{t_c}$
$n_2 = \frac{V_t}{F} = -\frac{d_{31} L}{t_c C_p}$

of the model.

3.2 Piezoelectric Bending Beam Analysis for Energy Harvesting using Shoe Inserts

This section summarizes and highlights the main results obtained in [19] where a study of different piezoelectric bending beams is done since different structures were not compared thoroughly before. One piezoelectric material that is suitable to be integrated in the insole of shoes and harvest energy from walking activity is a polymer called Polyvinylidene fluoride (PVDF) which is flexible and thus, easier to integrate in a shoe than piezoelectric ceramics. [19] exposes how to obtain the equations for PVDF from the piezoelectric constitutive matrix equation. The result obtained (that is well known) concludes that the efficiency for this material is greater in the working mode 31 than in the two other possible working modes (33 and 32). This fact motivates the analysis of different bending beam structures since the mechanical force exerted during walking activity for the heel of the foot is realized in direction 3 and therefore, bending beams structures are employed to cause a stress in direction 1.

The bending beam structures are analyzed from three different points of view:

- Support. Each end of the beam can be attached to one of the different types of existing supports which provide different reaction forces to the beam.

- Composite beams. A composite beam consists on piezoelectric and non piezoelectric material.

- Width of the beam. The shape of the width of the beam is another variable taken into account.

First of all, an homogeneous triangular and rectangular cantilever are compared and it is concluded that greater values are obtained with the first one in terms of maximum deflection and average strain. In addition, two different composite beams are introduced: the symmetric and asymmetric heterogeneous bimorph. From the comparison between the heterogeneous and homogeneous bimorphs, it is concluded that the most efficient vertical structure is the asymmetric heterogeneous bimorph with a large value of Y_s/Y_c.

The analysis of all the structures is made assuming that the maximum deflection is limited to a fix value D as can be seen in Figure 4 of [19]. Figures 7 and 8 in [19] show that the average strain in the case of the symmetric heterogeneous bimorph depends on the relation between the thickness of the piezoelectric and non-piezoelectric material but not on the relation between their Young's modulus. The average strain calculated in the case of the symmetric cantilever only takes into account a piezoelectric material thickness of $t_c/2$ whereas the average strain calculated for the asymmetric cantilever takes into account a piezoelectric material thickness of t_c. Therefore, with the appropriate electrical connection of the piezoelectric films, the results shown in the graph for the symmetric cantilever can be doubled.

A step forward is done the section titled *simply supported beam* of [19] to analyze the closer structure to the real case of placing piezoelectric films inside the insole of a shoe placed under the heel of the foot or even to increase the efficiency of placing the films in the beginning of the foot. Therefore, the structure analyzed is a simply supported beam with a distributed load q and rectangular width. The comparison shown in Figure 11 of [19] concludes that the simply supported beam with distributed load is the best of the structures analyzed. The case of simply supported beam with a distributed load q and triangular width was not analyzed in the paper and it is presented here.

3.3 Piezoelectric Beams Measurements

When a person is walking, running, et cetera, the beginning of the foot is stressed basically in direction 1 and thus, no additional mechanical structure is necessary to obtain a notorious improvement in the harvested energy of a piezoelectric material placed in this position. However, when the bimorph is placed in the heel of the shoe, a mechanical structure (a beam) is necessary to convert load force in direction 3 into mechanical stress in direction 1 (axial stress) when

walking activity takes place and therefore, to harvest more energy with each step.

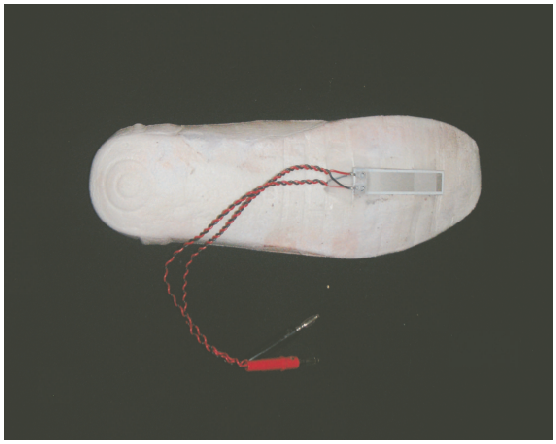

Figure 3.2: Position of the symmetric heterogeneous bimorph in the shoe.

Practical measurements were made employing a symmetric heterogeneous bimorph beam placed at different positions in the insole of a shoe. The beam has been placed at the beginning of the insole of the shoe (Figure 3.2), in the heel of the insole of the shoe (Figure 3.3) and in the same position but practicing a hole in the insole (Figure 3.4) to have the structure of a simply supported beam for testing the structure of a simply supported beam with distributed load.

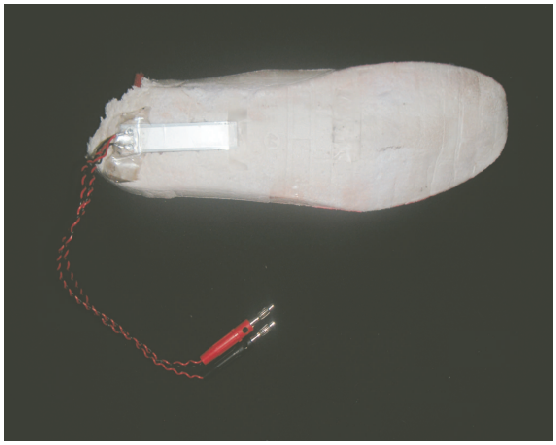

Figure 3.3: Position of the symmetric heterogeneous bimorph in the shoe.

Different usual activities (walking, running, descending and ascending stairs)

have been stored with the piezoelectric structure described employing a circuit designed to store the voltage signal generated by a piezoelectric film wired to a resistive load during 30 seconds [103]. Figures 3.11, 3.12 and 3.13 show the energy delivered to a 560kΩ resistor by a symmetric heterogeneous bimorph realizing these activities with piezoelectric films placed as appear in Figures 3.2, 3.3 and 3.4, respectively.

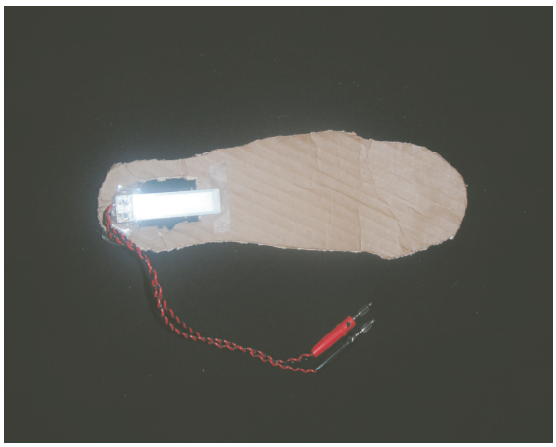

Figure 3.4: Position of the symmetric heterogeneous bimorph in the shoe.

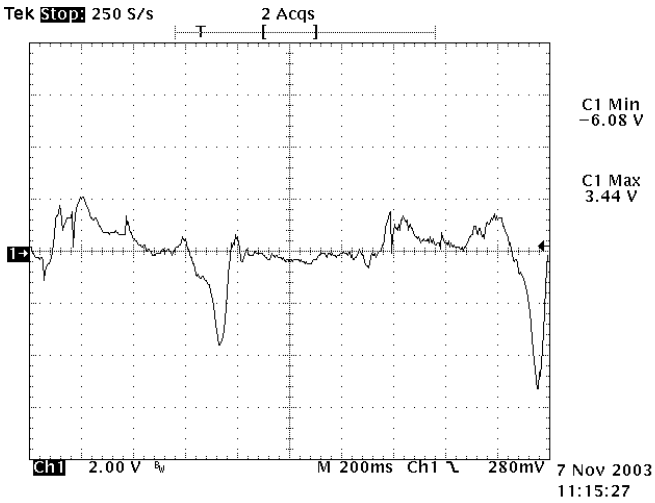

Figure 3.5: Voltage waveform of two piezoelectric films wired to a load of 100kΩ while a person is walking.

Figure 3.5 shows the voltage waveform obtained when two piezoelectric

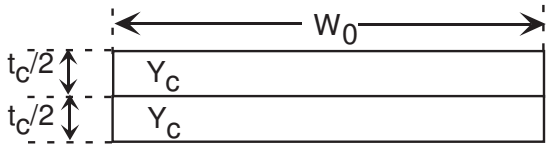

Figure 3.6: Cross section of a homogeneous bimorph beam. $t_c/2$ corresponds to a piezoelectric film thickness. Y_c is the Youngs modulus for the piezoelectric material. W_0 is the width of the beam. The neutral axis is placed between the two piezoelectric films.

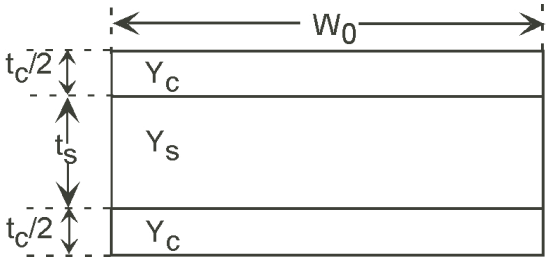

Figure 3.7: Cross section of symmetric heterogeneous bimorph beam. $t_c/2$ corresponds to piezoelectric film thickness whereas t_s corresponds to non-piezoelectric film thickness. Y_c is the Youngs modulus for the piezoelectric material, and Y_s is the Youngs modulus for the non-piezoelectric material. W_0 is the width of the rectangular beam.

films(homogeneous bimorph, see Figure 3.6) are placed at the beginning of a shoe and connected to a 100kΩ resistive load while a person is walking. It can be seen, that there are positive and negative parts in the waveform depending if the piezoelectric film is being compressed or tensed. The first positive part happens when the piezoelectric films are deformed but the foot is still on the ground whereas the first negative part occurs when the foot is already in the air and the piezoelectric films are relaxed (not suffering compression or tension). The second positive and negative peaks are always smaller than the first ones. The second positive peak occurs when the foot is placed again in the ground and the negative peak is the response to the relaxation of the piezoelectric films when the foot is still in the ground.

Figures 3.8, 3.9 and 3.10 show also the voltage waveform obtained but in this case with the storing device developed in [103] where the voltage waveform is stored after a diode bridge. Figure 3.8 is the voltage waveform obtained for the case of the heterogeneous symmetric bimorph placed at the beginning of the shoe. It can be seen in this figure that the period of the signal is approximately 1 second. Comparing Figures 3.9 and 3.10, it is deduced that higher voltages are obtained after employing a simply supported beam in the same location, the

heel of the shoe, and developing the same activity (walking).

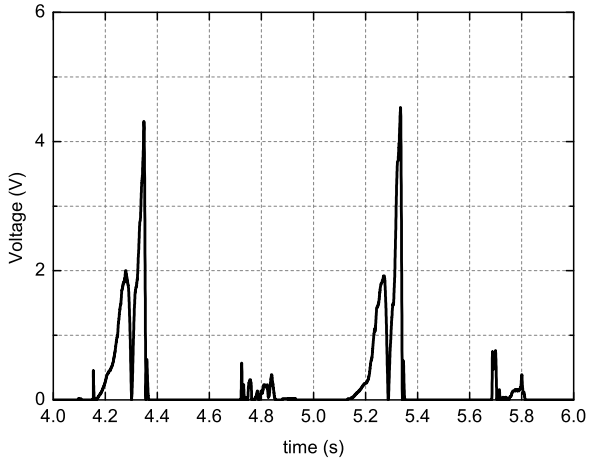

Figure 3.8: Voltage waveform of an heterogeneous symmetric bimorph placed at the beginning of a shoe with two piezoelectric films wired to a load of 560kΩ while a person is walking.

Figure 3.11 shows that the activity that delivers more energy placing the symmetric heterogeneous bimorph structure at the beginning of the shoe is running followed by walking whereas descending and ascending stairs are the activities that harvest less energy. The curves for ascending and descending stairs, see Figure 3.12, change their slopes at t=14s and t=12.5s, respectively, due to a displacement at the location of the beam structure. Similarly, in Figure 3.13 the walking waveform also has a change in its slope at t=12.5s.

3.4 Conclusions of the Piezoelectric Beam Measurements

Table 3.5 summarizes the energy delivered to a 560k Ω resistor by the three different structures analyzed. $E_{beginning}$ is the energy delivered by the structure that appears in Figure 3.11, E_{heel} is the energy delivered by the structure that appears in Figure 3.12 and the term $E_{heel-hole}$ corresponds to the energy delivered by the structure of Figure 3.13. Table 3.6 repeats the information given by Table 3.5 but assuming no change in the slope of the energy delivered by the different activities.

Comparing the values of the energy delivered by the three different struc-

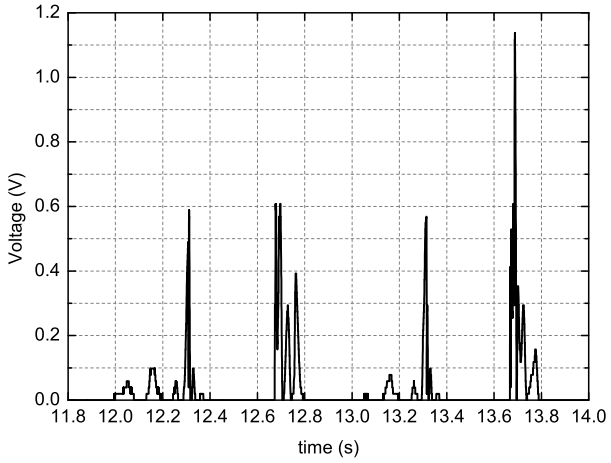

Figure 3.9: Voltage waveform of an heterogeneous symmetric bimorph placed at the end of a shoe with two piezoelectric films wired to a load of 560kΩ while a person is walking.

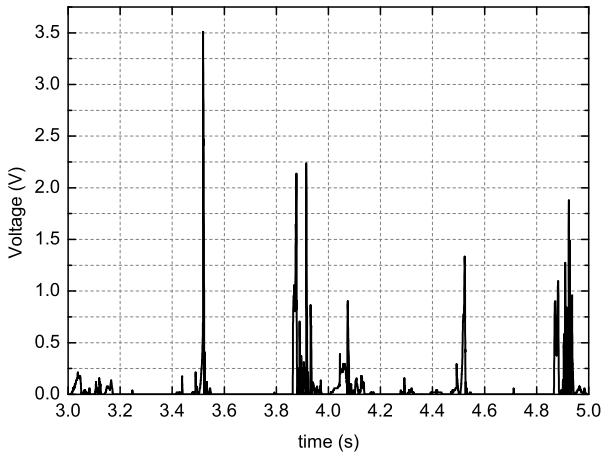

Figure 3.10: Voltage waveform of an heterogeneous symmetric bimorph simply supported bending beam with distributed load placed at the end of a shoe with two piezoelectric films wired to a load of 560kΩ while a person is walking.

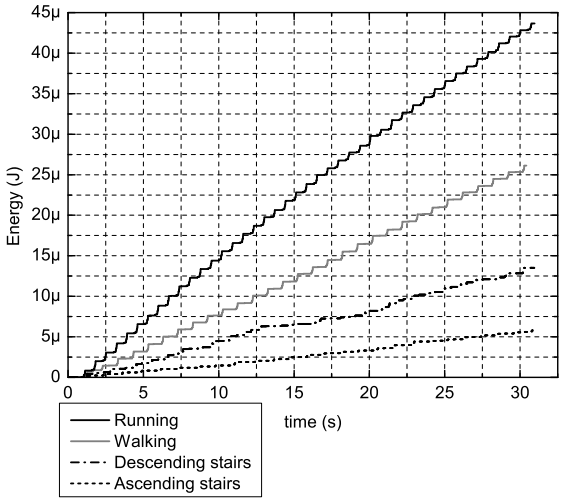

Figure 3.11: Energy delivered to a 560kΩ resistor by a symmetric heterogeneous bimorph placed in the position shown by Figure 3.2 for different activities.

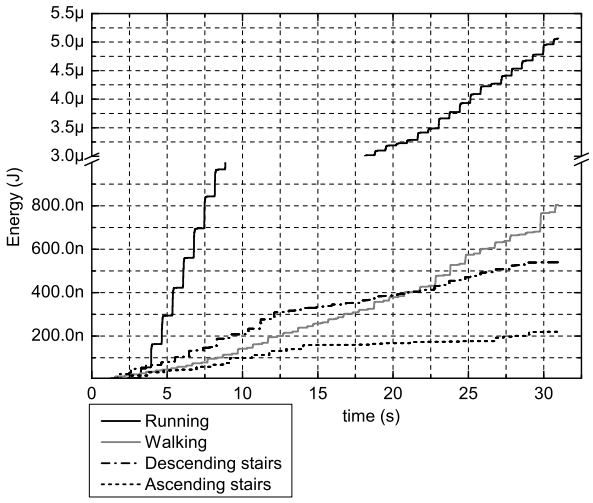

Figure 3.12: Energy delivered to a 560kΩ resistor by a symmetric heterogeneous bimorph placed in the position shown by Figure 3.3 for different activities.

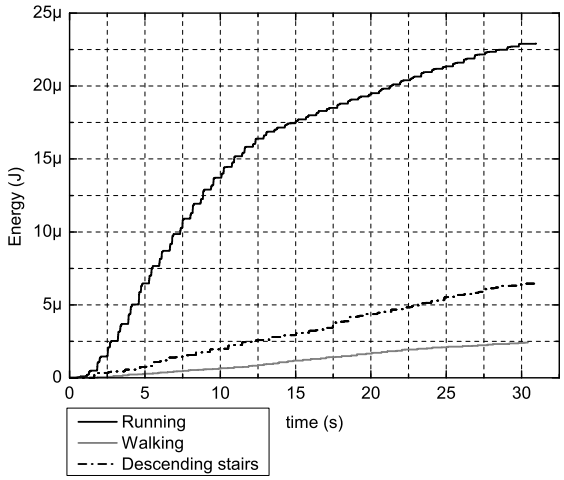

Figure 3.13: Energy delivered to a 560kΩ resistor by a symmetric heterogeneous bimorph placed in the position shown by Figure 3.4 for different activities.

Table 3.5: Energy delivered by the symmetric heterogenous bimporh structure placed in a shoe after t=30.42s of activity.

Activity	$E_{beginning}$ (μJ)	E_{heel} (μJ)	$E_{heel-hole}$ (μJ)
Running	42.83	4.96	22.9
Walking	26.13	0.771	2.41
Descending stairs	13.51	0.539	6.45
Ascending stairs	5.61	0.219	-

tures that appear in Table 3.6, it can be concluded that placing the bimorph structure at the beginning of the shoe harvests more energy than placing the same structure in the heel of the shoe. The heel of the foot receives mostly an impact in direction 3 but more energy is harvested, if the strain is made in direction 1 [19] as happens with the beginning of the shoe. This is the reason that explains that the results of placing the same bending beam structure at the beginning of the shoe and at the heel give better results for the first location.

A way to increase the energy harvested by piezoelectric transducers placed in the heel of the shoe is to deform also the piezoelectric in direction 1. Therefore, a considerable improvement is done employing the simply supported beam with distributed load as was suggested in [19] and the energy obtained with the simply supported beam structure in the heel of the shoe is in the same range than the energy obtained at the beginning of the shoe. An improvement of 866% for running, 217% for walking and 706% for descending stairs is obtained comparing

Table 3.6: Energy delivered by the symmetric heterogenous bimorph structure placed in a shoe after t=30.42s of activity assuming no change in the slopes.

Activity	$E_{beginning}$ (μJ)	E_{heel} (μJ)	$E_{heel-hole}$ (μJ)
Running	42.83	4.96	47.9
Walking	26.13	0.771	2.41
Descending stairs	13.51	0.8	6.45
Ascending stairs	5.61	0.4	-

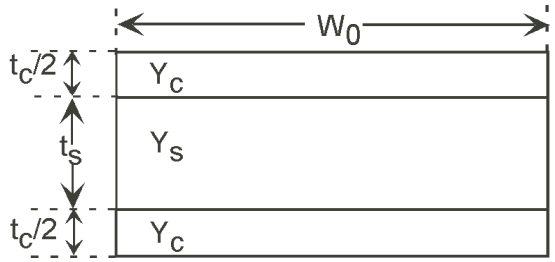

Figure 3.14: Cross section of symmetric heterogeneous bimorph beam. $t_c/2$ corresponds to piezoelectric film thickness whereas t_s corresponds to non-piezoelectric film thickness. Y_c is the Youngs modulus for the piezoelectric material, and Y_s is the Youngs modulus for the non-piezoelectric material. W_0 is the width of the rectangular beam.

the structure with the hole to the structure without the hole at the heel. The practical measurements done demonstrates that employing mechanical coupling with bending beams improves the harvested energy of piezoelectric films placed in the insoles of shoes.

3.5 Comparison of different Symmetric Heterogeneous Piezoelectric Beams in terms of Electrical and Mechanical Configurations

The electrical output obtained with the measurements done in the previous section, where PVDF films are excited by the walking activity of human body, is in the order of some micro amperes and units of volts. The current generated by the piezoelectric elements is proportional to the average strain done. However, this current can be not enough for the electric load to be powered by the piezoelectric transducer. In order to increase this low current, three different alternatives are presented in this section for using with symmetric heterogeneous bimorph beams.

Figure 3.14 shows the cross section of a symmetric heterogeneous bimorph beam composed by two piezoelectric elements placed at the top and bottom

of the structure with a thickness $t_c/2$ and a Young's modulus Y_c, and a non-piezoelectric element with thickness t_s and Young's modulus Y_s. In this structure, one piezoelectric film is placed at each side of the neutral axis position, and therefore one of the films is tensed whereas the other one is compressed with an average strain at each side S. First, it is introduced the calculation of the current and power for this structure in working mode 31 in order to can compare the three alternative structures with this one.

Piezoelectric constitutive equations relate the dielectric displacement, the electrical field and the mechanical strain, see Equation (3.5).

$$D_3 = \varepsilon_S^{33} E_3 + e_{31} S_1 \tag{3.5}$$

Integrating the above equation to obtain the mean value along the thickness, it is obtained:

$$\int_{t_s/2}^{(t_s+tc)/2} D_3 \mathrm{d}h = \int_{t_s/2}^{(t_s+tc)/2} \varepsilon_S^{33} E_3 \mathrm{d}h + \int_{t_s/2}^{(t_s+tc)/2} e_{31} S_1 \mathrm{d}h \tag{3.6}$$

Solving the previous equation and assuming that $E = \mathrm{d}V/\mathrm{d}h$ the result is:

$$D_3 \frac{t_c}{2} = \varepsilon_S^{33} V_3 + e_{31} S_x \frac{t_c}{2} \tag{3.7}$$

If it is assumed a sinusoidal steady state for the three state variables, Equation (3.7) is rewritten as:

$$D_3 e^{j\omega t} = 2\varepsilon_S^{33} \frac{V_3 e^{j\omega t}}{t_c} + e_{31} S_x e^{j\omega t} \tag{3.8}$$

Multiplying by the area of the triangular beam ($A = W_0 L/2$), doing the derivative of the previous equation and taking into account that $I = \mathrm{d}q/\mathrm{d}t$, it is obtained:

$$-I_3 = j\omega A \left[2\varepsilon_S^{33} \frac{V_3}{t_c} + e_{31} S_1 \right] \tag{3.9}$$

Assuming that the piezoelectric film is connected to a resistive load, R, the relation between the current generated and the voltage on the load is $V_R = I_3 R$. Therefore, the following expressions represent the current and voltage generated.

$$I_3 = \frac{-j\omega A e_{31} S_1}{j\omega \frac{2A\varepsilon_S^{33}}{t_c} R + 1} \tag{3.10}$$

$$V_R = \frac{-j\omega A e_{31} S_1 R}{j\omega \frac{2A\varepsilon_S^{33}}{t_c} R + 1} \tag{3.11}$$

Following the notation shown in Section 3.1, it is known that $C_p' = \frac{2A\varepsilon_{33}^S}{t_c}$ and therefore the current and voltage equations can be rewritten as:

$$I_3 = \frac{-j\omega A e_{31} S_1}{j\omega C'_p R + 1} \tag{3.12}$$

$$V_R = \frac{-j\omega A e_{31} S_1 R}{j\omega C'_p R + 1} \tag{3.13}$$

The expressions for the modulus of the current and voltage are:

$$|I_3| = \frac{A e_{31} \omega S_1}{\sqrt{1 + \omega^2 C'^2_p R^2}} \tag{3.14}$$

$$|V_R| = \frac{A e_{31} \omega S_1 R}{\sqrt{1 + \omega^2 C'^2_p R^2}} \tag{3.15}$$

The mean electrical power generated by one piezoelectric film is:

$$\langle P_3 \rangle = \frac{|V_R|^2}{2R} = |I_3|^2 2R = \frac{\left(A e_{31} \omega S_1\right)^2 R}{2\left(1 + \omega^2 C'^2_p R^2\right)} \tag{3.16}$$

The maximum mean electrical power occurs when $R = 1/\left(\omega C'_p\right)$.

The average strain for the top or bottom piezoelectric films of a symmetric heterogeneous bimorph beam is:

$$S_1 = y_{max} \frac{t_c \left(1 + 2t_s/t_c\right)}{2L^2} \tag{3.17}$$

Connecting electrically in parallel the top and the bottom films of the structure shown in Figure 3.14, the capacitance and current will be doubled. Therefore, the mean electrical power dissipated on the load is:

$$\langle P_{3parallel} \rangle = \frac{2\left(A e_{31} \omega S_1\right)^2 R}{\left(1 + \omega^2 4 C'^2_p R^2\right)} \tag{3.18}$$

In this case, the maximum mean electrical power occurs when $R = 1/\left(2\omega C'_p\right)$

1. Structure A. n piezoelectric symmetric heterogeneous bimorph beams with a piezoelectric film of thickness $t_c/2$ at each side and a non piezoelectric material of thickness t_s, see Figure 3.15. All the beams have the same average strain connected electrically in parallel and the top and bottom films also connected in parallel. Therefore, the current generated with this structure is:

$$I_{3A} = \frac{-j\omega 2n A e_{31} S_1}{1 + j\omega 2n C'_p R} \tag{3.19}$$

The mean electrical power generated by this structure is:

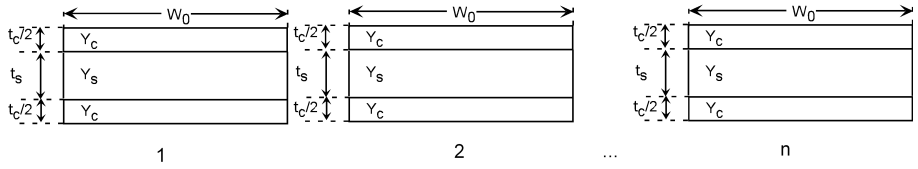

Figure 3.15: Cross section of n piezoelectric symmetric heterogeneous bimorph beams.

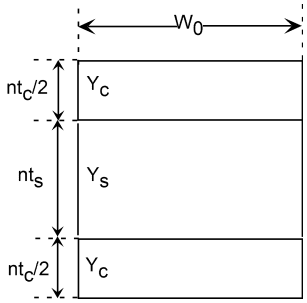

Figure 3.16: Cross section of a piezoelectric symmetric heterogeneous bimorph beam with a piezoelectric film of thickness $nt_c/2$ placed at each side of the non piezoelectric material with thickness nt_s.

$$\langle P_{3A} \rangle = \frac{\left(2nAe_{31}\omega S_x\right)^2 R}{2\left(1+\omega^2 4n^2 C_{p31}'^2 R^2\right)} \tag{3.20}$$

In this case the maximum mean electrical power is generated when $R = 1/\left(2n\omega C_p'\right)$.

2. Structure B. A piezoelectric symmetric heterogeneous bimorph with a piezoelectric film of thickness $nt_c/2$ at each side and a non piezoelectric material of thickness nt_s, see Figure 3.16.

   The average strain for the top or bottom film of thickness $nt_c/2$ is $S_{1B} = nS_1$. Thus, the current generated by the parallel electrical connection of two piezoelectric films of thickness $nt_c/2$ is:

$$I_{3B} = \frac{-j\omega 2nAe_{31}S_1}{1+j\omega 2/nC_{p31}'R} \tag{3.21}$$

   The mean electrical power is given by the following expression:

$$\langle P_{3B} \rangle = \frac{\left(2nAe_{31}\omega S_x\right)^2 R}{2\left(1+\omega^2 4/n^2 C_p'^2 R^2\right)} \tag{3.22}$$

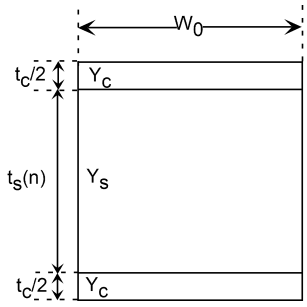

Figure 3.17: Cross section of a piezoelectric symmetric heterogeneous bimorph beam with a piezoelectric film of thickness $t_c/2$ placed at each side of the non piezoelectric material with thickness $t_s(n)$, see Equation (3.23)
.

In this case the maximum mean electrical power is generated when $R = n/\left(2\omega C_p'\right)$

3. Structure C. This structure is shown in Figure 3.17 where one piezoelectric film of thickness $t_c/2$ is placed at each side of the support film which has a thickness of $t_s\left(n\right)$, see Equation 3.23. The total thickness of this structure is the same as the thickness of the two structures described before. However, in this case only one piezoelectric film is placed at the top and bottom of the beam.

$$t_s\left(n\right) = nt_{s1} + \left(n-1\right)t_c \tag{3.23}$$

The average strain for one of the piezoelectric films placed at the top or bottom of the structure is:

$$S_{1C}\left(n\right) = y_{max}\frac{t_c\left(1+\frac{2t_s(n)}{t_c}\right)}{2L^2} = nS_1 + \frac{y_{max}}{2L^2}t_c\left(n-1\right) \tag{3.24}$$

The total current generated by the parallel connection of the two piezoelectric films of thickness $t_c/2$ is:

$$I_{3C} = \frac{-j\omega 2Ae_{31}S_1\left(n + t_c\left(n-1\right)/\left(t_c+2t_s\right)\right)}{1+j\omega 2C_p'R} \tag{3.25}$$

The mean electrical power generated with this structure is:

$$\langle P_{3C}\rangle = \frac{\left(2Ae_{31}\omega S_1\left(n + t_c\left(n-1\right)/\left(t_c+2t_s\right)\right)\right)^2 R}{2\left(1+\omega^2 4C_p'^2R^2\right)} \tag{3.26}$$

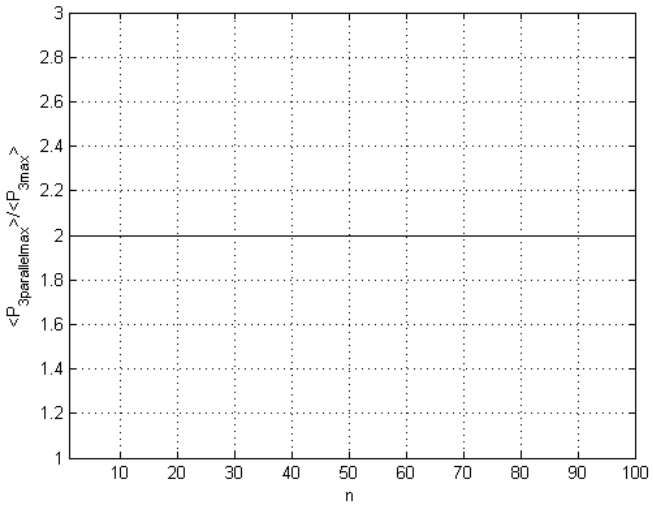

Figure 3.18: Ratio of the maximum mean electrical power of the parallel connection of the top and bottom piezoelectric elements of the structure shown in Figure 3.14 and the maximum electrical power of the top or bottom piezoelectric elements.

First, it is compared the power generated by the parallel electrical connection of the piezoelectric films located at the bottom and top of the structure of Figure 3.14 with the power generated by one of the piezoelectric films, see Figure 3.18. The results show that the power is doubled with the parallel connection. It must be taken into consideration that for each structure analyzed, the value of R has been substituted by its optimum value that makes maximum the mean electrical power. In order to compare the three different structures presented, the ratio of the maximum mean electrical power obtained with each structure and the maximum mean electrical power generated by the parallel electrical connection of the structure of Figure 3.14 has been plotted employing the values shown in Table 3.7. Figures 3.19 and 3.20 show the ratio as a function of n. Structure B is better than structure A since it generates more power since the strain made with this structure is n times bigger. Figure 3.21 shows the ratio of power for structure C as a function of $\tau = t_s/t_c$ and n. This structure is not better than structure B but it is the better structure in terms of generated power as a function of the number of piezoelectric films employed since the thickness of the non piezoelectric material helps to obtain also a high strain.

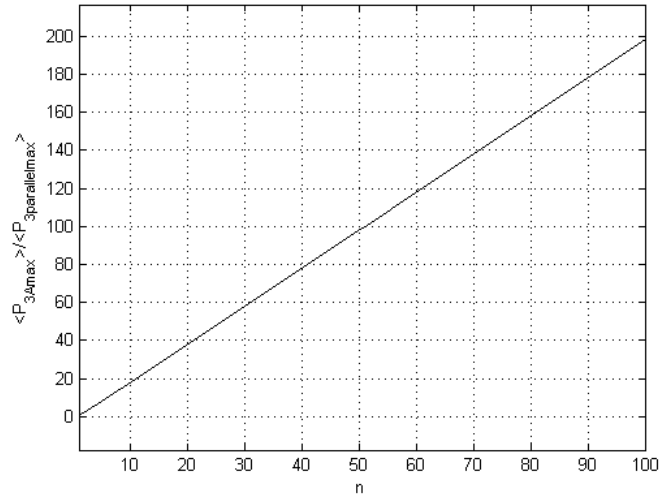

Figure 3.19: Ratio of the maximum mean electrical power of structure A and structure of Figure 3.14 versus n.

Table 3.7: Parameters employed for the simulation of structure A, B and C. The piezoelectric constants employed are for the PVDF films of Msiusa [104].

W_0	4 cm
L	5 cm
e_{31}	0.07 C/m^2
t_c	56 μm
t_s	$\tau * t_c$
ε_{33}^S	106e-12 F/m

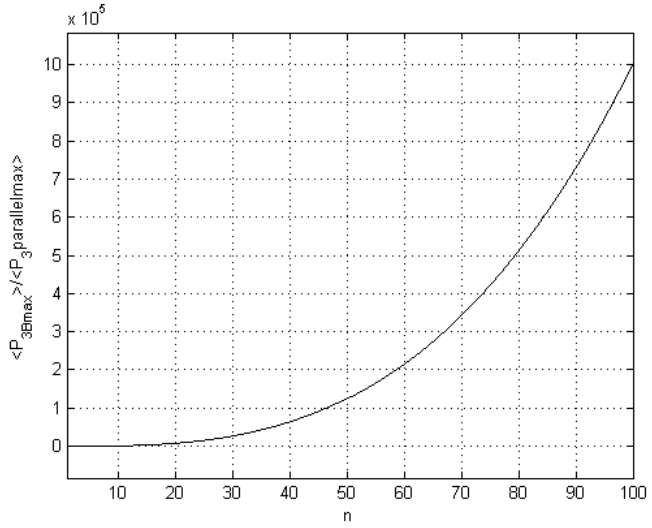

Figure 3.20: Ratio of the maximum mean electrical power of structure B and structure of Figure 3.14 versus n.

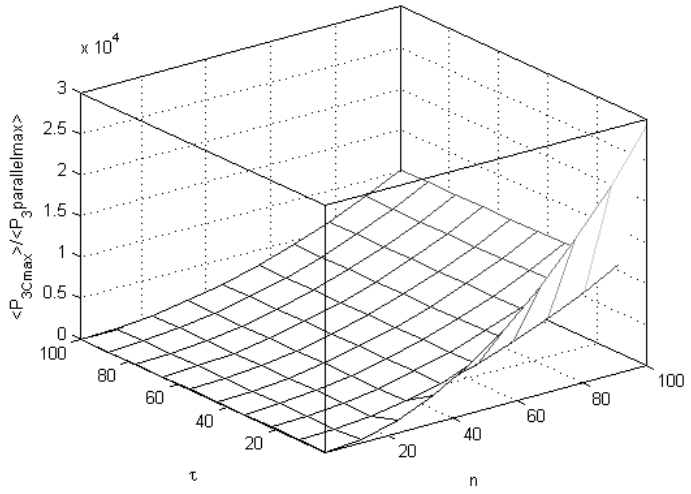

Figure 3.21: Ratio of the maximum mean electrical power of structure A and structure of Figure 3.14 versus τ and n.

3.6 Optimum Storage Capacitor for the Direct Discharge Circuit

Whereas the topic of increasing the harvested energy with piezoelectric materials placed in the insole of a shoe has been analyzed from the mechanical point of view in [19], the electrical point of view of the topic is covered by [20].

[20] in Chapter 10 employ an already described circuit [12,82,105], the direct discharge circuit, but with a new approach. The direct discharge circuit consists on the piezoelectric equivalent model for low frequencies wired to a full-wave diode rectifier connected to a storage capacitor, C_2. The piezoelectric equivalent model at low frequencies is shown in Figure 1 of [20]. It is composed basically by a current source, i_p, and a capacitor, C_1. [20] and Chapter 10 use a realistic current source, derived from measurements done during walking activity, for the calculation of the optimum value of C_2. However, all the equations are given as a function of the generated charge during walking activity and therefore, the calculus can be extrapolated to any mechanical activity where the generated charge is known.

The main contribution of [20] and Chapter 10 is the calculation of the optimum storage capacitor and the number of piezoelectric films connected in parallel that give the needed energy to power a low-power electronic device (like an RF transmitter) with a discontinuous load profile in the minimum time between operations. This section gives a more detailed qualitative explanation of the results obtained

Figure 16 of [20] shows the initial number of mechanical cycles needed to power on the electric load the first time, k_{ini}, the number of mechanical cycles needed to power on the electric load after the first time, k_s, and the value of the storage capacitance, C_2. It can be also shown in Figure 16 of [20] that there is a value for the graph k_s that gives the required energy with the minimum number of mechanical cycles. This optimal value is named $k_{s,opt}$ and the voltage at which the electric load must be turned on is called $V_{on,opt}$. The initial number of steps and the storage capacitance are selected for $V_{on,opt}$. Therefore, the values of V_{on} and C_2 are selected to assure that the electric load will be turned on in the minimum time between operations.

An application example where an RF communication module is powered intermittently to send a sensing data is given in section 5 of [20] to prove validity of the obtained results. The circuit operation is as follows. As the piezoelectric element is repetitively stressed, the voltage in the storage capacitor increases. Whenever this voltage reaches a certain limit (V_{on}),the capacitor is connected to the regulator input and it is discharged to a lower voltage, V_{off}, providing the energy required to sense and transmit the data, E_{req} (including the energy needed by the regulator). The capacitor is then disconnected from the load once more, allowing it to be recharged as can be shown in Figure 3.22. The value of V_{off} is determined by the voltage supply of the load and V_{on} is determined by the energy required by the load to operate. Therefore, as it is represented in Figure 3.22, the number of initial steps k_{ini} is bigger than k_s and an RF trans-

mission can be done every Tk_s seconds (after the first one), where T corresponds to the period of one mechanical cycle.

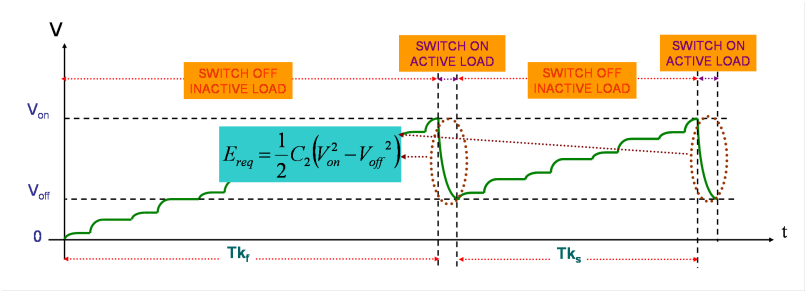

Figure 3.22: Working mode of the direct discharge circuit with control and regulator circuit to supply power to a load.

3.7 System-level simulation with piezoelectric energy harvesting

Chapter 13 [13] presents a complete simulation at system level using Verilog-A language. The energy harvesting transducer employed is PVDF piezoelectric film. The structure of the piezoelectric transducer employed during simulations corresponds to a symmetric heterogeneous bimorph with triangular shape, see Figure 3.23. A more detailed explanation of the equations and constants that are employed to model the piezoelectric transducer in Verilog-A is given in this section.

The mechanical conditions required to operate in mode 31 are: $T_2 = T_3 = 0$ and $S_2 = S_3 = 0$. Therefore, mechanical stress is only applied in direction 1, T_1 (length expansion working mode) and the electric displacement obtained is:

$$D_3 = d_{31} T_1 \tag{3.27}$$

In length expansion working mode, mechanical stress and strain are related by:

$$T_1 = Y_{11} S_1 \tag{3.28}$$

where Y_c corresponds to the Youngs modulus of the piezoelectric material that is defined as the mechanical stress obtained when a strain is applied. For Equation (3.28), the Young's modulus of the piezoelectric material corresponds to Y_{11} since the mechanical stress and the strain are in direction 1.

$$Q_3 = D_3 A \tag{3.29}$$

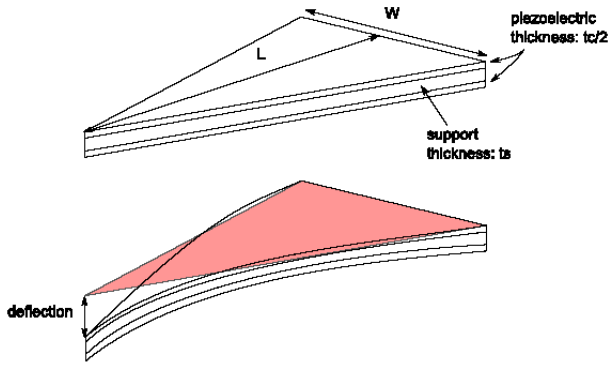

Figure 3.23: Structure of a symmetric heterogeneous bimorph with triangular shape.

where A is the area of the piezoelectric film. For the particular case shown in Figure 3.23, $A = W_0 L/2$.

Combining Equations (3.29) and (3.28), it is obtained:

$$Q_3 = d_{31} Y_{11} S_1 A \tag{3.30}$$

In [19], it was calculated the maximum deflection, y_{max}, and the average strain, S_1, for different bending beams structures including the structure shown in Figure 3.23. For the case of a triangular symmetric heterogeneous bimorph cantilever, S_1 is:

$$S_1 = \frac{y_{max} t_c}{2L^2} (1 + 2\tau) \tag{3.31}$$

where $\tau = t_s/t_c$, t_c is the piezoelectric material thickness, t_s is the non-piezoelectric material thickness and L is the length of the beam structure.

The maximum deflection is given by the following expression:

$$y_{max} = \frac{6FL^3}{Y_{11} W_0 t_c^3} \frac{1}{1 + 3\tau + 3\tau^2 + \eta\tau^3} \tag{3.32}$$

where $\eta = Y_s/Y_{11}$, Y_{11} is the piezoelectric material Young's modulus, Y_s is the non-piezoelectric material Young's modulus and W_0 is the base of the triangular cantilever.

For the piezoelectric generator model in Verilog-A, the mechanical input for the beam structure can be selected between the input force, F_1, and the maximum deflection of the beam, y_{max}. One variable depend on the other and are related by k_e, the elastic constant of the beam:

$$F_1 = k_e y_{max} \tag{3.33}$$

The charge generated by the top and bottom piezoelectric films, Q_3, is proportional to the maximum mechanical deflection and the charge constant, k_q of the beam.

$$Q_3 = k_q y_{max} \tag{3.34}$$

As it was shown in Section 3.6, the electrical model for low frequencies of a piezoelectric transducer is composed by a current source in parallel with a capacitor. The current source value is related with the mechanical part of the model by:

$$i = \frac{\mathrm{d}Q_3}{\mathrm{d}t} = k_q \dot{y}_{max} \tag{3.35}$$

The expression for k_q and k_e depends on the structure of the beam selected. From Equations (3.33) and (3.32), it is deduced that the value for k_e is:

$$k_e = \frac{Y_c W_0 t_c^3}{6L^3} \left(1 + 3\tau + 3\tau^2 + \eta\tau^3\right) \tag{3.36}$$

Substituting into Equation (3.30), the value of S_1 given by Equation (3.31) and comparing the result with Equation (3.34), it is obtained the value of k_q.

$$k_q = \frac{W_0 t_c}{2L} d_{31} Y_{11} \left(1 + 2\tau\right) \tag{3.37}$$

where $\tau = t_s/t_c$, $\eta = Y_s/Y_{11}$, Y_c is the piezoelectric material Young's modulus, Y_s is the non-piezoelectric material Young's modulus, W_0 is the base of the triangular cantilever.

The capacitance of one of the piezoelectric films with thickness $t_c/2$ is:

$$C_1 = \frac{2\varepsilon_{33}^T W_0 L}{t_c} \left(1 - k_{31}^2\right) \tag{3.38}$$

where ε_{33}^T is the dielectric displacement developed in a plane perpendicular to direction 3 when an electric field is applied in direction 3 with a constant mechanical stress and k_{31} is the electromechanical coupling coefficient for the length expansion working mode.

These equations are included in the piezoelectric transducer Verilog-A model. If the top and the bottom piezoelectric films are connected in parallel (as in the simulations developed in the present paper), the current generated is two times the current given in Equation (3.35) as well as the total capacitance is two times the capacitance shown in Equation (3.38).

Chapter 4

Inductive Energy Harvesting Generator

The principle governing inductive generators is the well known Faraday's law. Any change in the magnetic environment of a coil of wire will cause a voltage to be induced in the coil, of magnitude given by Faraday's law:

$$\epsilon_{induced} = -\frac{\mathrm{d}\phi_m}{\mathrm{d}t} \tag{4.1}$$

where ϕ_m is the flux of the magnetic field through the surface of the coil. The change could be produced by changing the magnetic field strength, moving a magnet toward or away from the coil, moving the coil into or out of the magnetic field, rotating the coil relative to the magnet, etc.

In the case of a fixed magnet causing the magnetic field, an inductive generator can be designed to harvest kinetic energy, since vibrations can modify the position of the coil with respect to the magnet. Most of the applications of electromagnetic transducers based on this principle are designed to harvest energy from vibrating machinery to power WSNs.

Previous works modeling electromagnetic induction microgenerators [31, 35, 106–108] describe the response of the system in the frequency domain. The frequency-domain analysis gives insight on important design parameters, especially regarding the mechanical resonance oscillation frequency of the converter in relation to the frequency spectrum of input accelerations. It is indeed possible to obtain from frequency-domain the analysis of some electrical magnitudes (e.g. peak power), but other magnitudes, like accumulated energy, can only be obtained from time-domain analysis. In addition, frequency-domain models rely on linear approximations of the mechanical and electrical system (small swing oscillations of the mass in the magnetic field, and a linear electrical load) and therefore, large swing oscillations are not adequately modeled. These facts motivate the time-domain analysis made in [21].

For the time domain analysis, it is necessary to do real acceleration measurements of different parts of human body in order to analyze the use of induc-

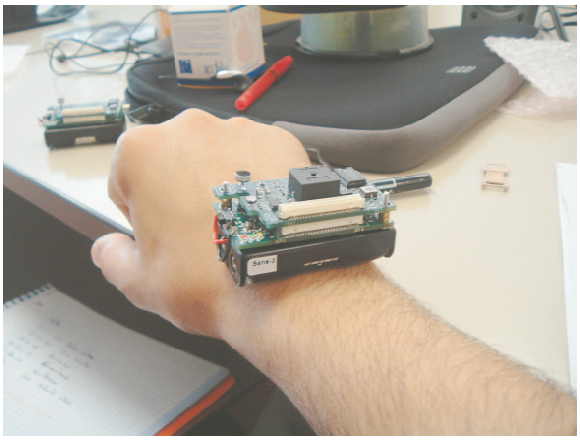

Figure 4.1: Mica 2 sensor board employed for the human body acceleration measurements.

tive energy harvesting generators that recover energy from human body vibrations. Next sections explain the method employed for the sensor calibration and present the measurements obtained. The acceleration measurements obtained placing the sensors at the knee of a person while the person was walking were presented and analyzed in [21]. However, this section gives the results of the complete set of measurements done placing the accelerometers at different parts of the human body doing different activities.

4.1 Accelerometer sensor calibration

The measurement setup employs Mica2 motes with its sensor board, see Figure 4.1. This sensor board has a 2-axis accelerometer, ADXL202JE [109], with a range of $\pm 2g$. The accelerometer has an analog and a digital output with a duty cycle proportional to the measured acceleration. The analog sensitivity is of 167 mV/g while the digital sensitivity is 11 % duty cycle change per g and a resolution of 2 mg. Only the digital output was employed for the acceleration measurements done. The duty cycle outputs are connected to the microprocessor counter of the Mica2 motes that has 10 bit resolution.

Before starting the measurements, it is necessary to calibrate the accelerometers [110–112]. Tables 4.1, 4.2 and 4.3 show the measurements obtained from the digital output to calibrate the 2-axis accelerometer included in the sensor board. It is necessary to calculate the offset, o, and the sensitivity, s, of the sensors for each one of its axis. Equations (4.2-4.5) allow to calculate these two parameters for x-axis and y-axis and thus, to calibrate the accelerometers. The calibration process is done by rotating the sensor into known accelerations. When the axis of the sensor is placed in the same direction and sense that the

gravity, $1g$, the value obtained is named X_{1g} and Y_{1g} for x-axis and y-axis, respectively. When the axis of the sensor is placed in the opposite direction of the gravity, $-1g$, the value measured is called X_{-1g} and Y_{-1g} for x-axis and y-axis, respectively.

By rotating the sensor into a +1 G and a 1 G position, the offset and sensitivity can be calculated to within

Table 4.1: Calibration measurements for sensor board 1.

Position	X-axis $[g]$	X-axis $[count]$	Y-axis $[g]$	Y-axis $[count]$
1	0	519	0	476
2	-1	461	0	476
3	1	574	0	475
4	0	519	1	532
5	0	521	-1	417

Table 4.2: Calibration measurements for sensor board 2, first measurement

Position	X-axis $[g]$	X-axis $[count]$	Y-axis $[g]$	Y-axis $[count]$
1	0	517	0	450
2	-1	461	0	450
3	1	580	0	449
4	0	515	1	510
5	0	515	-1	390

Table 4.3: Calibration measurements for sensor board 2, second measurement

Position	X-axis $[g]$	X-axis $[count]$	Y-axis $[g]$	Y-axis $[count]$
1	0	520	0	452
2	-1	462	0	452
3	1	584	0	454
4	0	521	1	512
5	0	520	-1	392

$$o_x = \frac{X_{1g} + X_{-1g}}{2} \tag{4.2}$$

$$s_x = \frac{X_{1g} - X_{-1g}}{2} \tag{4.3}$$

$$o_y = \frac{Y_{1g} + Y_{-1g}}{2} \tag{4.4}$$

$$s_y = \frac{Y_{1g} - Y_{-1g}}{2} \tag{4.5}$$

The results obtained for offset and sensitivity from the calibration measurements done are presented in Table 4.4 where the subindex indicates the sensor board employed. The results for sensor board 2 have been calculated with the mean value of the two measurements done.

Table 4.4: Calibration results for sensor board 1 and 2.

o_{x1}	s_{x1}	o_{y1}	s_{y1}	o_{x2}	s_{x2}	o_{y2}	s_{y2}
517.5	56.5	474.5	57.5	521.75	59.75	451	60

Employing the measured number of counts (X for an x-axis measurement and Y for an y-axis measurement), the measured acceleration expressed in g, Acc, is calculated as:

$$Acc_x = \frac{X - o_x}{s_x} \tag{4.6}$$

$$Acc_y = \frac{Y - o_y}{s_y} \tag{4.7}$$

4.2 Acceleration Measurements on the Human Body

Human activities like walking, ascending and descending stairs were done with the sensor nodes placed on the knee, ankle and wrist of a person. Some of the graphs of the acceleration measurements are shown in this section whereas the rest are in Appendix D.

Figure 4.2 shows the acceleration measurements of X-axis and Y-axis of an accelerometer placed on a knee while a person was walking. Figure 4.3 and Figure 4.4 show a zoom of the previous figure for X-axis and Y-axis, respectively, where it is possible to observe the periodicity of the signal. The period of the signal is approximately 1 s.

Figure 4.5 shows the acceleration measurements of X-axis and Y-axis of an accelerometer placed on a knee while a person was ascending and descending stairs. Figure 4.6 and Figure 4.7 show a zoom of the previous figure for X-axis and Y-axis, respectively.

S. Roundy [105] analyzed different vibration sources present in everyday objects like microwaves, refrigerator, etc. He concludes that the vibrations have a sinusoidal nature and therefore, it is possible to work with a transducer model in the frequency domain. However, it can be observed in the acceleration graphs shown in this section that the human body movements are not periodical movements with sinusoidal nature. It is also deduced from the graphs that the movements are somehow similar and that have associated low frequencies.

Two representative acceleration spectrum of a sensor placed on a knee while a person was walking and going up and down stairs are shown in Figures 4.8,

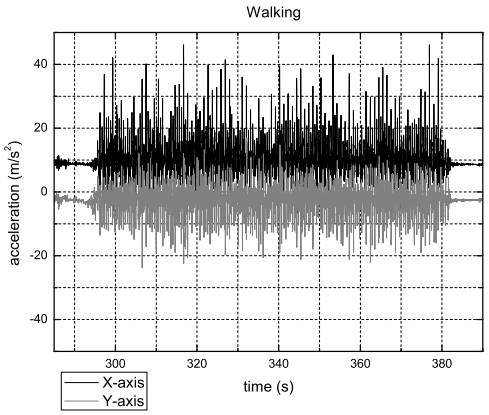

Figure 4.2: Acceleration measurements obtained by placing the sensor node on a knee while a person was walking with T_s=0.013s.

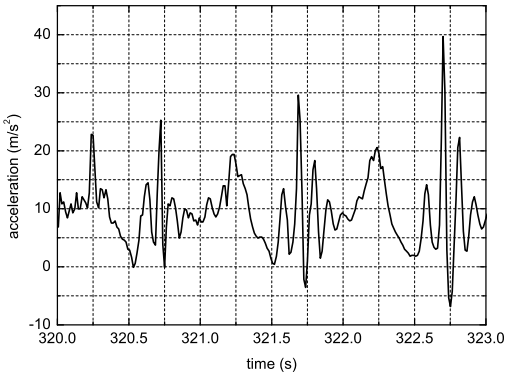

Figure 4.3: X-axis acceleration measurements obtained by placing the sensor node on a knee while a person was walking with T_s=0.013s.

4.9 and 4.10 respectively, in order to obtain more information about the acceleration behavior in the frequency domain. The acceleration spectrum graphs were obtained applying a Hamming window and the FFT algorithm to the acceleration measured data. The acceleration spectrum graphs show acceleration amplitudes in the same order of magnitude at different frequencies lower than 3 Hz. Therefore, mechanical movements of the human body have associated as

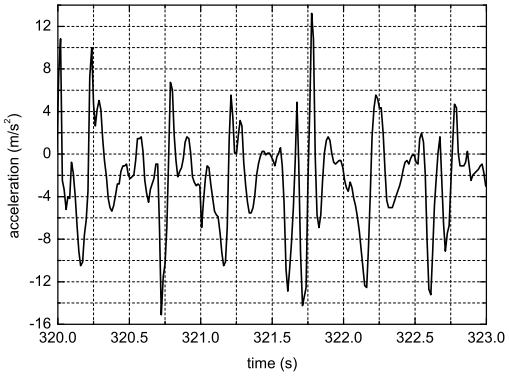

Figure 4.4: Y-axis acceleration measurements obtained by placing the sensor node on a knee while a person was walking with T_s=0.013s.

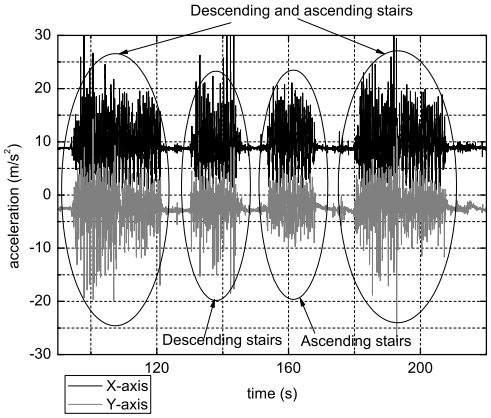

Figure 4.5: Acceleration measurements obtained by placing the sensor node on a knee while a person was descending and ascending stairs with T_s=0.013s.

expected low frequencies.

The magnitude and frequency spectrum of the human body accelerations are very different from one activity to another and they also change throughout the same activity even taking into account the same point of the human body. However, from the amplitudes obtained it can be deduced that the wrist is a worst location than the ankle or the knee for harvesting energy. The frequency

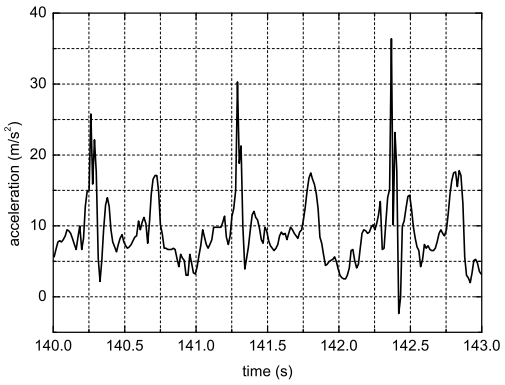

Figure 4.6: X-axis acceleration measurements obtained by placing the sensor node on a knee while a person was descending and ascending stairs with T_s=0.013s.

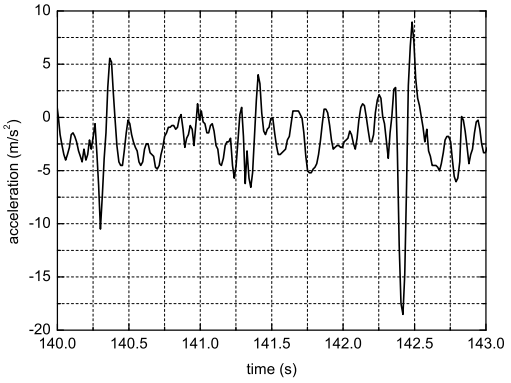

Figure 4.7: Y-axis acceleration measurements obtained by placing the sensor node on a knee while a person was descending and ascending stairs with T_s=0.013s.

domain can obtain the peak power harvested by the converter but other important magnitudes like the accumulated energy, can only be obtained from time-domain analysis. Thus, it has been demonstrated from the measurements that a model of the inductive energy harvesting generator for converting human

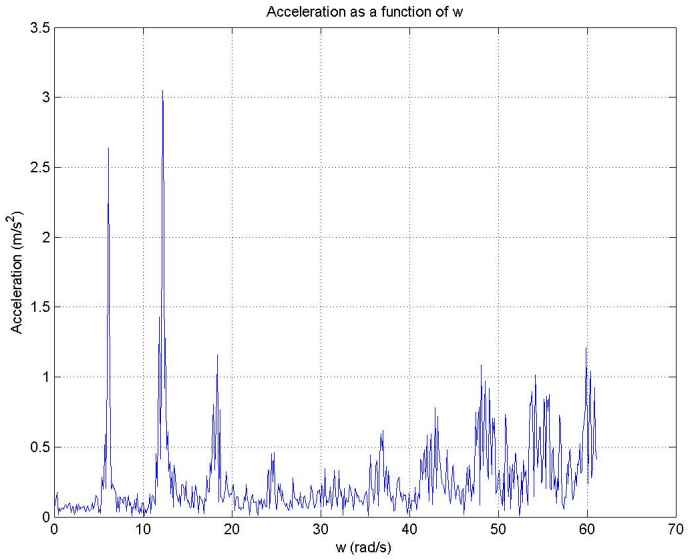

Figure 4.8: Acceleration spectrum calculated from measurements obtained by placing an accelerometer on the knee of a person that was walking with T_s=0.013s for X-direction.

movements must be done in the time domain. Next section shows the results obtained with time domain simulations employing the acceleration data measured as input parameter.

4.3 Simulation results in the time domain

As it is explained in [21] and Chapter 11, frequency-domain models assume implicitly a linear approximation of the mechanical and electrical system (small swing oscillations of the mass in the magnetic field, and a linear electrical load). Therefore, large swing oscillations are not adequately modeled. A linear and a non linear model were implemented in [21] and Chapter 11 employing the mixed simulator Ptolemy [15] in order to compare their results in the time domain and evaluate when the linear approximation for the model is valid. It was concluded that the linear model approximation is not valid for small swing oscillations of the mass in the magnetic fied. Thus, the simulation results shown in this section are done employing the non linear model.

Table 4.5 to Table 4.10 complete the simulations results obtained in [21] and Chapter 11 employing the non linear model and the acceleration measurements stored for different human activities.

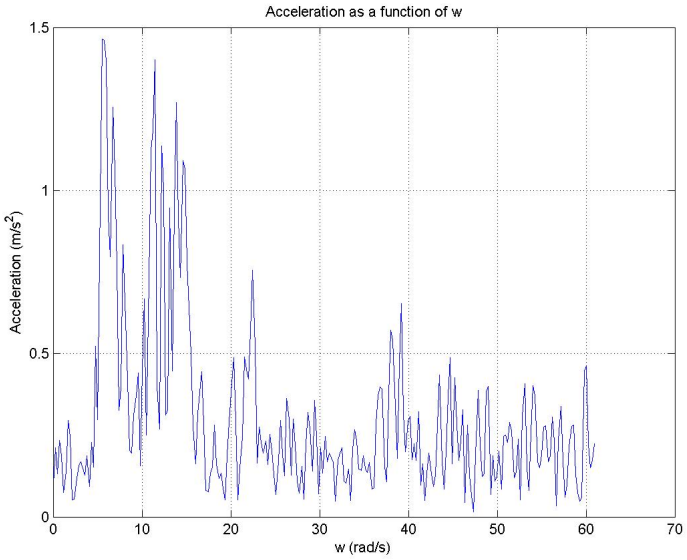

Figure 4.9: Acceleration spectrum calculated from measurements obtained by placing an accelerometer on a knee while a person was descending and ascending stairs with T_s=0.013s for X-direction.

4.4 Conclusions of the Simulation Results obtained with Acceleration Measurements of the Human Body

Table 4.11 shows a summary of the previous tables with the highest average power of each location at the human body while a human activity takes place. It is selected the average power for comparison between the different activities since the duration of each recorded activity was different.

The results shown in Table 4.11 were obtained for z_0=10 mm and the lowest value of the spring constant, k=400 N/m or k=600 N/m. In some simulations the magnet collides with the coil and for this reason, the spring constant is increased from 400 N/m to 600 N/m.

From the simulation results summarized in Table 4.11, it is deduced that the location of the knee, while a person is walking, is the one that generates more energy per second, $20.34\mu J$, with the simulation parameters $k = 600N/m$, $z_0 = 10mm$ and $b = 0.1$. The acceleration measurements, the simulated position of the proof mass of the inductive generator and the energy dissipated on the load for this case are shown in Figure 4.11, Figure 4.12 and Figure 4.13, respectively. With the same simulation parameters ($k = 600N/m$, $z_0 = 10mm$ and $b = 0.1$)

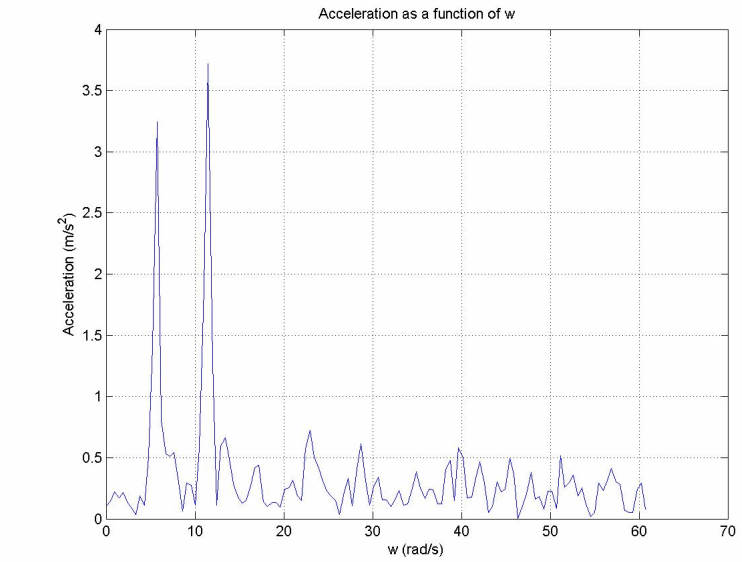

Figure 4.10: Acceleration spectrum calculated from measurements obtained by placing an accelerometer on a knee while a person was descending and ascending stairs with T_s=0.013s for X-direction.

the energy per second dissipated on the load, if the microgenerator is located in the ankle while a person is walking, is $11.68\mu J$. Placing the inductive generator in the knee while a person is ascending and descending stairs is the activity that generates less energy per second.

Therefore, it is concluded that the lower parts of the human body, knee and ankle, are the best ones to place inductive microgenerators and harvest energy from human activities like walking.

Table 4.5: Non linear model simulation results from acceleration x-axis measurements of the knee of a person while is going up and down stairs with $b = 0.1$.

z_0 =50 mm ($\beta_0 = 2.5$)						
k (N/m)	V_{peak} (mV)	E_{28sec} (J)	$\Delta\beta$	f_0 (Hz)	ζ_e	ζ_m
30	6.1	822.7E-9	3.11	3.9	1.57E-7	4.1E-2
50	8.84	810.1E-9	2.37	5.03	1.21E-7	3.2E-2
400	3.24	450.4E-9	462E-3	14.2	4.29E-8	1.1E-2
2000	2.17	95.3E-9	135.5E-3	31.8	1.92E-8	5E-3
z_0 =10 mm ($\beta_0 = 0.5$)						
k (N/m)	V_{peak} (mV)	E_{28sec} (J)	$\Delta\beta$	f_0 (Hz)	ζ_e	ζ_m
400	60.8	144E-6	462E-3	14.2	3.2E-4	1.1E-2
2000	40.4	32E-6	134.7E-3	31.8	1.43E-4	5E-3
8000	15.2	9.1E-6	28.7E-3	63.7	7.16E-5	2.5E-3
80000	4.82	588.5E-9	2.57E-3	201.3	2.26E-5	7.9E-4
z_0 =2 mm ($\beta_0 = 0.1$)						
k (N/m)	V_{peak} (mV)	E_{28sec} (J)	$\Delta\beta$	f_0 (Hz)	ζ_e	ζ_m
2000	47.3	29.84E-6	112.9E-3	31.8	6.4E-3	5E-3
8000	19	9.31E-6	27.6E-3	63.7	3.2E-3	2.5E-3
80000	6.3	566.2E-9	2.45E-3	201.3	1E-3	7.9E-4

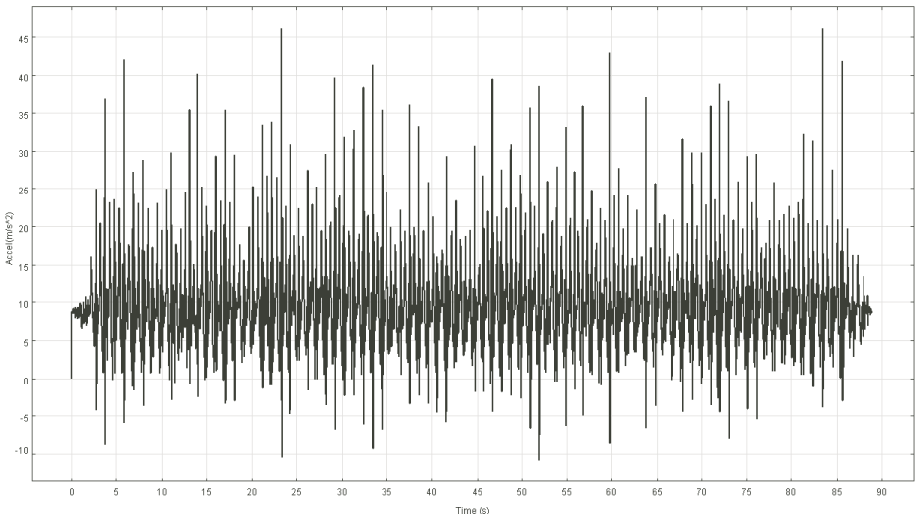

Figure 4.11: X-axis acceleration measurements obtained by placing the sensor node on the knee of a person when is walking.

Table 4.6: Non linear model simulation results from acceleration y-axis measurements of the knee of a person while is going up and down stairs with $b = 0.1$.

z_0 =50 mm ($\beta_0 = 2.5$)						
k (N/m)	V_{peak} (mV)	E_{28sec} (J)	$\Delta\beta$	f_0 (Hz)	ζ_e	ζ_m
50	127	79.3E-6	4.48	5.03	1.21E-7	3.2E-2
400	3.66	415E-9	0.495	14.2	4.29E-8	1.1E-2
2000	0.735	14.9E-9	65E-3	31.8	1.92E-8	5E-3
z_0 =10 mm ($\beta_0 = 0.5$)						
k (N/m)	V_{peak} (mV)	E_{28sec} (J)	$\Delta\beta$	f_0 (Hz)	ζ_e	ζ_m
400	72.6	145E-6	0.488	14.2	3.2E-4	1.1E-2
2000	13.68	5.13E-6	65E-3	31.8	1.43E-4	5E-3
8000	14.75	6.44E-6	25.5E-3	63.7	7.16E-5	2.5E-3
80000	2.54	143.9E-9	1.89E-3	201.3	2.26E-5	7.9E-4
z_0 =2 mm ($\beta_0 = 0.1$)						
k (N/m)	V_{peak} (mV)	E_{28sec} (J)	$\Delta\beta$	f_0 (Hz)	ζ_e	ζ_m
2000	15.3	4.33E-6	59.8E-3	31.8	6.4E-3	5E-3
8000	17.2	5.17E-6	22.36E-3	63.7	3.2E-3	2.5E-3
80000	2.66	114.1E-9	1.62E-3	201.3	1E-3	7.9E-4

Table 4.7: Non linear model simulation results from acceleration x-axis measurements of the knee of a person while is walking with $b = 0.1$.

z_0 =50 mm ($\beta_0 = 2.5$)						
k (N/m)	V_{peak} (mV)	E_{89sec} (J)	$\Delta\beta$	f_0 (Hz)	ζ_e	ζ_m
30	20.2	7.01E-6	4.54	3.9	1.57E-7	4.1E-2
50	14.1	5.47E-6	3.27	5.03	1.21E-7	3.2E-2
400	11.9	6.39E-6	1.34	14.2	4.29E-8	1.1E-2
2000	2.11	238E-9	0.165	31.8	1.92E-8	5E-3
8000	2.12	329.8E-9	66.5E-3	63.7	9.6E-9	2.5E-3
z_0 =10 mm ($\beta_0 = 0.5$)						
k (N/m)	V_{peak} (mV)	E_{89sec} (J)	$\Delta\beta$	f_0 (Hz)	ζ_e	ζ_m
600	144	1.81E-3	730.5E-3	17.43	2.61E-4	9.1E-3
2000	36.65	80E-6	163.5E-3	31.8	1.43E-4	5E-3
8000	39.6	112.1E-6	65.5E-3	63.7	7.16E-5	2.5E-3
80000	6.88	1.61E-6	3.5E-3	201.3	2.26E-5	7.9E-4
z_0 =2 mm ($\beta_0 = 0.1$)						
k (N/m)	V_{peak} (mV)	E_{89sec} (J)	$\Delta\beta$	f_0 (Hz)	ζ_e	ζ_m
2000	59.77	76.21E-6	154.55E-3	31.8	6.4E-3	5E-3
8000	48.45	91.84E-6	60E-3	63.7	3.2E-3	2.5E-3
80000	8.93	1.51E-6	3.8E-3	201.3	1E-3	7.9E-4

Table 4.8: Non linear model simulation results from acceleration y-axis measurements of the knee of a person while is walking with $b = 0.1$.

z_0 =50 mm ($\beta_0 = 2.5$)						
k (N/m)	V_{peak} (mV)	E_{89sec} (J)	$\Delta\beta$	f_0 (Hz)	ζ_e	ζ_m
60	55.44	62.67E-6	3.69	5.51	1.1E-7	2.9E-2
400	5.36	1.91E-6	688E-3	14.2	4.29E-8	1.1E-2
2000	1.6	125.3E-9	115.5E-3	31.8	1.92E-8	5E-3
8000	1.11	85.33E-9	34.5E-3	63.7	9.6E-9	2.5E-3
z_0 =10 mm ($\beta_0 = 0.5$)						
k (N/m)	V_{peak} (mV)	E_{89sec} (J)	$\Delta\beta$	f_0 (Hz)	ζ_e	ζ_m
400	107.7	671.03E-6	679.5E-3	14.2	3.2E-4	11.2E-3
2000	29.97	42.9E-6	115.5E-3	31.8	1.43E-4	5E-3
8000	20.8	29.2E-6	34E-3	63.7	7.16E-5	2.5E-3
80000	4.46	893.6E-9	3E-3	201.3	2.26E-5	7.9E-4
z_0 =2 mm ($\beta_0 = 0.1$)						
k (N/m)	V_{peak} (mV)	E_{89sec} (J)	$\Delta\beta$	f_0 (Hz)	ζ_e	ζ_m
2000	34.31	30.8E-6	102.88E-3	31.8	6.4E-3	5E-3
8000	24.8	23.68E-6	31E-3	63.7	3.2E-3	2.5E-3
80000	5.46	756.1E-9	2.5E-3	201.3	1E-3	7.9E-4

Table 4.9: Non linear model simulation results from acceleration x-axis measurements of the ankle of a person while is walking with $b = 0.1$.

z_0 =50 mm ($\beta_0 = 2.5$)						
k (N/m)	V_{peak} (mV)	E_{131sec} (J)	$\Delta\beta$	f_0 (Hz)	ζ_e	ζ_m
30	16.88	4.18E-6	4.81	3.9	1.57E-7	4.1E-2
50	15.73	10.57E-6	3.45	5.03	1.21E-7	3.2E-2
400	4.47	2.22E-6	575E-3	14.2	4.29E-8	1.1E-2
2000	3.25	936.2E-9	203.5E-3	31.8	1.92E-8	5E-3
8000	0.52	29.78E-9	5.055E-3	63.7	9.6E-9	2.5E-3
z_0 =10 mm ($\beta_0 = 0.5$)						
k (N/m)	V_{peak} (mV)	E_{131sec} (J)	$\Delta\beta$	f_0 (Hz)	ζ_e	ζ_m
400	86.8	704.37E-6	573.9E-3	14.2	3.2E-4	11.2E-3
2000	60.6	315.25E-6	202.45E-3	31.8	1.43E-4	5E-3
8000	21.05	42.54E-6	44.1E-3	63.7	7.16E-5	2.5E-3
80000	9.76	10.13E-6	5E-3	201.3	2.26E-5	7.9E-4
z_0 =2 mm ($\beta_0 = 0.1$)						
k (N/m)	V_{peak} (mV)	E_{131sec} (J)	$\Delta\beta$	f_0 (Hz)	ζ_e	ζ_m
2000	69.9	313.2E-6	169E-3	31.8	6.4E-3	5E-3
8000	26.9	36.1E-6	40.2E-3	63.7	3.2E-3	2.5E-3
80000	11.77	7.62E-6	4.76E-3	201.3	1E-3	7.9E-4

Table 4.10: Non linear model simulation results from acceleration y-axis measurements of the ankle of a person while is walking with $b = 0.1$.

z_0 =50 mm ($\beta_0 = 2.5$)						
k (N/m)	V_{peak} (mV)	E_{131sec} (J)	$\Delta\beta$	f_0 (Hz)	ζ_e	ζ_m
30	113.5	66.18E-6	4.49	3.9	1.57E-7	4.1E-2
50	39.66	19.02E-6	3.51	5.03	1.21E-7	3.2E-2
400	9.77	5.47E-6	1.07	14.2	4.29E-8	1.1E-2
2000	4.31	1.64E-6	250E-3	31.8	1.92E-8	5E-3
8000	1.87	263.2E-9	56.5E-3	63.7	9.6E-9	2.5E-3
z_0 =10 mm ($\beta_0 = 0.5$)						
k (N/m)	V_{peak} (mV)	E_{131sec} (J)	$\Delta\beta$	f_0 (Hz)	ζ_e	ζ_m
600	148.4	1.53E-3	679.5E-3	17.43	1.3E-4	9.1E-3
2000	82.37	561.8E-6	249.5E-3	31.8	1.43E-4	5E-3
8000	35.1	89.9E-6	56.5E-3	63.7	7.16E-5	2.5E-3
z_0 =2 mm ($\beta_0 = 0.1$)						
k (N/m)	V_{peak} (mV)	E_{131sec} (J)	$\Delta\beta$	f_0 (Hz)	ζ_e	ζ_m
2500	76.9	218.9E-6	159.81E-3	35.59	5.7E-3	4.5E-3
8000	42.85	70.48E-6	51.5E-3	63.7	3.2E-3	2.5E-3
80000	16.5	10.48E-6	6.55E-3	201.3	1E-3	7.9E-4

Table 4.11: Summary table with the highest average power for measurements done in different parts of the human body while various activities where realized.

	P (μW)	k (N/m)	V_{peak} (mV)	$\Delta\beta$	f_0 (Hz)
$Knee - Stairs_x$	5.14	400	60.8	462E-3	14.2
$Knee - Stairs_y$	5.18	400	72.6	488E-3	14.2
$Knee - Walking_x$	20.34	600	144	730.5E-3	17.43
$Knee - Walking_y$	7.54	400	107.7	679.5E-3	14.2
$Ankle - Walking_x$	5.38	400	86.8	573.9E-3	14.2
$Ankle - Walking_y$	11.68	600	148.4	679.5E-3	17.43

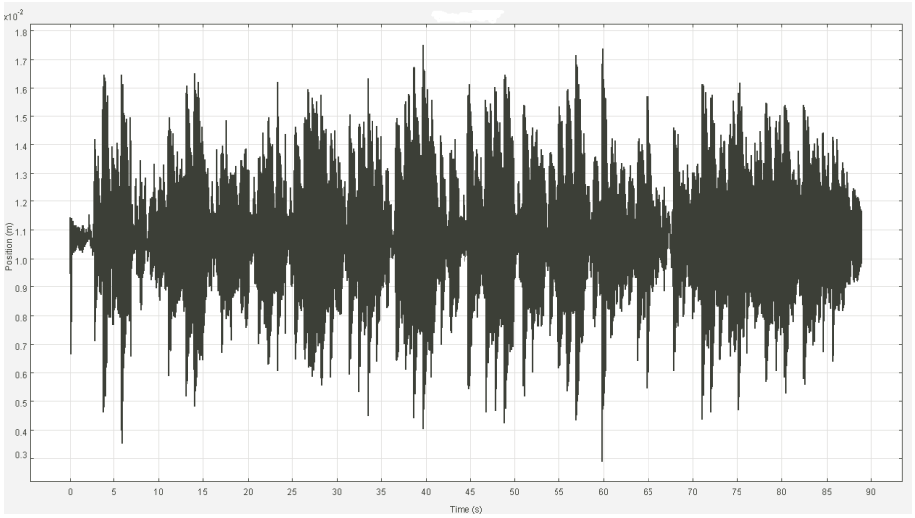

Figure 4.12: Position of the proof mass when the external acceleration of Figure 4.11 is applied to the microgenerator. The parameters employed during the simulation are $k = 600N/m$, $z_0 = 10mm$ and $b = 0.1$.

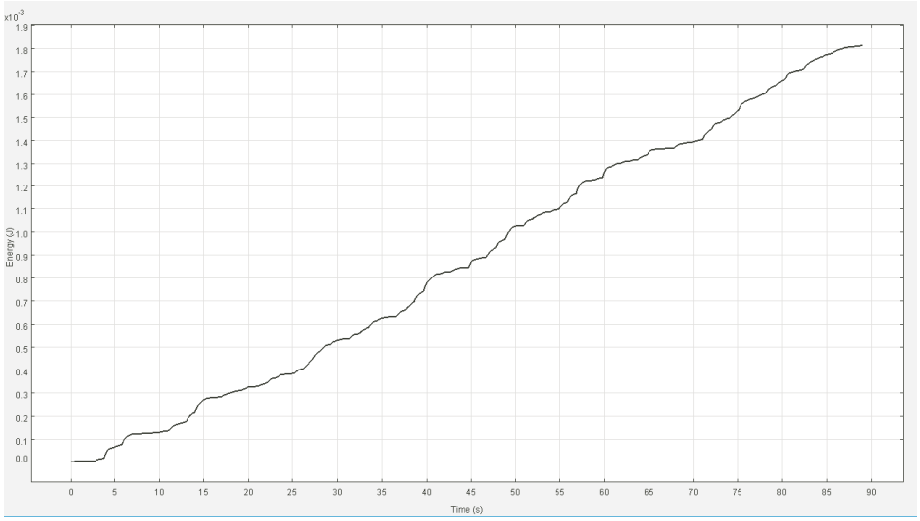

Figure 4.13: Energy dissipated in the load when the external acceleration of Figure 4.11 is applied to the microgenerator. The parameters employed during the simulation are $k = 600N/m$, $z_0 = 10mm$ and $b = 0.1$.

Chapter 5

Thermoelectric Generator

The thermoelectric generator (TEG) also called thermogenerator basically consists of one or more thermocouples, each one being composed of a p-type and n-type semiconductor connected electrically in series and thermally in parallel. The TEG is based on the Seebeck effect and produces an electrical voltage proportional to the temperature difference between hot and cold junctions and to the number of thermocouples since the electrical connection allows to add the voltage obtained at each thermocouple. The heat flux that enters or leaves a junction of a thermoelectric device is generated by two mechanisms: the presence of a temperature gradient at the junction and the absorption or liberation of energy due to the Peltier effect [49].

This section shows the electrical model of the thermogenerator, characterizes some commercial thermogenerators in order to select one of them and finally presents a power management unit designed to supply power to an application where a sensor unit and an RF transmitter send the sensing data with the energy generated by a TEG that converts the heat flow existing between the human hand and the ambient, see Figure 5.1.

5.1 Electrical model of a Thermocouple

A Peltier device can be employed as a thermocooler (TEC) or as a thermogenerator (TEG). In the first case, an electrical energy is applied to the TEC that is able to create a temperature gradient between its two sides. In the second case, a voltage is generated with the temperature gradient present between the two sides of the TEG. An electrical model of a TEG allows to simulate the complete energy harvesting generator based on a thermoelectric transducer to predict its behavior. Therefore, electrical and thermal circuits can be simulated together and it can be predicted the minimum temperature difference necessary to start up the power management unit or the response of the circuit to variations in the thermal source. It is first introduced the TEC electrical model since it appears in the literature and afterwards it is presented the electrical model for the TEG,

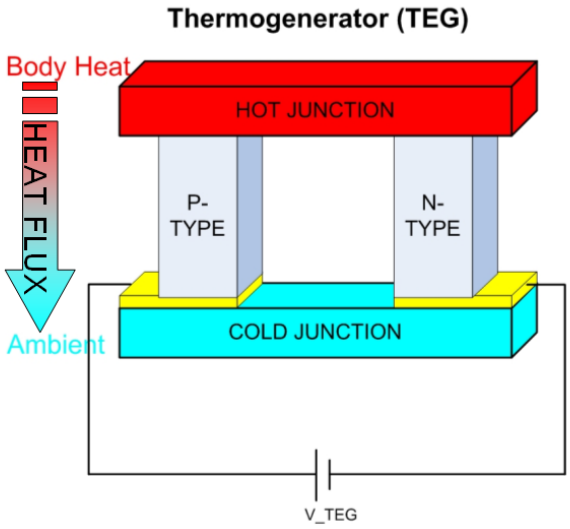

Figure 5.1: The thermogenerator converts the heat flow existing between the human hand and the ambient in electrical energy.

based in the previous one.

5.1.1 Thermocooler Electrical Model

Chavez et al. in [1] and Lineykin et al. in [2] presented two equivalent SPICE models for TECs. In the TEC, the heat is emitted by the cold side and it is absorbed by the hot side when electrical energy is applied to the Peltier device. Figure 5.2 shows the TEC equivalent circuit based on the model presented by Chavez et al. whereas Figure 5.3 shows the TEC circuit based on the model presented by Lineykin et al. Two different circuits can be distinguished in both models. On one hand, the circuit that models the thermal behavior and on the other hand, the circuit that models the electrical behavior. The circuit that models the TEC electrical response has a temperature dependent voltage source, V_α, and a resistor, R_m. The value of the voltage source is proportional to the temperature gradient between the hot side, T_H, and the cold side, T_C of the TEC and to the Seebeck's coefficient, α_m. R_m represents the equivalent electric resistance of the thermoelectric module. For the case of a TEC, an external current source (I in Figures 5.2 and 5.3) or voltage source must be connected to the electrical circuit in order to create a temperature gradient between both sides of the thermoelectric module, TEM.

Some definitions of thermal parameters are necessary in order to understand the thermal part of the model. Specific heat capacity, also known simply as specific heat, c, is the measure of the heat energy required to raise the temper-

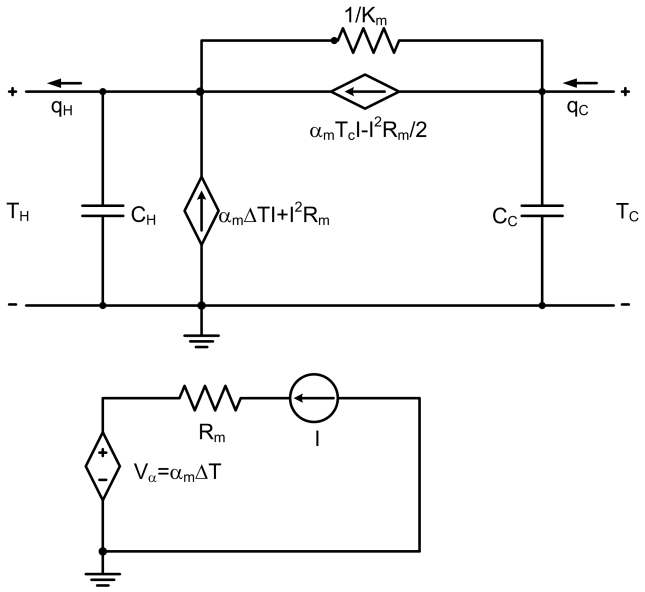

Figure 5.2: Thermocooler equivalent circuit [1].

ature of one gram of a substance by one Kelvin. Volumetric heat capacity, c_v, is the measure of the heat energy required to raise the temperature of one cubic meter of a substance by one Kelvin. It is different from specific heat capacity in that the volumetric heat capacity depends on the volume of the material, while the specific heat depends on the mass of the material. Thermal mass (also called heat capacity), C, is a measurable physical quantity that characterizes the ability of a body to store heat as it changes in temperature:

$$C = mc = Vc_v \, [J/K] \tag{5.1}$$

Thermal conductivity, k, is the property of a material that indicates its ability to conduct heat. It is defined as the quantity of heat, ΔQ, transmitted during time Δt through a thickness L, in a direction normal to a surface of area A, due to a temperature difference ΔT, under steady state conditions and when the heat transfer is dependent only on the temperature gradient.

$$k = \frac{Q}{t}\frac{L}{A\Delta T} \, [W/\,(mK)] \tag{5.2}$$

Thermal conductance, K, is the ability of a material to transfer heat per unit time:

$$K = \frac{kA}{L} \, [W/K] \tag{5.3}$$

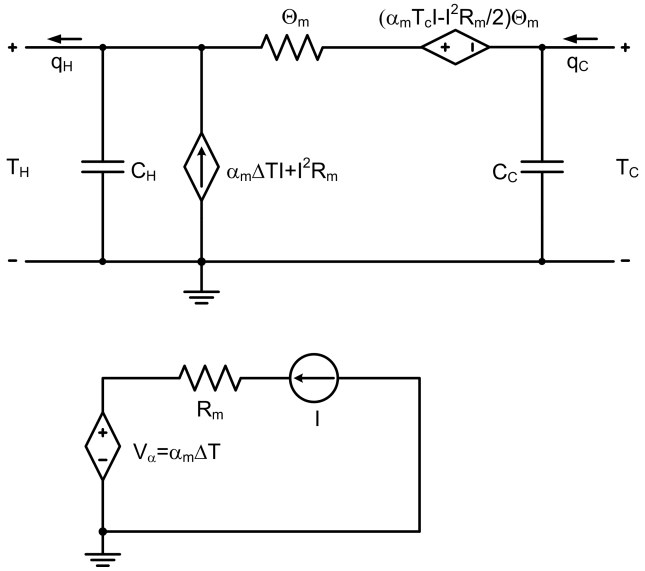

Figure 5.3: Thermocooler equivalent circuit [2].

Thermal resistance, Θ, is the difference of temperature between opposite faces due to 1W of heat flowing in a unit time through a plate of area A and thickness L.

$$\Theta = \frac{L}{kA} = \frac{1}{K}\,[K/W] \tag{5.4}$$

The thermal part of the model, illustrated by Figures 5.2 and 5.3, is composed by two capacitors at each side of the TEM, C_H and C_C. C_H is the thermal mass of the hot side of the Peltier element whereas C_C is the thermal mass of the hot side of the Peltier element. A resistor that represents the thermal conductance of the material, K_m, and two voltage controlled current sources also appear in the model whereas model based on [1] whereas the model based on [2] employs a voltage-controlled voltage source and the thermal resistance, Θ_m, instead of the thermal conductance. Both models are equivalent since $k_m = 1/\Theta_m$.

q_C is the heat absorbed by the cold side and q_H is the heat emitted at the hot side. The thermal part of the TEC model is illustrated by Figure 5.2 and described by Equations (5.5) and (5.6).

$$q_C = \alpha_m T_C I - \frac{I^2 R_m}{2} - K_m \Delta T \tag{5.5}$$

where $\alpha T_C I$ corresponds to the Seebeck's power generation, $\frac{1}{2} I^2 R_m$ corresponds to the Joule heating effect, the term $K_m \Delta T$ (and $\frac{\Delta T}{\Theta_m}$) is due to thermal con-

Table 5.1: Thermal parameters.

Parameter	Definition	Unit
C_H	Thermal mass of the hot side of the Peltier module	$[J/K]$
C_C	Thermal mass of the cold side of the Peltier module	$[J/K]$
K_m	Thermal conductance	$[W/K]$
Θ_m	Thermal resistance	$[K/W]$
R_m	Electrical resistance	$[\Omega]$
α_m	Seebeck's coefficient	$[V/K]$

vection and $\Delta T = T_H - T_C$. Thompson phenomenon ($1/2\tau_m I \Delta T$) is small and therefore is neglected in the models.

$$q_H = \alpha_m T_H I + \frac{I^2 R_m}{2} - K_m \Delta T \tag{5.6}$$

The electrical characteristic of the thermoelectric module can be modeled by a voltage source proportional to the temperature gradient between the hot and the cold side.

$$V_\alpha = \alpha \left(T_H - T_C\right) = \alpha \Delta T \tag{5.7}$$

When the TEM is employed as a TEC both sides of the TEM will be at ambient temperature at the beginning. Therefore, in order to simulate the model, it is necessary to give the ambient temperature as voltage initial conditions of capacitors C_H and C_C. The current or voltage delivered at the electrical part of the circuit will generate a temperature difference between the two sides of the TEM.

5.1.2 Thermogenerator Electrical Model

Figure 5.4 shows the equivalent circuit for a TEG based on the model explained in the previous section for a TEC. In the case of a TEG the electrical circuit is connected to the electrical load to power (modeled in the figure by resistor R_{load}) instead of an electrical energy source. Moreover, the sense in the heat fluxes and the current dependent sources is also different with respect to the previous model. In addition, taking into account that in the TEG, the heat is absorbed by the hot side and it is emitted by the cold side, the equations for the thermal part of the circuit are:

$$q_C = \alpha_m T_C I + \frac{I^2 R_m}{2} + k_m \Delta T \tag{5.8}$$

$$q_H = \alpha_m T_H I - \frac{I^2 R_m}{2} + k_m \Delta T \tag{5.9}$$

The equation for the electrical part of the TEG is:

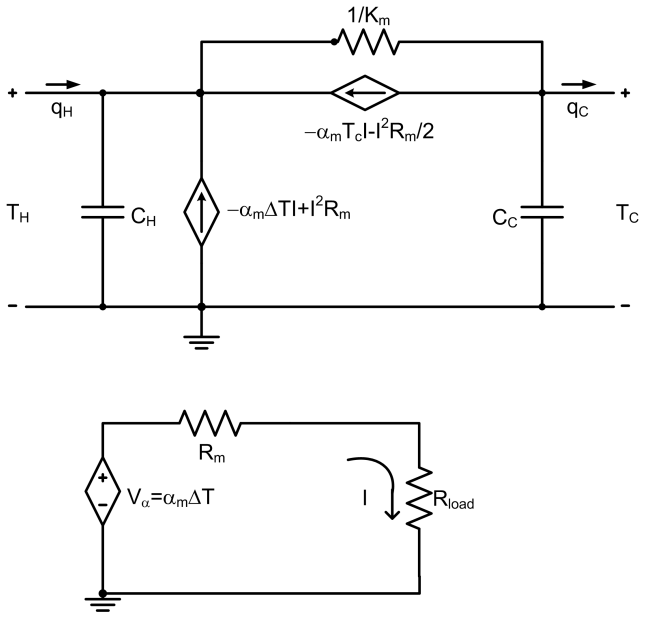

Figure 5.4: Thermogenerator equivalent circuit based in the model of Chavez et al. [1].

$$V_{load} = V_{\alpha} - IR_m \tag{5.10}$$

The open circuit voltage is the Seebeck coefficient for the TEG times the temperature gradient.

$$V_{oc} = \alpha \Delta T \tag{5.11}$$

$$I_{opt} = \frac{\alpha \Delta T}{R\left(m'_{opt} + 1\right)} \tag{5.12}$$

The output power delivered to the load, R_{load}, is:

$$P_o = I^2 R_{load} \tag{5.13}$$

If a transient response of the TEG is not necessary and it is only required a static characterization, the capacitors C_H and C_C can be removed in the equivalent circuit.

5.2 Design Considerations

The first step is the selection of the n- and p-type materials that form the TEM. A parameter to maximize in its design is the thermal efficiency , η_{TEG}, is defined as the ratio of the electrical power output, P_o, to the thermal power absorbed by the hot junction, q_H [49].

$$\eta_{TEG} = P_o/q_H \tag{5.14}$$

The output power is:

$$P_o = I^2 R_{load} \tag{5.15}$$

The current that flows through the electrical load, R_{load}, is:

$$I = \frac{\alpha_m \Delta T}{R_m + R_{load}} \tag{5.16}$$

Therefore, Equation (5.14) can be expressed as:

$$\eta_{TEG} = \frac{I^2 R_{load}}{k_m \Delta T + \alpha_m T_H I - \frac{1}{2} I^2 R_m} \tag{5.17}$$

A new variable m' that relates R_{load} and R_m is introduced in order to calculate how to maximize the thermal efficiency of the TEG.

$$m' = \frac{R_{load}}{R_m} \tag{5.18}$$

Expressing Equation (5.17) as a function of m':

$$\eta_{TEG} = \frac{m' \left(\Delta T / T_H\right)}{\frac{(1+m')^2}{T_H} \frac{R k_m}{\alpha^2} + (1 + m') - \frac{1}{2} \frac{\Delta T}{T_H}} \tag{5.19}$$

If it is considered that all parameters of Equation (5.19) remain constant except the product $R_m k_m$, the smaller this parameter is, the higher efficiency is obtained.

The following analysis relates the product $R_m k_m$ with the dimensions and properties of the thermogenerator material. The thermal conductance of the TEG is:

$$k_m = \lambda_n A_n / l_n + \lambda_p A_p / l_p = \lambda_n \gamma_n + \lambda_p \gamma_p \tag{5.20}$$

where A_n is the cross sectional area of n-type material, A_p is the the cross sectional area of n-type material, l_n is the length of the n-type material, l_p is the cross sectional area of p-type material, λ_n is the thermal conductivity of n-type material [W/(mK)], λ_p is the thermal conductivity of p-type material, γ_n is the ratio A_n/l_n [m] and γ_p is the ratio A_p/l_p.

The internal resistance of the TEG is:

$$R_m = \rho_n/\gamma_n + \rho_p/\gamma_p \tag{5.21}$$

where ρ_n and ρ_p are the electrical resistivity $[\Omega m]$ of the n-type and p-type material, respectively.

$$R_m k_m = \lambda_n \rho_n + \lambda_n \rho_p \left(\gamma_n/\gamma_p\right) + \lambda_p \rho_n \left(\gamma_p/\gamma_n\right) + \lambda_p \rho_p \tag{5.22}$$

Doing the derivative of $R_m k_m$ with respect to γ_n/γ_p and equaling to zero, it is obtained that the minimum value of the product is obtained when:

$$\gamma_n/\gamma_p = \left[\left(\rho_n \lambda_n\right)^{1/2} + \left(\rho_p \lambda_p\right)^{1/2}\right]^2 \tag{5.23}$$

The expression for the figure of merit, Z, of a Peltier element is defined as:

$$Z = \frac{\alpha_m^2}{R_m k_m} = \frac{\alpha_m^2 \Theta_m}{k_m} = \frac{\alpha_m^2 \sigma_m}{\lambda_m} \tag{5.24}$$

The selection of the materials employed to fabricate the thermopair depends on the temperature ranges the thermogenerator must cope with. Altenkirch [113] concluded that good thermoelectric materials have large Seebeck coefficients, α, and electrical conductivity, σ, whereas they have low thermal conductivity, λ. These three variables are related with the figure of merit Z, (5.24).

Another way to define the figure of merit is ZT since Z varies with the temperature. Therefore, the ideal materials for a TEG employed at ambient temperatures should have a large value of ZT under these working conditions.

The expression for the figure of merit for a combination of materials that form a couple is:

$$Z = \frac{\left(|\alpha_n| + |\alpha_p|\right)^2}{\lambda_n \rho_n + \lambda_n \rho_p \left(\gamma_n/\gamma_p\right) + \lambda_p \rho_n \left(\gamma_p/\gamma_n\right) + \lambda_p \rho_p} \tag{5.25}$$

Substituting in Equation (5.25) the result obtained for $\left(R_m k_m\right)_{min}$ deduced from Equations (5.23) and (5.22), it is obtained the expression for the figure of merit that provides the maximum efficiency of the TEG when its geometry is optimized, $Z*$.

$$Z* = \frac{\left(|\alpha_n| + |\alpha_p|\right)^2}{\left[\left(\rho_n \lambda_n\right)^{1/2} + \left(\rho_p \lambda_p\right)^{1/2}\right]^2} \tag{5.26}$$

These equations fix geometrical conditions to maximize the efficiency of the TEG and therefore, the efficiency can be optimized in the design step. If Equation (5.26) substitutes the value $\alpha_m^2/(R_m k_m)$ in Equation (5.19), it is obtained the thermal efficiency of a TEG that has optimum geometry.

$$\eta_{TEG-maxgeometry} = \frac{m' \left(\Delta T/T_H\right)}{\frac{\left(1+m'\right)^2}{Z^* T_H} + \left(1 + m'\right) - \frac{1}{2}\frac{\Delta T}{T_H}} \tag{5.27}$$

Once the TEG is designed to work with the maximum efficiency, the load resistance can also be properly selected to maximize the efficiency. The optimum value of m', m'_{opt} is obtained doing the derivative of Equation (5.27) with respect to m' and equaling to zero.

$$m'_{opt} = (1 + Z^* T_{av})^{1/2} \tag{5.28}$$

where $T_{av} = (T_C + T_H)/2$

Therefore, if the efficiency is optimized in the design step of the TEG and in the selection of the load, it is obtained the maximum efficiency of the TEG, $\eta_{TEG-max}$.

$$\eta_{TEG-max} = \frac{\left(m'_{opt} - 1\right)(\Delta T/T_H)}{m'_{opt} + T_C/T_H} \tag{5.29}$$

The maximization of the TEG efficiency requires to optimize it in the design phase. However, if it is not possible to do this, an improvement can be done maximizing the output power of the TEG. The output power, P_o, as a function of the resistance ratio m' is expressed as:

$$P_o = \frac{(\alpha_m \Delta T)^2 m'}{(1 + m')^2 R_m} \tag{5.30}$$

The maximum output power is obtained for $m' = 1$ ($R_{load} = R_m$). Thus, the efficiency obtained for maximizing the output power is:

$$\eta_{TEG-maxp} = \frac{\Delta T/T_H}{4/(ZT_H) + 2 - \frac{1}{2}(\Delta T/T_H)} \tag{5.31}$$

The maximum output power is obtained from Equation (5.30) when $m' = 1$:

$$P_{o-max} = \frac{(\alpha_m \Delta T)^2}{4R_m} = \frac{(\alpha_m \Delta T)^2}{4\left[\rho_n l_n/A_n + \rho_p l_p/A_p\right]} \tag{5.32}$$

If it is assumed that $A = A_n + A_p$ and $l_n = l_p = l$, Equation (5.32) can be simplified to:

$$P_{o-max} = \frac{(\alpha_m \Delta T)^2 A}{4l\left[\rho_n + \rho_p\right]} = \frac{(\alpha_m \Delta T)^2 A}{4l\rho} \tag{5.33}$$

From Equation (5.33), it is deduced that the maximum output power generated by a TEG is proportional to A/l where A is the cross-sectional area and l is the length of a p-n thermoelectric leg couple. Therefore, decreasing the length of the thermocouples and increasing their section, the maximum output power generated will be increased. Thus, maintaining the same volume in the TEG, higher output power values can be obtained increasing its area and decreasing its length.

5.3 Characterization of Thermoelectric Modules (TEMs)

The characterization of the TEM is of special interest for the design of the power management unit of the TEG. Once the TEM to employ is characterized, it is possible to predict the voltage and power generated for different temperature gradients, as well as, the internal electrical resistance of the TEG. Moreover, once a power management unit is designed, it can be evaluated the percentage of the total available power that is extracted with the converter.

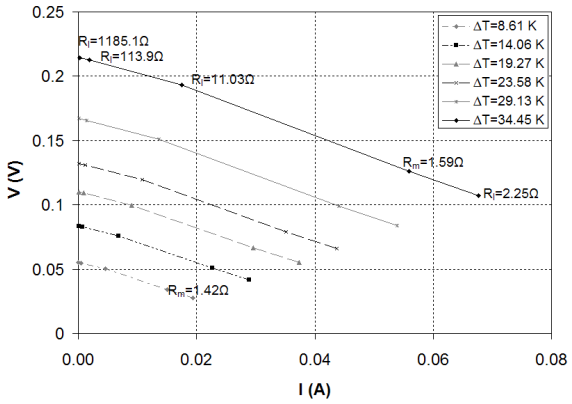

Figure 5.5: Voltage as a function of current for the 17 A 1015 H 200 Peltron thermogenerator.

A TEG can be modeled taking into account three of its parameters: the Seebecks coefficient, α_m, the internal resistance, R_m, and the thermal resistance, Θ_m. The parameters of a TEG can be extracted following the methodology described in [114]. Nevertheless, most of the manufacturers of thermoelectric modules give this information in their datasheets. Sometimes, this information is not available in a direct way and it has to be calculated from another parameters [2, 115]. However, these parameters are dependent of the temperature and this dependence is not taken into account either by the models employed in [1, 2, 115] or by the manufacturers.

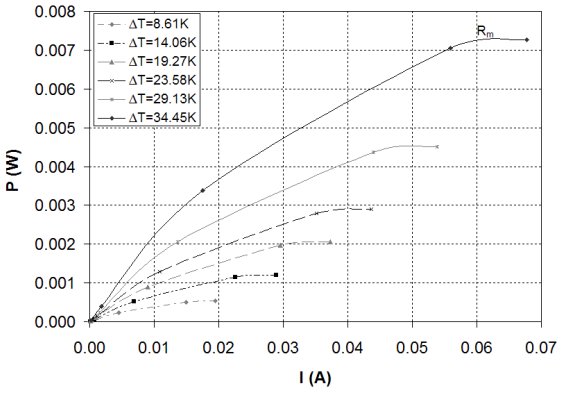

Figure 5.6: Power as a function of current for the 17 A 1015 H 200 Peltron thermogenerator.

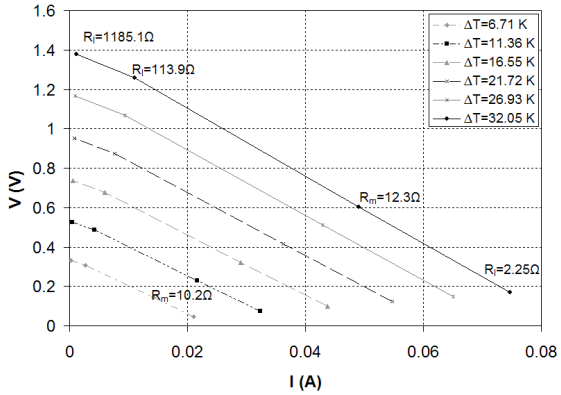

Figure 5.7: Voltage as a function of current for the 128 A 1030 Peltron thermogenerator.

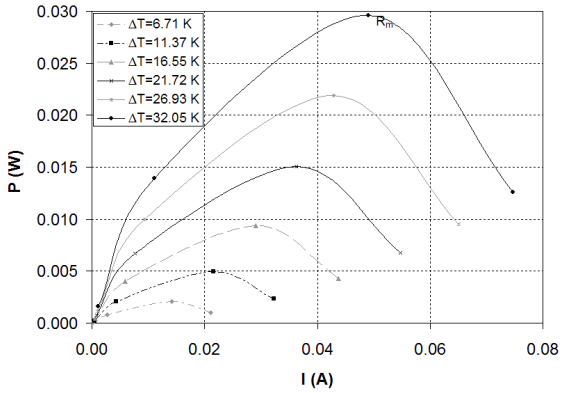

Figure 5.8: Power as a function of current for the 128 A 1030 Peltron thermogenerator.

Table E.1 and Table E.2 included in Appendix E show the measurements obtained employing two different thermogenerators. From these measurements, the parameters α_m and R_m of the TEGs needed to its model can be calculated. The results obtained for the characterization of the two different TEGs [116] are presented in two different figures. Figure 5.5 and Figure 5.7 show the voltage as a function of current for different ΔT for the models 17 A 1015 H 200, 128 A 1030 and 128 A 0020 respectively, whereas Figure 5.6 and Figure 5.8 show the power of the TEG as a function of current for the same values of ΔT. The value of the internal resistance, R_m, of the TEG was calculated for every ΔT and the maximum output power is obtained when the load resistance connected to the TEG is equal to R_m.

The Peltron thermogenerator 128 A 1030 was selected to power the application presented in [22] (Chapter 12) since it delivers higher output power and voltage than the other model for the same temperature gradients. For indoor applications, the temperature gradient between the human body and the ambient will be lower than 6 K, around 3 K-5 K. Then, this TEG, that has a Seebeck coefficient of 49.71 mV/K, is expected that provides a voltage between 149 mV and 249 mV in open circuit with the proposed temperature gradient. When the TEG is delivering the maximum power, its output voltage is half of its open circuit voltage. Thus, if the power management circuit is working in the maximum power point, the output voltage of the TEG will be between 74.5 mV and 124.5 mV.

5.4 Power Management Unit for Thermogenerators

From the results of the characterization of the thermogenerators presented in the previous section, it is found that there is a gap between the output of thermoelectrical energy transducers and the minimum required input voltage of state-of-the- art voltage converters. For example, commercial DC-DC boost regulators have a minimum input voltage of 500 mV [117]. In energy harvesting generators, it is possible to employ a battery or a capacitor to store the energy that is not immediately consumed by the electronic load. However, an energy harvesting system must not be dependent on the energy storage element to be able to start its operation. Therefore, a start-up circuit to assure initial voltage conversion only employing a thermoelectric transducer is included in power management circuit designed in [22, 118] and Chapter 12. The starter circuit consists of a charge-pump in conjunction with a step-up DC-DC converter. The power management unit presented is designed to convert input voltages of the order of few hundreds of millivolts to the voltage supply required by Enocean RF transmitter (3-4 V) employed as a load. However, better results are obtained with a step-up converter based on coupled inductors in terms of efficiency, above 70% for input voltages higher than 300 mV, and lower start-up voltage (116 mV) [119].

The approach presented in [22,118] and Chapter 12 is focused in the design of a power management unit able to operate with the low output voltages obtained with low temperature gradients applied to TEGs. The IMEC has developed a different approach where the main point is the design of an optimum multistage structure for the TEGs. The objective of this configuration is to have a minimum output voltage on the TEG, once it is connected to the power management unit, of 0.7 V that is a value that can be step-up converted by the state of the art converters. Different power management units that are used with this multistage structure have been designed and tested [54, 120, 121]. Moreover, it is tested which location of the wrist is the optimum one for placing a TEG.

5.4.1 Energy Storage Element

An energy storage element can be employed for two reasons. On one hand, it permanently accumulates the available energy delivered by the thermogenerator, even though no continuous power is demanded by the electronic application. On the other hand, if excessive power bursts, e.g. upon start-up or during transmission, are required, they can be drawn out of the energy buffer. Moreover, in the designed circuit, the charge-pump needs in the order of 100 seconds to charge its output capacitor. Therefore, to avoid this delay, the battery can be connected at the beginning as input to the power management circuit.

The output voltage that must be provided by the power management unit depends on the supply voltage range required by the electrical load. The energy storage element must also be selected according to this criterion and the energy

requirements of the load as well. Two possible storage elements are batteries and large capacitors.

- Batteries. For a supply voltage range between 2V and 2.8V two-cell-NiMH [122] or one-cell-lithium-polymer with lithium-titanium-oxide [123] batteries can be taken into account. For higher supply voltages up to 4.2V, typical 3.7V lithium batteries can be selected.
- Capacitors. High value capacitors (Supercaps, Gold Caps, Ultra Caps) can replace the batteries. However, their capacity is generally lower than those of batteries, they don't have a flat discharge curve and the limited voltage rating has also to be considered. An advantage is the higher power density, such that they can withstand higher current pulses.

The selected energy storage element for the power management unit is the battery in order to have the option of reducing the start-up time of the circuit (as it is explained in the next section) connecting the battery to the input of the circuit instead of the TEG.

5.4.2 Power Management Circuit

Figure 5.9 shows the power management circuit designed to power an RF communication module [22, 118] (Chapter 12). This section gives additional data about this circuit that is not presented in (Chapter 12). The main blocks of the power management circuit are a charge pump and a step-up converter. At first moment, the charge-pump is employed to increase the input voltage of the TEG to a value that can be operated by the boost converter.

The charge pump was first tested at several input voltages under no load condition. An external power supply, V_{in} was employed as input energy source. The recorded input currents, I_{in}, for the charge-pump are shown in Table 5.2. An external power supply V_{in} was also employed as input energy source while the output of the step-up converter was adjusted to 2.8 V in order to calculate the efficiency of the power management unit, see Table 5.3, attached to two-cell NiMH battery pack with an open circuit overall voltage of 1.8 V. I_{bat} corresponds to the current flowing into the battery.

Table 5.2: Measurements of the input voltage and charge-pump current consumption.

$V_{in}(mV)$	I_{in}
300	350μA
250	1.5mA
200	3.5mA
150	2.6mA
140	6mA
130	6.4mA

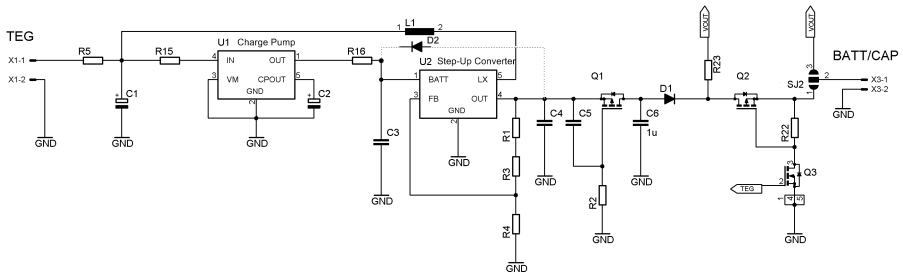

Figure 5.9: Low-input voltage power management circuit.

Table 5.3: Measurements of the input voltage and current, output voltage and current of the switching regulator and efficiency with an external power supply.

$V_{in}(mV)$	$I_{in}(mA)$	$V_{out}(V)$	$I_{bat}(\mu A)$	$\eta(\%)$
300	10.33	2.44	897	70.63
250	9.8	2.42	659	65.09
200	9.35	2.408	436	56.14
150	8.8	2.381	227	40.95
140	8.66	2.374	186	36.42
130	8.45	2.365	146	31.43

Table 5.4: Measurements of the TEG voltage and current, output voltage and current of the switching regulator and efficiency with a thermogenerator power supply for a regulated output voltage of 2.5 V.

$V_{in}(mV)$	$I_{in}(mA)$	$V_{out}(V)$	$I_{bat}(\mu A)$	$\eta(\%)$
265	10.16	2.49	695	64.28
254	10	2.476	645	62.87
246	9.76	2.43	646	65.38
236	9.88	2.489	550	58.71

Table 5.5: Measurements of the TEG voltage and current, output voltage and current of the switching regulatorand efficiency with a thermogenerator power supply for a regulated output voltage of 3.8 V.

$V_{in}(mV)$	$I_{in}(mA)$	$V_{out}(V)$	$I_{bat}(\mu A)$	$\eta(\%)$
400	9.15	3.77	346	35.63
300	13.28	3.745	344	32.34
250	17	3.695	339	29.47
220	16.01	3.33	306	28.93
150	8.69	2.058	189	29.83

Parameter	**Symbol**	**Conditions**	**Min**	**Typ**	**Max**	**Unit**
Min. Input Voltage (after startup)	V_{in}	Battery connected, V_{out}=3.8 V		0.12		V
		No battery connected, V_{out}=3.8 V, no load		0.22		V
		No battery connected, V_{out}=3.8 V, output load 10 kΩ		0.28		
		No battery connected, V_{out}=2 V, no load		0.13		V
		No battery connected, V_{out}=2 V, output load 10 kΩ		0.17		V
Minimum input voltage at startup	V_{in}	No battery connected		0.29		V
Startup time	$t_{startup}$	No battery connected, V_{out}=3.8 V				
		V_{in}=0.29 V	100		150	s
		V_{in}=0.4 V	6		15.8	s
		V_{in}=0.5 V	2.4		5.1	s
Max. Input Voltage	V_{in}			5.5		V
Output voltage range	V_{out}		2		5.5	V
Quiescent current		V_{in}=0.5 V V_{out}=2V		0.8		mA
		V_{in}=0.5 V V_{out}=3.8		3.2		mA
		V_{in}=0.3 V V_{out}=2V		1.3		mA
		V_{in}=0.3 V V_{out}=3.8V		7		mA

Table 5.6: Electrical characteristics of the Power Management Unit

The external supply was replaced by the 128 A 1030 thermoelectric module from Peltron. By means of human body to ambient temperature difference the circuit was powered-up after around 100 seconds providing a regulated output of 2.8 V. Upon power-up, the output voltage of the TEG dropped from 350mV to 250mV. The step-up converter kept regulating down to an input voltage of 150mV. Table 5.4 and 5.5 shows the measured data as well as the calculated efficiency output voltages of 2.5 V and 3.8 V, respectively. The efficiency of the converter is lower for the case of the output voltage fixed at 3.8 V. Moreover, the output voltage in this case is not regulated when the TEG provides an output voltage lower than 250 mV.

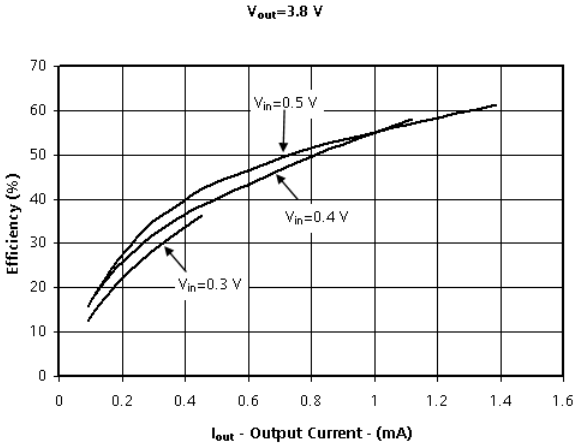

Figure 5.10: Efficiency versus output current for V_{out}=2V

Table 5.6 summarizes the electrical characteristics of the designed power management unit while Figures 5.10 and 5.11 show the efficiency versus output current for an output voltage of 3.8 V and 2 V. The curves of both figures stop at a point where the power management circuit was not regulating its output anymore for the load connected. First row of Table 5.6 show the values of the minimum input voltage at which the power management circuit kept regulating for different output voltages. The minimum input voltage after startup decreases with the output voltage and increases with the value of the load connected. The typical minimum input voltage for starting to operate the converter circuit is 290 mV after 100 s to 150 s. The startup time decreases with input voltage dramatically, e.g. for an input voltage of 400 mV, the startup time is between 6 s and 15.8 s.

It is possible to connect the power management circuit to a battery in order to charge it. However, this connection does not require to make use of a conventional battery charger (that includes a current-limit, a voltage-limit regulation loop and a time-limited charge termination circuit) and thus energy and area can be saved. A current-limit regulation loop is usually required to

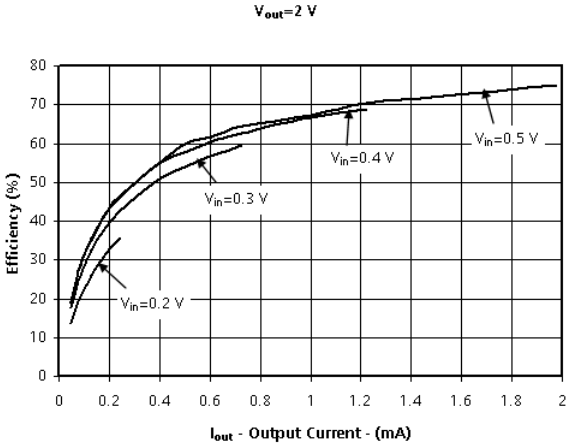

Figure 5.11: Electrical characteristics of the Power Management Unit

avoid overcharging during the fast charging stage of NiMH and lithium batteries [94]. The designed circuit takes advantage of the intrinsic current limiting characteristics of the TEG for charging the battery without the need of dedicated hardware. Additionally, the voltage-limit regulation loop is undertaken by the boost DC-DC converter since it provides the required charging voltage at the output of the power management unit. Time-limited charge termination circuitry is also avoided by selecting a regulated voltage slightly below the maximum topping voltage specified by battery manufacturers. A battery charger is replaced though by a diode, $D1$, connected between the output of the regulator and the battery. This approach is more advisable for lithium-polymer than for NiMH accumulators, since the latter suffer from memory effect degradation when the charging procedure is not completed. This topology can be enhanced in terms of reliability by placing a Zener diode that limits the charging voltage in case of failure. It is also possible to connect the battery to the input of the power management circuit in order to reduce the startup time and afterwords connect the TEG as input voltage for the power management circuit.

More detailed information about the power management unit and the application designed to power a wireless communication data that is able to sense and transmit information once every second is given in [22, 118] (Chapter 12).

Chapter 6

System-level Simulation

The amount of available power in a system that employs an energy harvesting transducer as a power supply is limited and it is not constant with time. If an energy storage element is employed, the requirement to fulfill is to generate enough energy to supply the electronic load connected to the energy harvesting system.

The evolution in the area of microprocessors and transceivers has made possible communication modules with different power consumption modes depending on its state. There are several power consumption modes: standby, transmission, reception, sleep, etc. and some of them need a minimum time to be operative.

In a given time interval, it is desirable to make equal the energy harvested by the generator and the energy consumed by the load to assure an energy neutral operation, in other words, to assure that there will always be available energy to supply the load. This is the same as stating that the average power in the time interval generated and spent must be the same for neutral operation. A system-level simulation allows to design and modify a complete system (from the transducer to the load) that employs energy harvesting power supplies in the same simulation environment. Furthermore, it is possible to simulate how a modification in the transducer affects the available energy for supplying power to the load. During the thesis, two different simulation environments that combine mechanical and electrical models have been developed. An inductive generator model was analyzed in [21] (Chapter 11) employing the Ptolemy simulator whereas a piezoelectric generator model described with Verilog-A was presented in [13] (Chapter 13). Both system-level simulations are done in the time domain instead of the frequency domain.

Each one of the blocks that compose the complete system-level simulation of [13] (Chapter 13) must be modeled and included in the simulation of the complete energy harvesting generator. The energy transducer (a piezoelectric transducer), the voltage regulator (a linear regulator) and the electronic load (an RF transmitter) are modeled at a behavioral level whereas the battery and the converter were modeled at a circuit level.

The power consumption profile of the electronic load can be changed in two different ways. The first one is the replacement of some hardware of the communication module (microprocessor, transceiver,) and the second one is a change in the power consumption mode of the communication module.

6.1 Energy Harvesting Transducer and Load Energy Profile

In the section titled *7. Power Conditioning Circuits* of [18] (Chapter 8), the two operation modes of an electronic load powered by an energy harvesting generator are explained: continuous and intermittent. An energy storage element is not necessary if the power consumption of the electronic device is lower than the power generated by the energy harvesting generator and is only operated when there is generated power. For the rest of the cases, an energy storage element is necessary , e.g. a battery.

The application and the harvested and consumed energy will determine the operating mode to select. The objective of this chapter is to present a way to calculate the initial charge of the storage element before starting operation as well as, the maximum quantity of energy that is required to store. The method is based on the works made by Kansal et al. presented in [124] and [30]. This technique consists of a model to characterize environmental sources and electronic loads that allows to determine the size of the energy storage element employed as a function of the power consumption profile of the load to assure energy neutral operation.

When the difference between the last maximum and minimum of the mean power delivered by the energy harvesting transducer to the energy storage device is Δ, this means that the error to calculate the energy neutral operation point has an error margin of $\pm\Delta$ and that no more stored power data are necessary [124]. Therefore, this method is feasible for periodical or quasi-periodical energy harvesting sources but not for non-periodical ones. Kansal et al. developed this method for solar panels in outdoors applications where there is power available only under sunlight and the cycles of converted power caused by day and night alternation are quasi-periodic. Nevertheless, this behaviour is not limited to solar energy since mechanical energy sources or thermal energy sources can also be periodical or quasi-periodical.

First of all, it is necessary to define the energy delivered by the transducer to the energy storage element and the energy consumed by the load in a mathematical way. Figure 6.1 shows the power harvested by an energy harvesting transducer and delivered to the energy storage element, P_s, as a function of time. The mean power, ρ_s, is defined as

$$\rho_s = \frac{1}{T}\int_T P_s(t)\mathrm{d}t \tag{6.1}$$

where T is the interval of time considered for the calculations that gives an error of $\pm\Delta$.

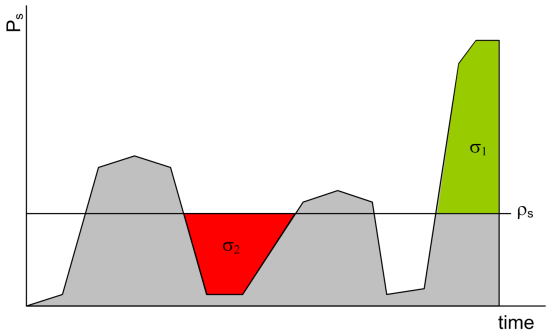

Figure 6.1: Power delivered by the energy harvesting transducer to the energy storage element as a function of time.

If it is assumed that T_{lows-i} is the $i-th$ contiguous time duration for which $P_s(t) \leq \rho_s(t)$, then σ_2 is defined as the maximum deficit of energy of the energy harvesting transducer, see Figure 6.1.

$$\sigma_2 = max_i \left\{ \int_{T_{lows-i}} \rho_s - P_s(t)\mathrm{d}t \right\} \tag{6.2}$$

If it is assumed that $T_{highs-i}$ is the $i-th$ contiguous time duration for which $P_s(t) \geq \rho_s(t)$, then σ_1 is defined as the maximum excess of energy of the energy harvesting transducer, see Figure 6.1.

$$\sigma_1 = max_i \left\{ \int_{T_{highs-i}} P_s(t) - \rho_s\mathrm{d}t \right\} \tag{6.3}$$

The energy harvested by the transducer and delivered to the energy storage element will be inside a certain margin limited by E_{smin} and E_{smax}:

$$E_{smin} \leq \int_T P_s(t)\mathrm{d}t \leq E_{smax} \qquad \forall\ t \tag{6.4}$$

where E_{smin} is the lower limit and E_{smax} is the upper limit of the energy delivered by the energy harvesting transducer to the energy storage element. $E_{smin}(T)$ and $E_{smax}(T)$ are piecewise functions defined as:

$$E_{smin}(T) = \begin{cases} \rho_s T - \sigma_2 \frac{T}{T_{lows-i}} & \forall T \leq T_{lows-i}, \\ \rho_s T - \sigma_2 & \forall\ T \geq T_{lows-i}. \end{cases} \tag{6.5}$$

$$E_{smax}(T) = \begin{cases} \rho_s T + \sigma_1 \frac{T}{T_{highs}} & \forall\ T \leq T_{highs-i}, \\ \rho_s T + \sigma_1 & \forall t \geq T_{highs-i}. \end{cases} \tag{6.6}$$

Figure 6.2 shows the power consumption of an electronic load,P_l, as a function of time. ρ_l is the average power consumption of the load. P_1 is the power

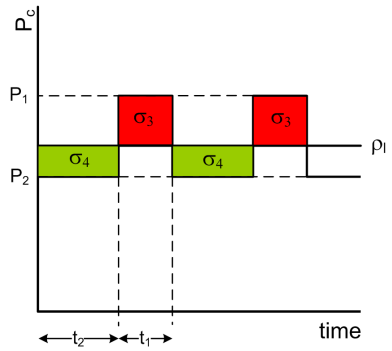

Figure 6.2: Power consumption of the load as a function of time.

consumption of the load in the highest power consumption mode (e.g., transmission mode in a communication module) and it takes place during a time interval t_1. P_2 is the power consumption of the load in the lowest power consumption mode (e.g., standby mode in a communication module) and it takes place during a time interval t_2. Therefore, the electronic load consumption can be defined as a function of the parameters $(\rho_l, \sigma_3, \sigma_4)$.

$$\rho_l = \frac{1}{T}\int_T P_l(t)\mathrm{d}t \tag{6.7}$$

If it is assumed that $T_{highs-i}$ is the $i-th$ contiguous time duration for which $P_l(t) \geq \rho_l(t)$, then σ_3 is defined as the maximum overconsumption of energy made by the load, see Figure 6.2.

$$\sigma_3 = max_i \left\{ \int_{T_{highl-i}} P_l(t) - \rho_l \mathrm{d}t \right\} \tag{6.8}$$

If it is assumed that $T_{highs-i}$ is the $i-th$ contiguous time duration for which $P_l(t) \geq \rho_l(t)$, then σ_4 is defined as the maximum less consumption of energy made by the load, see Figure 6.2.

$$\sigma_4 = max_i \left\{ \int_{T_{lowl-i}} \rho_l - P_l(t)\mathrm{d}t \right\} \tag{6.9}$$

The lower and upper limits of the energy consumed by the electronic load are:

$$E_{lmin}(T) = \begin{cases} \rho_l T - \sigma_4 \frac{T}{T_{lowl-i}} & \forall\ T \leq T_{lowl-i}, \\ \rho_l T - \sigma_4 & \forall\ T \geq T_{lowl-i}. \end{cases} \tag{6.10}$$

$$E_{lmax}(T) = \begin{cases} \rho_l T + \sigma_3 \frac{T}{T_{highl-i}} & \forall\ T \leq T_{highl-i}, \\ \rho_l T + \sigma_3 & \forall\ T \geq T_{highl-i}. \end{cases} \tag{6.11}$$

6.2 General Conditions for Energy Neutral Operation

When a wearable device, e.g., a node of a WSN, employs an energy harvesting system to be powered, the objective to achieve is to eliminate the need to replace or recharge externally their battery. Thus, it is necessary to assure energy neutral operation or in other words, to assure that the battery will have always the energy required by the electronic device. Thus, the energy storage element is defined with two parameters that are its initial charge when it is connected to the energy harvesting system, B_0, and the amount of energy that can be stored, B. The value of both parameters are calculated in this section.

In order to achieve energy neutral operation, the total energy in the system, ΣE, has to be greater than zero since the energy harvesting transducer, E_s, plus the initial energy stored in the battery, B_0 has to be greater than the energy consumed by the electronic load, E_l. Moreover, it is desirable in an energy harvesting system to assure that no energy is wasted or that the battery is damaged due to overcharge. These two conditions can be expressed as:

$$\Sigma E \geq 0 \tag{6.12}$$

$$\Sigma E \leq B \tag{6.13}$$

The available energy in the system is equal to the initial energy stored in the battery plus the energy harvested by the transducer minus the energy consumed by the load and minus the leakage energy due to the energy storage element.

$$\Sigma E = B_0 + E_s - E_l - \int_T P_{leak} T \mathrm{d}t \tag{6.14}$$

where P_{leak} is the leakage power of the energy storage element.

The value of B_0 can be calculated using the condition expressed by Equation (6.12). This condition is evaluated when the worst case takes place, that is when the generated energy by the harvesting transducer to the energy storage device is minimum, E_{smin}, and the energy consumed by the electronic load is maximum, E_{lmax}.

$$B_0 + E_{smin} - E_{lmax} - \int_T P_{leak} T \mathrm{d}t \geq 0 \tag{6.15}$$

The above condition can be expressed as:

$$B_0 + E_{smin} - E_{lmax} - \rho_{leak} T \geq 0 \tag{6.16}$$

where ρ_{leak} is the mean leakage power of the energy storage element.

In a similar way, the value of B can be calculated using the condition expressed by Equation (6.13). This condition is evaluated when the worst case takes place, that is when the generated energy by the harvesting transducer

is maximum, E_{smax}, and the energy consumed by the electronic load is minimum, E_{lmin}. In this case, the energy storage element will have at its maximum capacity.

$$B_0 + E_{smax} - E_{lmin} - \int_T P_{leak} T \mathrm{d}t \leq B \tag{6.17}$$

The above condition can be expressed as:

$$B_0 + E_{smax} - E_{lmin} - \rho_{leak} T \leq B \tag{6.18}$$

If the value of T tends to infinity for the two conditions expressed by Equation (6.16) and Equation (6.18), it is obtained:

$$\rho_s - \rho_l - \rho_{leak} \geq 0 \tag{6.19}$$

$$\rho_s - \rho_l - \rho_{leak} \leq 0 \tag{6.20}$$

Equation (6.19) and Equation (6.20) can be simplified as:

$$\rho_s - \rho_l - \rho_{leak} = 0 \tag{6.21}$$

Substituting in Equation (6.16), the value given for E_{smin} and E_{lmax} by Equation (6.5) and Equation (6.11), respectively, and taking into consideration the previous expression, it is obtained:

$$\begin{aligned} &B_0 - \sigma_2 \frac{T}{T_{lows}} - \left(\sigma_3 \frac{T}{T_{highl}} \right) \geq 0 \\ &\forall\ T \leq T_{lows} \text{ and } \forall\ T \leq T_{highl} \end{aligned} \tag{6.22}$$

$$\begin{aligned} &B_0 - \sigma_2 \frac{T}{T_{lows}} - (\sigma_3) \geq 0 \\ &\forall\ T \leq T_{lows} \text{ and } \forall\ T \geq T_{highl} \end{aligned} \tag{6.23}$$

$$\begin{aligned} &B_0 - \sigma_2 - \left(\sigma_3 \frac{T}{T_{highl}} \right) \geq 0 \\ &\forall\ T \geq T_{lows} \text{ and } \forall\ T \leq T_{highl} \end{aligned} \tag{6.24}$$

$$\begin{aligned} &B_0 - \sigma_2 - (\sigma_3) \geq 0 \\ &\forall\ T \geq T_{lows} \text{ and } \forall\ T \geq T_{highl} \end{aligned} \tag{6.25}$$

There are two conditions that give as a result the worst scenario and therefore, the minimum value of B_0. One of these conditions occurs when T is equal to T_{lows} and this value is greater than T_{highl}. The second condition occurs when

T is equal to T_{highl} and this value is greater than T_{lows}. For both cases the same expression is obtained:

$$\begin{aligned} &B_0 \geq \sigma_2 + \sigma_3 \\ &\forall\ T = T_{lows} \text{ and } \forall\ T \geq T_{highl} \\ &\forall\ T = T_{highl} \text{ and } \forall\ T \geq T_{lows} \end{aligned} \tag{6.26}$$

When the conditions given by Equation (6.26) and Equation (6.21) are accomplished, the energy harvesting system can operate forever.

The conditions to avoid overcharging the energy storage element are obtained substituting in Equation (6.18), the value given for E_{smax} and E_{lmin} by Equation (6.6) and Equation (6.10), respectively, it is obtained a piecewise expression:

$$\begin{aligned} &B_0 + \sigma_1 \frac{T}{T_{highs}} - \left(-\sigma_4 \frac{T}{T_{lowl}}\right) \leq B \\ &\forall\ T \leq T_{highs} \text{ and } \forall\ T \leq T_{lowl} \end{aligned} \tag{6.27}$$

$$\begin{aligned} &B_0 + \sigma_1 \frac{T}{T_{highs}} - (-\sigma_4) \leq B \\ &\forall\ T \leq T_{highs} \text{ and } \forall\ T \geq T_{lowl} \end{aligned} \tag{6.28}$$

$$\begin{aligned} &B_0 + \sigma_1 - \left(-\sigma_4 \frac{T}{T_{lowl}}\right) \leq B \\ &\forall\ T \geq T_{highs} \text{ and } \forall\ T \leq T_{lowl} \end{aligned} \tag{6.29}$$

$$\begin{aligned} &B_0 - \sigma_2 - (\sigma_3) \leq B \\ &\forall\ T \geq T_{highs} \text{ and } \forall\ T \geq T_{lowl} \end{aligned} \tag{6.30}$$

The maximum amount of stored energy B will occur when the maximum delivered energy by the transducer and the minimum spent energy by the load are coincident in time. In this case, it is obtained the expression:

$$B_0 + \sigma_1 + \sigma_4 \leq B \tag{6.31}$$

Combining (6.26) and (6.31), it is deduced that:

$$\sigma_1 + \sigma_2 + \sigma_3 + \sigma_4 \leq B \tag{6.32}$$

When this condition is accomplished, then no waste energy is produced from the energy harvesting transducer since all the energy generated can be stored in the energy buffer.

6.2.1 Conditions for Energy Neutral Operation with two Power Consumption Modes

The electronic load is defined in terms of ρ_l, σ_3 and σ_4 whereas the energy harvesting transducer is defined in terms of ρ_s, σ_1 and σ_2. However, the consumption of the load can be chosen. This selection is made to assure that there will be enough energy in the system to power the load. Nowadays, it is possible that electronic loads like microprocessors and RF transceivers work in different power consumption modes. Therefore, if the electronic load is for example a communication module, it is possible to adapt its power consumption to the harvested energy by the transducer. This adaptation can be made in terms of the duration of a certain mode (sleep mode, stand by mode, transmission mode, reception mode, etc.) and the combination of the available operating modes. This section analyzes how to adapt the electronic load to the available harvested energy.

For this first approach, it is assumed that the electronic load works with two different consumption modes: P_1 and P_2 ($P_1 > P_2$), each one with a duration t_1 and t_2, respectively. The consumption profile shown in Figure 6.2 is repeated with period τ. Next section gives a more general analysis with N different consumption modes for the electronic load.

The mean power consumed by the load, ρ_l, is:

$$\rho_l = x_1 P_1 + x_2 P_2 \tag{6.33}$$

where $x_2 = 1 - x_1$, $t_1 = x_1\tau$ and $t_2 = x_2\tau$.

The contiguous time duration for which $P_l(t) \geq \rho_l(t)$ is t_1. Therefore, σ_3 is expressed as:

$$\sigma_3 = \int_{t_1} (P_1 - \rho_l)\,\mathrm{d}t \tag{6.34}$$

Substituting in the above equation the value of ρ_l given in Equation (6.33), it is obtained:

$$\sigma_3 = (1 - x_1)\, x_1 \tau\, (P_1 - P_2) \tag{6.35}$$

In a similar way, it is obtained the value for σ_4:

$$\sigma_4 = (1 - x_1)\, x_1 \tau\, (P_1 - P_2) \tag{6.36}$$

To assure energy neutral operation, the value of ρ_l must be equal to ρ_t minus $\rho_{leakage}$. Taking this fact into account as well as the fact that the values for P_1 and P_2 are fixed by the electronic load selected, the value of x_1 can be calculated.

$$x_1 = \frac{\rho_s - \rho_{leak} - P_2}{P_1 - P_2} \tag{6.37}$$

Thus, the value of x_2 is:

$$x_2 = \frac{P_1 - \rho_s + \rho_{leak}}{P_1 - P_2} \tag{6.38}$$

Once the value of x_1 is calculated, the value of B, B_0 and τ must be selected in a compromise way that allows proper operation of the electronic load and the selection of an energy storage elements that fit with the requirements of the system (for example, in terms of dimensions and weight). There is a minimum time needed for the tasks associated to power consumption P_1 and P_2 that must be respected in order to allow the proper operation of the load. Therefore, a minimum value for τ is fixed by the requirements of the load.

$$t_1 \geq x_1 \tau_{min} \tag{6.39}$$

$$t_2 \geq x_2 \tau_{min} \tag{6.40}$$

For the case of only two different consumption modes, σ_3 is equal to σ_4 and thus, the conditions for the battery capacity and initial charge are:

$$\sigma_1 + \sigma_2 + 2\,(1 - x_1)\,t_1\,(P_1 - P_2) \leq B \tag{6.41}$$

$$\sigma_2 + (1 - x_1)\,t_1\,(P_1 - P_2) \leq B_0 \tag{6.42}$$

6.2.2 Conditions for Energy Neural Operation with N Power Consumption Modes

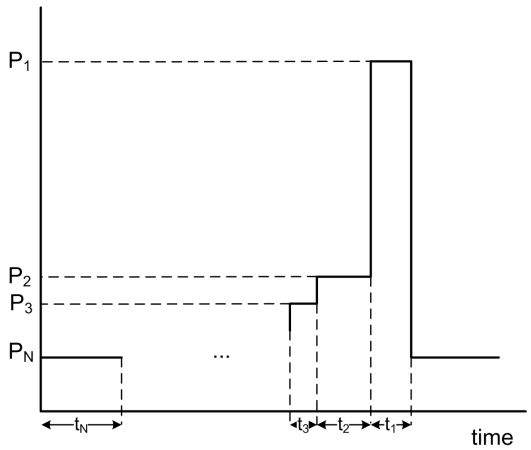

Figure 6.3: Power consumption of the load as a function of time.

Figure 6.3 shows a load with N different power consumption modes. P_N is the lowest power consumption mode whereas P_1 is the highest power consumption mode. The rest of the power consumption modes between these two values increase consecutively their power consumption from P_N to P_1. When this assumption is accepted, for the general case of N different consumption modes, it is calculated that:

$$\tau = \sum_{i=1}^{N} x_i \tau \tag{6.43}$$

where τ is period of the power consumed by the load and x_i is the percentage of τ where the power consumed by the load is P_i.

$$\rho_l = \sum_{i=1}^{N} P_i x_i \tag{6.44}$$

The expressions for σ_3 and σ_4 are:

$$\sigma_3 = \tau \left((P_1 - \rho_l)\, x_1 + \sum_{i=2}^{N-1} \langle P_i - \rho_l \rangle\, x_i \right) = \tau \sum_{i=1}^{N} \langle P_i - \rho_l \rangle\, x_i \tag{6.45}$$

$$\sigma_4 = \tau \left((\rho_l - P_N)\, x_N \sum_{i=2}^{N-1} \langle \rho_l - P_i \rangle\, x_i \right) = \tau \sum_{i=1}^{N} \langle \rho_l - P_i \rangle\, x_i \tag{6.46}$$

The addition of σ_3 and σ_4 gives as a result:

$$\begin{aligned} \sigma_3 + \sigma_4 &= \tau \left(\sum_{i=1}^{N} \langle \rho_l - P_i \rangle\, x_i + \sum_{i=1}^{N} \langle P_i - \rho_l \rangle\, x_i \right) \\ &= \tau \left((P_1 - \rho_l)\, x_1 \sum_{i=2}^{N-1} \langle \rho_l - P_i \rangle\, x_i + \sum_{i=2}^{N-1} \langle P_i - \rho_l \rangle\, x_i + (\rho_l - P_N)\, x_N \right) \end{aligned} \tag{6.47}$$

$(\rho_l - P_N)\, x_N \tau$ can be expressed as a function of the rest of the power consumption modes:

$$\begin{aligned} (\rho_l - P_N)\, x_N \tau &= \rho_c T \left(1 - \sum_{i=1}^{N-1} x_i \right) - P_N x_N T \\ &= \left(\sum_{i=1}^{N-1} (P_i - \rho_c)\, x_i \right) \tau \end{aligned} \tag{6.48}$$

Therefore, substituting the above expression in Equation 6.47, it is obtained:

$$\sigma_3 + \sigma_4 = 2\tau \sum_{i=1}^{N-1} \langle \rho_l - P_i \rangle \, x_i \tag{6.49}$$

Therefore, the conditions to be fulfilled for energy neutral operation by a electronic load with N consumption modes are summarized here employing expressions (6.26) and (6.32).

$$\sigma_2 + T \sum_{i=1}^{N-1} \langle P_i - \rho_l \rangle \, x_i \leq B_0 \tag{6.50}$$

$$\sigma_1 + \sigma_2 + 2T \sum_{i=1}^{N-1} \langle P_i - \rho_l \rangle \, x_i \leq B \tag{6.51}$$

6.3 System-level Simulation Example

A complete system-level simulation is shown in [13]. The schematic of the electronic circuit simulated, see Figure 6.4, is composed by five different blocks which have their functionality described with Verilog-A. The block called *triangpos* has a description of the deflection done by the piezoelectric element. The second block, $piezofilm$, contains a description of the behavior of a triangular cantilever with a concentrated load applied at its end and composed with piezoelectric and non-piezoelectric material. Between the two output terminals of the block $piezofilm$, it is obtained the voltage generated by the bending beam. The variables of these two blocks have an appropriate value for simulating the step of a person walking. Then, a voltage doubler is employed as rectifier with Schottky diodes. Afterwards, a capacitor stores the energy delivered by the piezoelectric bending beam. The block *GenRegulator* is a linear regulator that when it is active charges the battery. The electronic device selected as electronic load is an RF transmitter.

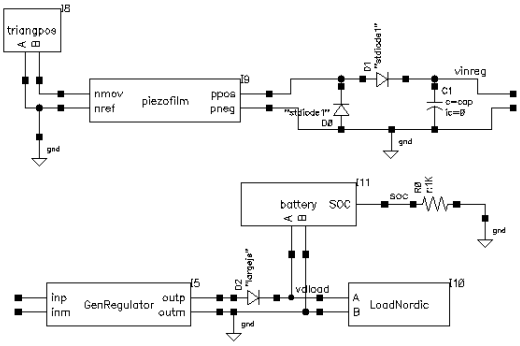

Figure 6.4: Schematic of a battery-powered RF transmitter

The simulation is first done without a load connected in order to measure ρ_s, σ_1 and σ_2. Therefore, the mean power delivered by the energy harvesting transducer to the energy storage device is measured with the voltage doubler and the linear regulator connected. In this way, it is not necessary any assumption about the efficiency of the electronics which depends on the voltage and current delivered by the transducer and the fixed input and output voltages for the operation of the linear regulator. This kind of simulation environment allows to make a complete simulation of an energy harvesting system. Thus, it is possible to predict for example, when the electronic load is a RF transmitter module, how often it is achievable to transmit data without discharging the battery, how changes in the piezoelectric element modify the electrical energy generated and calculate the appropriate parameters of the battery to employ. A second simulation with the load, a transmitter module, connected is done in order to prove the theoretical analysis done with the calculated parameters.

Table 6.1: Parameters employed for the simulation.

Parameter	Value
SOC_i	500 mV
W_0	30 mm
t_s	1 mm
n	10
L	30 mm
$vreg$	3.2 V
$vlimsup$	10 V
$vliminf$	vreg+0.1 V
$R_{int-reg}$	150 mΩ
T	400 ms
t_r	350ms
t_f	125ms
$iconsreg$	10μA
$cintreg$	10μF
cap	10μF
$amplm$	6mm
C_{BAT}	2mAh

The parameters employed for the simulation are summarized in Table 6.1 where SOC_i corresponds to the initial state of charge of the battery, W_0 is the width of the piezoelectric beam, t_s is the thickness of the non piezoelectric material that composes the beam, T is the period of the triangular mechanical excitation, t_r is the rise time for the mechanical excitation, t_f is the fall time of the mechanical excitation, n is the number of piezoelectric films connected in series, $vreg$ is the minimum voltage needed by the linear regulator, $vliminf$ is the minimum voltage at which the energy transducer gives electrical energy to the battery and the load, $vlimsup$ is the maximum voltage at which the capacitor is charged, $iconsreg$ is the consumption of the linear regulator, $cintreg$

is the internal capacitor of the linear regulator and *cap* is the value of the capacitor connected after the voltage doubler and before the linear regulator. Employing the parameters shown in Table 6.1, it is obtained a value of ρ_s= 14.88 μW. Therefore, the power that is delivered from the transducer to the battery is known.

The power consumption profile of the load is always a well known data. The wireless transmitter employed in the simulations has a power consumption in sleep mode, P_{sleep}, of 5.79 μW and a power consumption in transmission mode, P_{Tx}, of 27 mW. The minimum transmission time, T_x, required is 300μs whereas the time between transmissions, τ, will be calculated taking into account the energy delivered by the transducer. If it is considered that the mean leakage power of the battery is zero, the power generated by the transducer and consumed by the load must be equal, see Equation 6.21, $\rho_l = \rho_s$, the following expression relates the mean power generated by the energy harvesting transducer with the parameters of the load.

$$\rho_l = \frac{1}{\tau}\left[P_{Tx}Tx + P_{sleep}\left(\tau - Tx\right)\right] \tag{6.52}$$

From Equation (6.52) it is deduced that time between transmissions, τ, is:

$$\tau = \frac{\left(27mW - 5.79\mu W\right)0.3ms}{14.88\mu W - 5.79\mu W} = 891ms \tag{6.53}$$

The values of σ_3 and σ_4 are calculated in Equations 6.54 and 6.55.

$$\sigma_3 = \left(P_{Tx} - \rho_s\right)Tx = \left(27mW - 14.88\mu W\right)0.3ms = 8.1\mu J \tag{6.54}$$

$$\begin{aligned}\sigma_4 &= \left(\rho_s - P_{sleep}\right)\left(\tau - Tx\right) = \\ &= \left(14.88\mu W - 5.79\mu W\right)\left(891ms - 0.3ms\right) = 8.1\mu J\end{aligned} \tag{6.55}$$

With the data extracted from the simulation done without load connected to the energy harvesting system, the values of σ_1 and σ_2 are calculated employing Equation 6.3 and Equation 6.2, respectively. The values obtained are σ_1=127 μJ and σ_2=185.1 μJ. Therefore, applying Equation 6.41 and Equation 6.42, the parameters of the battery are calculated. The values obtained are $B \geq$330.28 μJ and $B_0 \geq$194.19 μJ. Thus, C_{BAT} and SOC_i can be deduced employing Equations (6.56) and (6.57), respectively.

$$C_{BAT} = \frac{3600B}{V_{dload}} \tag{6.56}$$

$$SOC_i = \frac{3600B_0}{V_{dload}C_{BAT}} \tag{6.57}$$

However, the values chosen for the initial state of charge of the battery, SOC_i, and the capacity of the battery, C_{BAT}, were different, see Table 6.1,

since the values obtained were very small and the values to use just must be greater than these values. 2 mAh of capacity is a value for lithium coin batteries. Simulations with values of SOC_i and C_{BAT} close to the minimum ones are done later. The simulation results with the parameters of Table 6.1 and an RF transmitter connected as a load are shown in Figures 6.5 and 6.6. From these simulation results it is deduced that the time between transmission is the appropriated one since the state of charge of the battery almost remains constant as well as the voltage on the battery. The transmissions are done periodically every 891 ms from the first moment.

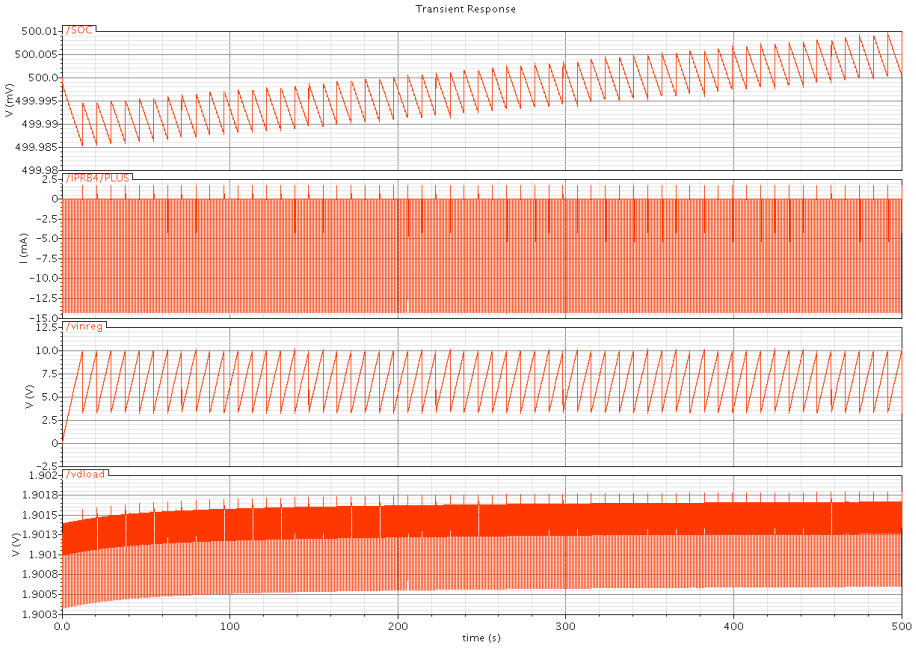

Figure 6.5: Simulation results with load for the parameters summarized in Table 6.1. The waveform called *SOC* shows the state of charge of the battery with a voltage range from 0 to 1 V. $IRPB4$ is the current flowing into the battery. *vinreg* is the voltage at the input of the linear regulator and *vdload* is the voltage of the battery that is supplied to the RF transmitter.

Another simulation has been realized. The number of piezoelectric elements connected in parallel has been doubled from the previous simulation but the period of the mechanical excitations has been tripled. The results obtained from this simulation are summarized in Table 6.2. Figure 6.7 shows the results obtained with no load connected to the system. From this simulation, the values shown in Table 6.2 have been calculated. The change in the period of the mechanical excitation causes that less electrical energy is generated by the

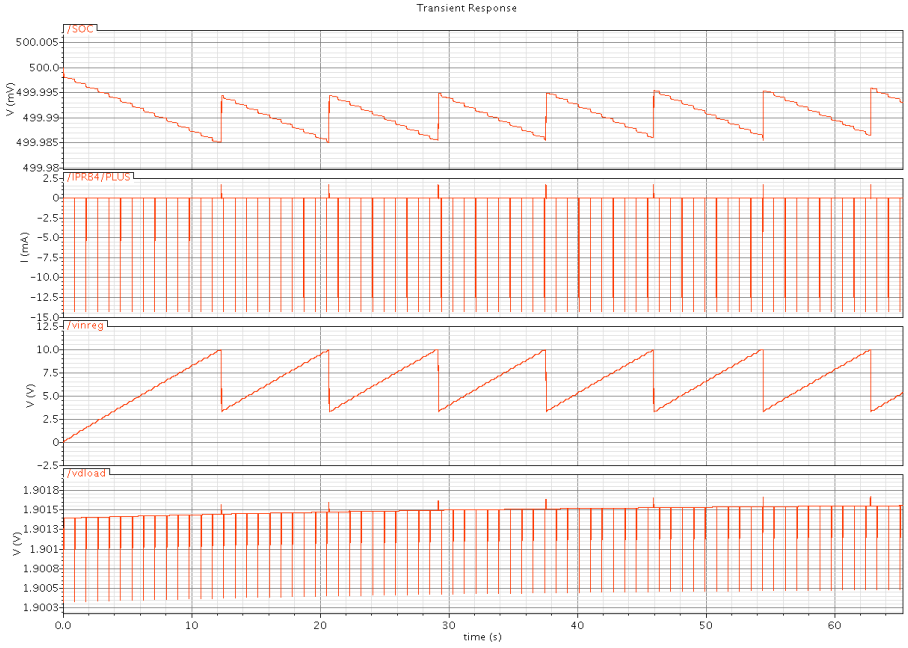

Figure 6.6: Zoom view of the simulation results with load for the parameters summarized in Table 6.1.

transducer and therefore stored in the battery despite the fact of incrementing the number of piezoelectric films from 10 to 20. Figure 6.8 shows the results for the simulation with the Enocean transmitter connected and a time between transmissions of 1.45 s.

Table 6.2: Results obtained from the simulation.

Parameter	Value
ρ_s	11.39 μW
τ	1.45 s
σ_3	8.1 μJ
σ_4	8.1 μJ
σ_1	133.64 μJ
σ_2	178.26 μJ
B_{min}	328.1 μJ
B_{0min}	186.36 μJ

In the two previous simulations, the values obtained for the capacity and initial charge of the battery are small since the mechanical excitation of the energy harvesting transducer is done periodically. Next simulation shows a

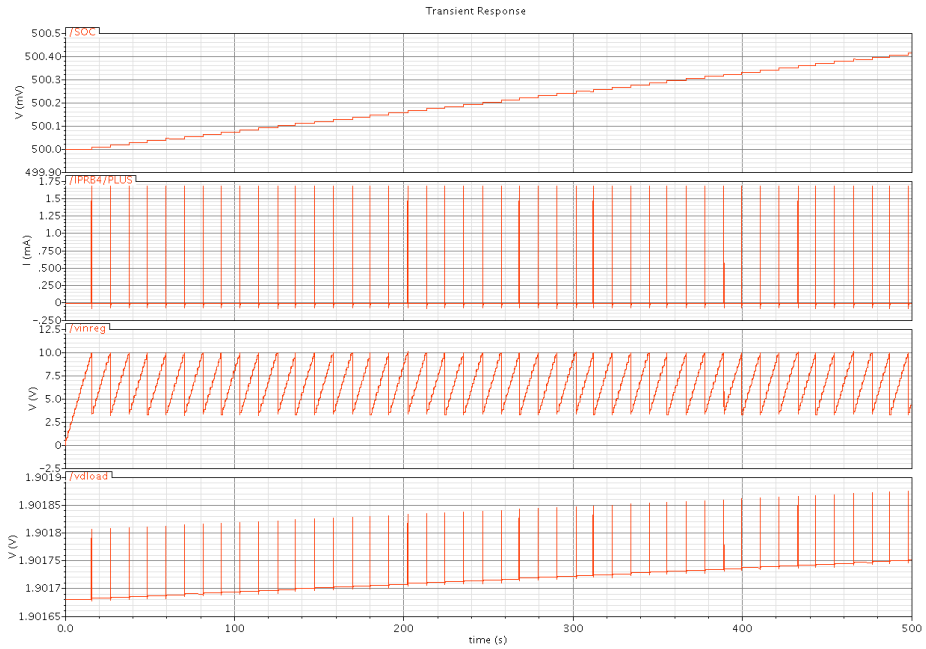

Figure 6.7: Simulation results without charge for n=20, T=1.2 s and the rest of parameters summarized in Table 6.1. The waveform called *SOC* shows the state of charge of the battery with a voltage range from 0 to 1 V. $IRPB4$ is the current flowing into the battery, *vinreg* is the voltage at the input of the linear regulator and *vdload* is the voltage of the battery that is supplied to the RF transmitter.

different scenario where the energy harvesting transducer is not excited periodically. Therefore, there is not mechanical excitation over the transducer between 0 and 100 s and also between 450 s and 500 s. Moreover, there are three different mechanical excitations connected through an adder to the piezoelectric transducer to create a non-periodic mechanical excitation as can be seen in the schematic simulated, Figure 6.9. Each one of these three different mechanical excitations has values of rise time, t_{r1}, t_{r2}, t_{r3} and fall time, t_{f1}, t_{f2} and t_{f3}. The value selected for the rise and fall time of the mechanical excitations is the same while the period of the three mechanical excitations is related since $T_2 = 2T_1$ and $T_3 = 3T_1$. The input and output of the block called piezofilm are shown in Figure 6.10. The first waveform corresponds to the voltage at the output of the piezoelectric elements connected in parallel and the second waveform is the mechanical excitation applied to the piezoelectric films.

The parameters employed during the simulation are shown in Table 6.3 and the simulation waveforms obtained without electrical load are displayed in Figure 6.11. The results obtained from the simulation are summarized in Table 6.4.

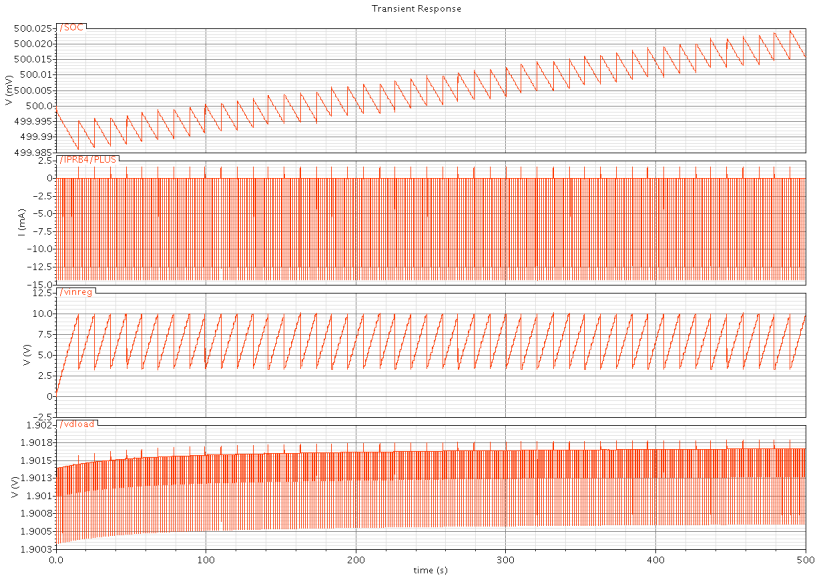

Figure 6.8: Simulation results with charge for n=20, T=1.2 s and the rest of parameters summarized in Table 6.1. The waveform called *SOC* shows the state of charge of the battery in per one, $IRPB4$ is the current flowing into the battery, *vinreg* is the voltage at the input of the linear regulator and *vdload* is the voltage of the battery that is supplied to the Enocean transmitter.

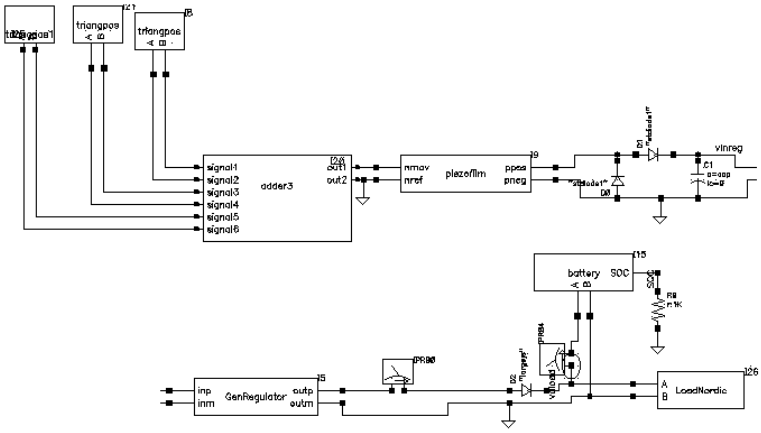

Figure 6.9: Schematic of a battery-powered RF transmitter simulated with the parameters of Table 6.3.

Table 6.3: Parameters employed for the simulation.

Parameter	Value
SOC_i	500 mV
W_0	30 mm
t_s	1 mm
n	10
L	30 mm
$vreg$	3.2 V
$vlimsup$	10 V
$vliminf$	vreg+0.1 V
$R_{int-reg}$	5 Ω
T_1	400 ms
T_2	$2T_1$
T_3	$3T_1$
t_{r1}	350 ms
t_{r2}	350 ms
t_{r3}	350 ms
t_{f1}	125 ms
t_{f2}	125 ms
t_{f3}	125 ms
$iconsreg$	10μA
$cintreg$	10μF
cap	10μF
$amplm_1$	6 mm
$amplm_2$	1 mm
$amplm_3$	1 mm
C_{BAT}	300 nAh

The mean power generated is in the same order of magnitude than in the two previous simulations as well as σ_3, σ_4 and the period between transmissions. Nevertheless, the values for B_{0min} and B_{min} have increased one order of magnitude since there is no mechanical excitation during all the simulating time. Thus, the simulation with the RF transmitter connected would allow to probe the validity of Equation 6.51 and Equation 6.50. The RF transmitter block described in Verilog-A employs a resistor of 132 Ω and a resistor of 633 kΩ to simulate the power consumed when the transmitter is sending data and in sleeping mode, respectively. Therefore, the power consumed by this load depends on the voltage supplied by the battery and this voltage also depends on the state of charge of the battery. Thus, it has been supposed a battery voltage of 2.05 V for calculating the period between transmissions.

The values for the minimum capacity of the battery and its minimum initial state of charge are calculated from the values obtained for B_{min} and B_{0min} in Table 6.4 and the values obtained are C_{BATmin}=203 nAh and SOC_imin=0.9. Figure 6.12 shows the simulation results employing those values. The results

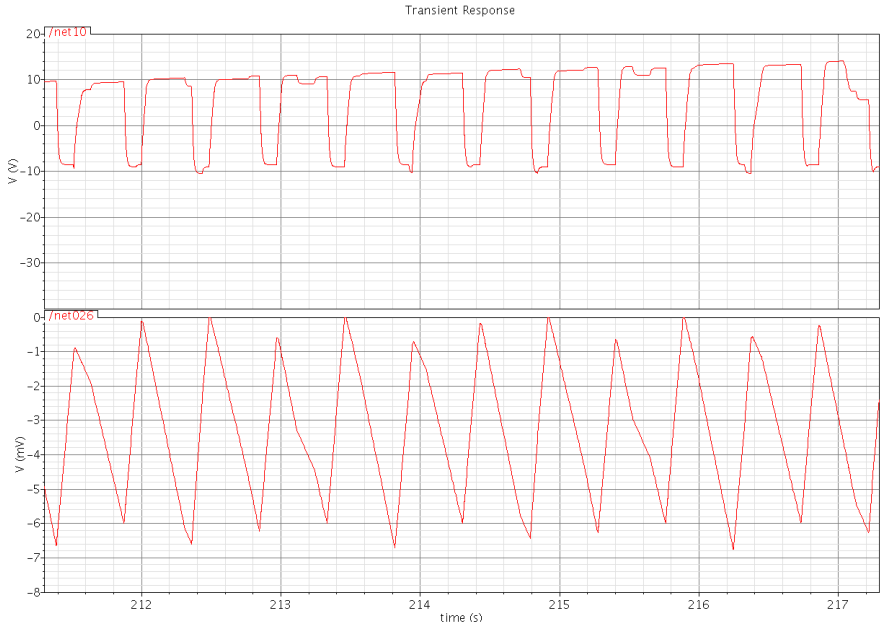

Figure 6.10: Total mechanical excitation combined from three different mechanical excitations.

obtained show that the RF transceiver stops to transmit at 100 s since the voltage on the battery is lower than 1.9 V that is the minimum supply voltage of the transceiver. At this moment the state of charge of the battery is 6.3%, the minimum obtained during the simulation. Afterwards the battery is charged a 101% from this minimum state of charge to its maximum state of charge (107.84%) and then decreases again due to the fact that there is no mechanical excitation from 450 s until the end of the simulation. However, the state of charge at the end of the simulation is not the same as at the beginning, what is considered energy neutral operation, due to the fact that the mean voltage of the battery during the simulation is greater than that employed for calculating the time between transmissions.

Figure 6.12 shows the simulation results obtained with C_{BAT}=1 μAh and SOC_i=0.3. The capacity chosen for the battery is bigger than the 203 nAh obtained as a minimum value and its initial state of charge is also bigger than the minimum initial charge of 182nAh calculated. In this case, the RF transmitter is supplied during all the simulation and the minimum state of charge of the battery 12.7%. The maximum state of charge obtained is of 35.4% at t=450 s and decreases to 0.29% at t=500 s since there is no mechanical excitation in this time interval. In this case the initial state of charge and the final state of charge are almost equal since the mean value of the battery voltage during the

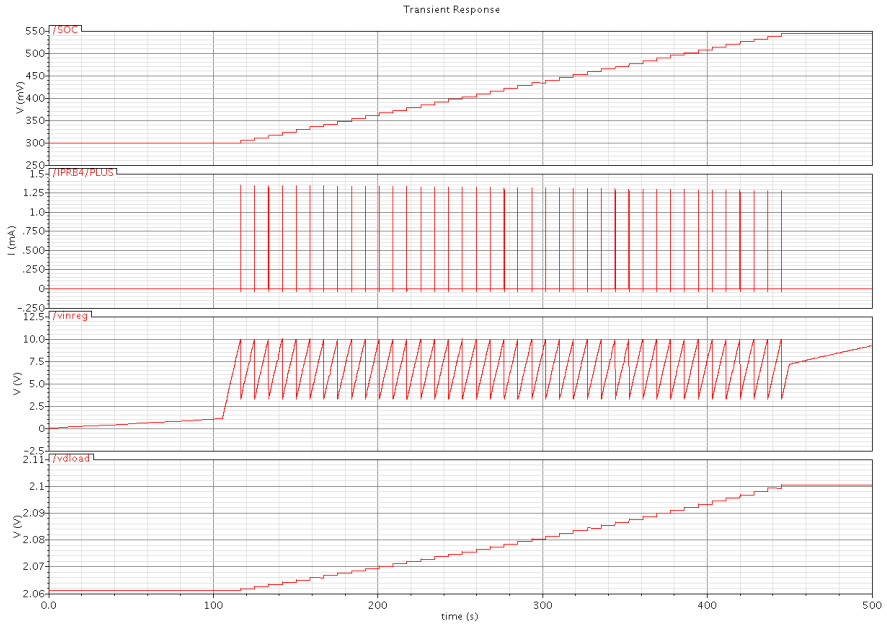

Figure 6.11: Simulation results without load for the parameters summarized in Table 6.3. The waveform called SOC shows the state of charge of the battery in per one. $IRPB4$ is the current flowing into the battery. *vinreg* is the voltage at the input of the linear regulator and *vdload* is the voltage of the battery that is supplied to the RF transmitter.

simulation is practically the same that the employed for the calculation of the time between RF transmissions. The voltage on the battery is quite constant since the state of charge of the battery is also almost constant since the capacity of the battery in this simulation is five times the minimum capacity calculated. Then, the system works in energy neutral operation.

Table 6.4: Results obtained from the simulation.

Parameter	Value
ρ_s	10.96 μW
τ	2.02 s
σ_3	8.1 μJ
σ_4	8.1 μJ
σ_1	138.06 μJ
σ_2	1.3 mJ
B_{min}	1.46 mJ
B_{0min}	1.31 mJ

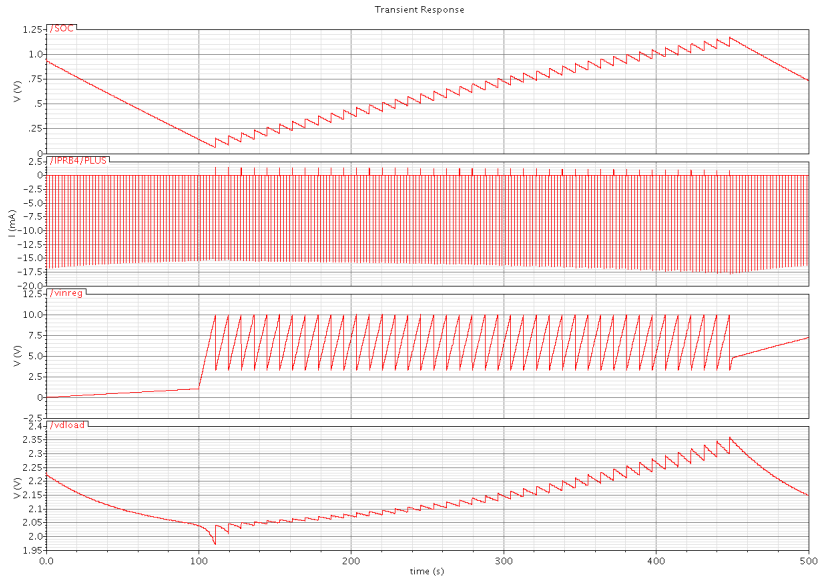

Figure 6.12: Simulation results with the Enocean transmitter as a load for the parameters summarized in Table 6.3. The waveform called *SOC* shows the state of charge of the battery in per one, $IRPB4$ is the current flowing into the battery, *vinreg* is the voltage at the input of the linear regulator and *vdload* is the voltage of the battery that is supplied to the RF transmitter.

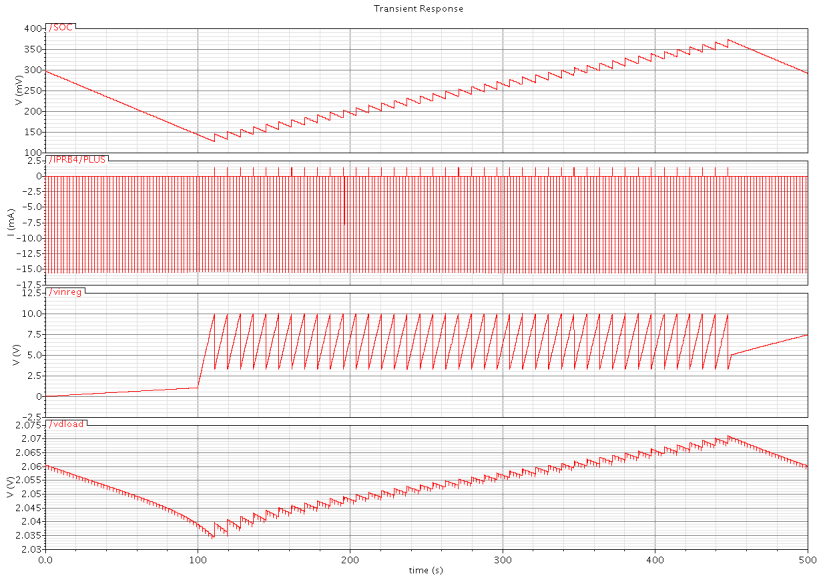

Figure 6.13: Simulation results with the Enocean transmitter as a load for the parameters summarized in Table 6.3. The waveform called *SOC* shows the state of charge of the battery in per one, $IRPB4$ is the current flowing into the battery, *vinreg* is the voltage at the input of the linear regulator and *vdload* is the voltage of the battery that is supplied to the Enocean transmitter.

Chapter 7

Conclusions

This chapter gives the general conclusions of the thesis whereas each paper included in Part II has its specific conclusions for the addressed problem. There are several general remarks to do for the design of an energy harvesting power supply from human power.

It is important to distinguish between energy harvesting from human body and from the environment. Both cases can use the same transducers and input energies. Nevertheless, the design of the transducer, the power management unit or the electronic load to power is different since the energy input levels in both cases as well as the amplitude and frequency of the signals of mechanical vibrations are not comparable. Normally, the energy levels associated to human body are lower than the energy levels associated to environmental sources which gives as a result that sophisticated techniques must be used to increase the efficiency of the transducer, to control the power management unit and to power the load.

An energy harvesting power supply has to be considered as a complete system where each element must be adapted to accomplish the requirements of the load. A system-level simulation is of special interest because it allows to simulate the mechanical and electrical elements together. This is a great advantage in order to increase the efficiency of both elements in the same simulation environment. Moreover, it is useful to decide the energy profile of the load (continuous or discontinuous operation) and the use of an energy storage element. Furthermore, with a system-level simulation, a trade off between the requirements of the load and the dimensions of the transducer can be easily made.

An application example for energy harvesting systems is to sense and transmit data. Therefore, a communication module with a microprocessor and a transceiver can be considered as a standard load for an energy harvesting system. Taking into account today's energy consumption requirements of low power transmission modules and the amount of energy that is harvested from human body, the most usual scenario is the discontinuous operation of the load. The inclusion of an energy storage element like a lithium ion battery, a capacitor or a supercapacitor must be evaluated taking into account different scenarios and

parameters. It must be considered if the load must operate continuously, the different power consumption modes of the load, the minimum operation time that needs each power consumption mode, the maximum time between transmissions, the amount of energy that can be stored in the energy storage element and the size, weight and volume that adds this element to the complete system.

A system-level simulation is ideal to make this kind of decisions since the modeling of the system elements can be done as in [13] with the physical equations of the transducer in order to include the mechanical part of the system and electrical or behavioral models for the rest of the components. In this way, it is simple for example to evaluate different transmission modules only taking into account their voltage supply and power consumption.

Once a general conclusion from the system point of view is made, specific conclusions for each element that is present in an energy harvesting power supply are given. The type of input energy and transducer form a tandem since the election of one imposes the other. The input energy must be measured or modeled in order to include it as the input variable of the system. In the case of TEGs the input energy can be modeled without the help of a previous measurement, only taking into account that the skin temperature is not constant over the body. However, for kinetic energies it is necessary to measure them in order to incorporate this data to a simulation environment or to model them. These measurements allow to include real inputs to the system and therefore to obtain realistic results and predictions. It is important that measurements are done in different parts of the human body doing different physical activities to locate which positions and activities produce more energy. However, some applications force the location of the energy transducer to a specific part of the human body close to the wearable device to supply.

There are several ways to model a transducer. One way consists in the use of the physical equations of the transducer like in [13] (Chapter 13) where the physical equations of a piezoelectric transducer were included directly in the model. A second method is to employ a circuit model that includes the conversion of the available energy into electrical energy as was shown in Chapter 3 where an electrical circuit that contains mechanical and electrical parts is given as well as in Chapter 5 where thermal and electrical parts are combined. The third proposed model presented contains only the electrical part of the complete model like in [20] (Chapter 10). The two first methods allow to improve the coupling between the energy source and the transducer modifying the physical parameters of the transducer. However, the third method only takes into account the electrical response of the transducer without the possibility of rearranging its physical design. Therefore, the two first approaches are indicated when the the coupling between body and transducer wants to be explored and improved whereas the last one is a simplified model that can be employed as the electrical voltage supply for the power management unit.

For all the cases, it is necessary to take into account the location of the energy harvesting transducer that usually depends strongly on the application. Measurements done with the energy harvesting transducer in the selected location are of special importance to adjust and validate the models for the transducers

since each location even with the same transducer generates different voltage and current waveforms. For the third way under consideration to model an energy harvesting transducer, the measurements are the only possibility to adjust the electrical source of the model.

7.1 Smart Clothes and Energy Harvesting

Nowadays, there is not yet available a real integration of wearable devices in clothes and it is only possible to attach external portable devices to clothes. Clothes and shoes are in direct contact with body skin. Thus, it is desirable that textiles and clothes are involved in different ways in the human body energy harvesting system:

- Developing comfortable connection technologies to integrate the transducers into fabrics. Furthermore, also the fabrics can be developed to act as an energy human transducers themselves (energy-harvesting fabrics).
- Developing conductive properties to create electronic circuits that connect the different components of the energy harvesting system (the energy harvesting transducers, the power management unit and the electric load).

This gives as a result a step further in the textile sector: e-textiles and smartclohtes. The improvement in these technologies and their merge with energy harvesting supplies employing human energy would be an improvement factor in this field based in the fact that the integration of the transducer in smartclothes or e-textiles would increase the surface of the transducer and its mechanical coupling with human body and therefore, more electrical energy would be generated. The mechanical coupling between the transducer and the human body depends on the location of the transducer and the activity that is done. A specific design taking this into account can increase very much the efficiency of the transducer as has been demonstrated in [19, 21] (Chapter 3 and Chapter 4).

7.2 Power Management Unit

The transducer is the element that converts the available human body energy into electrical energy. The combination of transducer and human body location gives as a result different output voltage and current levels generated by the transducer. These levels condition the power management unit design. Low output voltage levels obtained by TEGs and inductive transducers are no longer an issue for the design of power management units with the new technologies in the field of CMOS transistors that have low gate threshold voltages like ALD110800 with a gate threshold voltage of 0 V, ALD110802 [125] with a gate threshold voltage of 0.2 V or BSH105 [126] with a higher threshold voltage (0.57 V) but a lower drain source resistor than the other ones when a discrete

design is required. Another already known solution can be the employment of N-channel FETs which are self-conducting with a zero gate voltage [119]. The next step is the integration of the power conditioning circuits on the same chip to be powered. Several CMOS and BiCMOS technologies would be suitable for this purpose. More advances in the field of power management circuits would improve a lot the possibilities and simplify the designs of energy harvesting power supplies employing human body as input energy source.

There are two important factors to take into account in the design of the power management unit. The first one is related with the design of a starter circuit for the main power converter. A starter circuit initially stores enough voltage and/or current level to start switching the transistors of the main power management circuit [119]. A starter circuit must be included when it can not be assured that there will be enough energy for starting the operation of the main DC-DC converter circuit. The second one is related with the efficiency of the power management circuits. As important as increasing the efficiency of the power management circuit itself is developing techniques that ensure that the energy extracted from the transducer is the maximum available. For the case of piezoelectric transducers, it was calculated the optimum value of the capacitor for defined load conditions. For other transducers like the TEGs, the maximum power point tracking method can be applied, if the design of a low power consumption control loop can be achieved [127, 128].

Energy harvesting power supplies are able to supply power to present-day low power electronic devices as was demonstrated for example with the application presented in [22, 118]. Obviously, the load must be a low power consumption device and it is preferable to operate in a discontinuous way without a battery. This conclusion is based on the simulation results obtained in [13] (Chapter 13). This method is also employed to supply the RF communication module connected to the TEG in [22, 118] (Chapter 12). However, the evolution in low power transmission modules can change this conclusion depending mostly on the evolution of the power consumption in stand-by mode and the configuration time in transmission operation.

For the case of an energy harvesting power supply from human body it is not required to make use of a conventional battery charger (that includes a current-limit, a voltage-limit regulation loop and a time-limited charge termination circuit) and thus energy and area can be saved. A current-limit regulation loop is usually required to avoid overcharging during the fast charging stage of NiMH and lithium batteries [94] that is not required in our case due to the the intrinsic current limiting characteristics of the TEG, piezoelectric films and inductive generators. Additionally, the voltage-limit regulation loop is undertaken by the power management unit that has to adapt the output voltage level of the transducer to the requirements of the load. Time-limited charge termination circuitry is also avoided by selecting a regulated voltage slightly below the maximum topping voltage specified by battery manufacturers. Hence, for this case, a battery charger is replaced by a diode or a transistor connected between the output of the regulator and the battery to avoid the supply of the converter with the battery. This approach is more advisable for lithium-polymer than

for Ni-MH accumulators, since the latter suffer from memory effect degradation when the charging procedure is not completed [118]. This topology can be enhanced in terms of reliability by placing a Zener diode that limits the charging voltage in case of failure.

7.3 Energy and Power requirements of Applications

It is better to do the quantification of energy harvesting power supplies in terms of energy than power since it is a more meaningful magnitude when dealing with the discontinuous events of the load and the source of the system. The design of the electronic load to power with the energy harvesting power supply is not an objective of the thesis. Nevertheless, considering a communication module as the load, some conclusions and suggestions can be given. An important factor related with the energy consumption of the load is the communication protocol employed by its transceiver.

The particular needs of the application must be evaluated before assuming the employment of a de-facto standard communication protocol like for example ZigBee. The communication protocols can be compared in terms of radio efficiency (defined as the ratio between the payload and the gross data rate) and in terms of Time on Air (defined as the duration of the data transmission) [118]. In [118] a comparison between the Nordic proprietary solution and ZigBee was made in these terms and it was concluded that the Nordic protocol was the best one for the particular needs exposed (less than 200 bits of payload).

It is also interesting to notice that the energy consumption of the microprocessor (that form part of the communication module) can be reduced applying changes in its code. It was demonstrated in [129] that a code optimization of the operating system employed by wireless sensor networks reduce their energy consumption.

Part III

Appendixes

Appendix A

Relations between Piezoelectric Constants

The relations between the different piezoelectric constants, summarized in Table 3.2 of Section 3.1, are deduced from the comparison of the four different ways to express the piezoelectric constitutive equations.

$$\begin{aligned} D_l &= \varepsilon_{lm}^{T} E_m + d_{li} T_i \\ E_m &= -g_{mi} T_i + \beta_{ml}^{T} D_l \end{aligned} \qquad \text{for } i,j,k = 1,\ldots,6 \text{ and } l,m,n = 1,2,3 \tag{A.1}$$

$$\left[\boldsymbol{\varepsilon^T}\right] = \left[\boldsymbol{\beta^T}\right]^{-1} \tag{A.2}$$

$$[\mathbf{d}] = \left[\boldsymbol{\beta}^{T}\right]^{-1} [\mathbf{g}] = \left[\boldsymbol{\varepsilon}^{T}\right] [\mathbf{g}] \tag{A.3}$$

If these equations are compared, it is found a relation between their piezoelectric constants ($\left[\mathbf{s}^{D}\right]$, $\left[\mathbf{c}^{D}\right]$, $[\mathbf{g}]$ and $[\mathbf{h}]$).

$$\begin{aligned} S_i &= s_{ij}^{D} T_j + g_{li} D_l \\ T_j &= c_{ji}^{D} S_i - h_{lj} D_l \end{aligned} \qquad \text{for } i,j,k = 1,\ldots,6 \text{ and } l,m,n = 1,2,3 \tag{A.4}$$

$$\left[\mathbf{s}^{D}\right] = \left[\mathbf{c}^{D}\right]^{-1} \tag{A.5}$$

$$[\mathbf{g}] = \left[\mathbf{c}^{D}\right]^{-1} [\mathbf{h}] = \left[\mathbf{s}^{D}\right] [\mathbf{h}] \tag{A.6}$$

If the following equations are compared, it is found a relation between their piezoelectric constants.

$$\begin{aligned} E_l &= -h_{li} S_i + \beta_{lm}^{S} D_m \\ D_m &= e_{mi} S_i + \varepsilon_{ml}^{S} E_l \end{aligned} \qquad \text{for } i,j,k = 1,\ldots,6 \text{ and } l,m,n = 1,2,3 \tag{A.7}$$

$$\left[\boldsymbol{\varepsilon}^S\right] = \left[\boldsymbol{\beta}^S\right]^{-1} \tag{A.8}$$

$$[\mathbf{e}] = \left[\boldsymbol{\beta}^S\right]^{-1}[\mathbf{h}] = \left[\boldsymbol{\varepsilon}^S\right][\mathbf{h}] \tag{A.9}$$

The relation between $\left[\mathbf{s}^E\right]$ and $\left[\mathbf{s}^D\right]$ is more difficult to find than the previous ones. The method to obtain the expression that relates both piezoelectric constants is detailed in the following lines. First of all, the two piezoelectric expressions S(T,E) and S(T,D) are equaled.

$$s_{ij}^E T_j + d_{il} E_l = s_{ij}^D T_j + g_{im} D_m \quad \text{for } i,j,k = 1,\ldots,6 \text{ and } l,m,n = 1,2,3 \tag{A.10}$$

If $[D_m]$ is sbstituted, this new expression is obtained,

$$s_{ij}^E T_j + d_{il} E_l = s_{ij}^D T_j + g_{im}\left(\varepsilon_{ml}^T E_l + d_{mj} T_j\right) \quad \text{for } i,j,k = 1,\ldots,6 \text{ and } l,m,n = 1,2,3 \tag{A.11}$$

Substituting g_{im} for the expression obtained in Equation A.3

$$\begin{array}{l} s_{ij}^E T_j + d_{il} E_l = s_{ij}^D T_j + d_{il}\left(\varepsilon_{ml}^T\right)^{-1}\left(\varepsilon_{ml}^T E_l + d_{mj} T_j\right) \\ \text{for } i,j,k = 1,\ldots,6 \text{ and } l,m,n = 1,2,3 \end{array} \tag{A.12}$$

This equation can be simplified to obtain:

$$\left[\mathbf{s}^D\right] = \left[\mathbf{s}^E\right] - [\mathbf{d}]\left[\boldsymbol{\varepsilon}^T\right]^{-1}[\mathbf{d}] \tag{A.13}$$

From the existing relation between [**s**] and [**c**]. It can be deduced the following relation between [**c**] and $\left[\mathbf{c}^E\right]$,

$$\left[\mathbf{c}^D\right]^{-1} = \left[\mathbf{c}^E\right]^{-1} - [\mathbf{d}]\left[\boldsymbol{\varepsilon}^T\right]^{-1}[\mathbf{d}] \tag{A.14}$$

In a similar way the relation between $\left[\boldsymbol{\varepsilon}^{\boldsymbol{S}}\right]$ and $\left[\boldsymbol{\varepsilon}^{\boldsymbol{T}}\right]$ is deduced. First of all, the two piezoelectric expressions D(S,E) and D(E,T) are equaled.

$$\begin{array}{l} e_{li} S_i + \varepsilon_{lm}^S E_m = \varepsilon_{lm}^T E_m + d_{lj} T_j \\ \text{for } i,j,k = 1,\ldots,6 \text{ and } l,m,n = 1,2,3 \end{array} \tag{A.15}$$

If T_j is substituted, this new expression is obtained,

$$\begin{array}{l} e_{li} S_i + \varepsilon_{lm}^S E_m = \varepsilon_{lm}^T E_m + d_{lj}\left(c_{ji}^E S_i - e_{jm} E_m\right) \\ \text{for } i,j,k = 1,\ldots,6 \text{ and } l,m,n = 1,2,3 \end{array} \tag{A.16}$$

Substituting d_{lj} by $e_{lj}\left(\left(c_{ji}^E\right)^{-1}\right)^t$ and e_{jm} by $\left(s_{ij}^E\right)^{-1} d_{im}$. As c_{ji}^E is a symmetric matrix, it is obtained:

$$\left[\boldsymbol{\varepsilon}^S\right] = \left[\boldsymbol{\varepsilon}^T\right] - [\mathbf{d}]\left[\mathbf{s}^E\right]^{-1}[\mathbf{d}] \tag{A.17}$$

From the existing relation between $[\boldsymbol{\varepsilon}]$ and $[\boldsymbol{\beta}]$. It can be deduced the following relation between $\left[\mathbf{c}^D\right]$ and $\left[\mathbf{c}^E\right]$,

$$\left[\boldsymbol{\beta}^S\right]^{-1} = \left[\boldsymbol{\beta}^T\right]^{-1} - [\mathbf{d}]\left[\mathbf{s}^E\right]^{-1}[\mathbf{d}] \tag{A.18}$$

Appendix B

Relations between Piezoelectric Constants for PVDF and Ceramic Materials

The piezoelectric constitutive equations are general, without any consideration on the value of matrix elements. For real materials, the corresponding matrices present some properties that lead to simplified equations. The two most common types of piezoelectric materials are PVDF, polyvinylidene fluoride, and PZT, lead zirconate titanate that is a ceramic piezoelectric material. In this appendix, it is analyzed the relation of the piezoelectric constitutive equations and deduced which is the best mechanical excitation mode for these two materials.

B.1 Polyvinylidene Fluoride films

Polyvinylidene fluoride (PVDF) is a piezoelectric polymer with mm2 crystal symmetry [130]. Due to this fact the piezoelectric constitutive equations shown in equation 3.1 can be expressed in a matrix form as:

$$\begin{bmatrix} s_{11}^E & s_{12}^E & s_{13}^E & 0 & 0 & 0 & 0 & 0 & d_{31} \\ s_{12}^E & s_{22}^E & s_{23}^E & 0 & 0 & 0 & 0 & 0 & d_{32} \\ s_{13}^E & s_{23}^E & s_{33}^E & 0 & 0 & 0 & 0 & 0 & d_{33} \\ 0 & 0 & 0 & s_{44}^E & 0 & 0 & 0 & d_{24} & 0 \\ 0 & 0 & 0 & 0 & s_{55}^E & 0 & d_{15} & 0 & 0 \\ 0 & 0 & 0 & 0 & 0 & s_{66}^E & 0 & 0 & 0 \\ 0 & 0 & 0 & 0 & d_{15} & 0 & \varepsilon_{11}^T & 0 & 0 \\ 0 & 0 & 0 & d_{24} & 0 & 0 & 0 & \varepsilon_{22}^T & 0 \\ d_{31} & d_{32} & d_{33} & 0 & 0 & 0 & 0 & 0 & \varepsilon_{33}^T \end{bmatrix} \begin{bmatrix} T_1 \\ T_2 \\ T_3 \\ T_4 \\ T_5 \\ T_6 \\ E_1 \\ E_2 \\ E_3 \end{bmatrix} = \begin{bmatrix} S_1 \\ S_2 \\ S_3 \\ S_4 \\ S_5 \\ S_6 \\ D_1 \\ D_2 \\ D_3 \end{bmatrix} \quad \text{(B.1)}$$

A more compact way to express Equation B.1 is:

$$\begin{bmatrix} s_{11}^E & s_{12}^E & s_{13}^E & d_{31} \\ s_{12}^E & s_{22}^E & s_{23}^E & d_{32} \\ s_{13}^E & s_{23}^E & s_{33}^E & d_{33} \\ d_{31} & d_{32} & d_{33} & \varepsilon_{33}^T \end{bmatrix} \begin{bmatrix} T_1 \\ T_2 \\ T_3 \\ E_3 \end{bmatrix} = \begin{bmatrix} S_1 \\ S_2 \\ S_3 \\ D_3 \end{bmatrix} \tag{B.2}$$

$$\begin{bmatrix} s_{44}^E & d_{24} \\ d_{24} & \varepsilon_{22}^T \end{bmatrix} \begin{bmatrix} T_4 \\ E_2 \end{bmatrix} = \begin{bmatrix} S_4 \\ D_2 \end{bmatrix} \tag{B.3}$$

$$\begin{bmatrix} s_{55}^E & d_{15} \\ d_{15} & \varepsilon_{11}^T \end{bmatrix} \begin{bmatrix} T_5 \\ E_1 \end{bmatrix} = \begin{bmatrix} S_5 \\ D_1 \end{bmatrix} \tag{B.4}$$

$$s_{66}^E T_6 = S_6 \tag{B.5}$$

PVDF films are usually only metalized in the plane perpendicular to direction 3, so that $D_1 = D_2 = 0$. Equation (B.6) expresses the electric displacement generated in the piezoelectric element in charge mode (shortcircuit between the film connectors and therefore no electric field is applied).

$$D_3 = d_{31}T_1 + d_{32}T_2 + d_{33}T_3 \tag{B.6}$$

Equation (B.6) can be expressed in Einstein notation as:

$$D_3 = d_{3p}T_p \quad \text{for } p = 1, 2, 3 \tag{B.7}$$

The equivalent expression in voltage mode (open circuit between the film connectors and therefore no electric displacement is applied) can be obtained in a similar way from Equation (3.2):

$$\begin{bmatrix} s_{11}^D & s_{12}^D & s_{13}^D & 0 & 0 & 0 & 0 & 0 & g_{31} \\ s_{12}^D & s_{22}^D & s_{23}^D & 0 & 0 & 0 & 0 & 0 & g_{32} \\ s_{13}^D & s_{23}^D & s_{33}^D & 0 & 0 & 0 & 0 & 0 & g_{33} \\ 0 & 0 & 0 & s_{44}^D & 0 & 0 & 0 & g_{24} & 0 \\ 0 & 0 & 0 & 0 & s_{55}^D & 0 & g_{15} & 0 & 0 \\ 0 & 0 & 0 & 0 & 0 & s_{66}^D & 0 & 0 & 0 \\ 0 & 0 & 0 & 0 & -g_{15} & 0 & \beta_{11}^T & 0 & 0 \\ 0 & 0 & 0 & -g_{24} & 0 & 0 & 0 & \beta_{22}^T & 0 \\ -g_{31} & -g_{32} & -g_{33} & 0 & 0 & 0 & 0 & 0 & \beta_{33}^T \end{bmatrix} \begin{bmatrix} T_1 \\ T_2 \\ T_3 \\ T_4 \\ T_5 \\ T_6 \\ D_1 \\ D_2 \\ D_3 \end{bmatrix} =$$

$$= \begin{bmatrix} S_1 \\ S_2 \\ S_3 \\ S_4 \\ S_5 \\ S_6 \\ E_1 \\ E_2 \\ E_3 \end{bmatrix} \tag{B.8}$$

The voltage mode equation with Einstein notation is:

$$V_3 = g_{3p} T_p t_c \quad \text{for } p = 1, 2, 3 \tag{B.9}$$

where t_c is the thickness of the piezoelectric material.

This expression shows that only the longitudinal directions and not the shear directions (4, 5 and 6) take part in the generated voltage. Therefore, there are three possible modes to use the PVDF films: 31, 32, and 33. Figure B.1 shows a piezoelectric PVDF film positioned in its correspondent Cartesian coordinate system. The length of the rod, L, is oriented along axis 1, the width, W, along axis 2 and the thickness, t_c, along axis 3 [104].

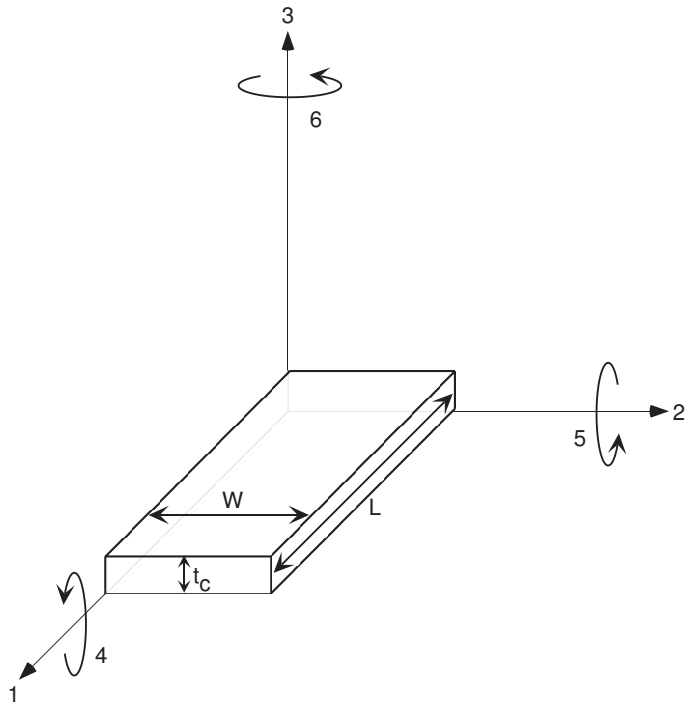

Figure B.1: Mechanical axis position for piezoelectric materials.

Mode 31 corresponds to a mechanical excitation along axis 1 whereas the electrical answer is obtained in the plane perpendicular to axis 3 as can be shown in Figure B.2. In this figure it is observed a mechanical force, F_1, applied along axis 1 that causes a strain of the piezoelectric film in the same direction. The mechanical stress generates a voltage in the piezoelectric element in the plane perpendicular to axis 3 since it is open circuited. In the case of a piezoelectric element shortcircuited, it would be obtained an electrical current instead of a voltage. Figure B.3 illustrates the case of working mode 33. In this case,

the mechanical excitation is applied along axis 3 which causes a strain of the material in the same direction. The electrical answer is obtained, as in the previous case, in the plane perpendicular to axis 3.

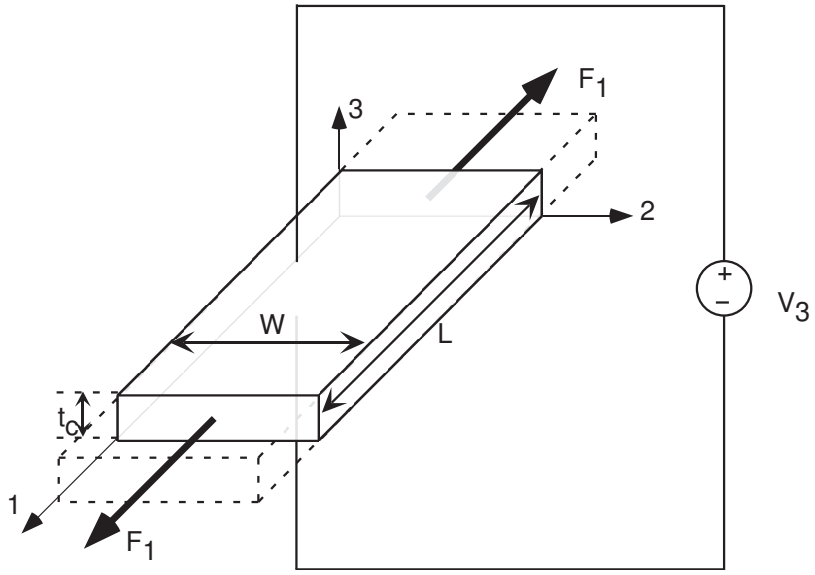

Figure B.2: Mechanical excitation of the piezoelectric film along axis 1.

Mode 32 is discarded since d_{32} is 10 times less than d_{31} or d_{33} (Brown, 2002). In mode 31, the stress is applied in direction 1, and in mode 33, the stress is applied in direction 3. The voltage and charge obtained resulting from an applied force in a certain direction, F_1 or F_3, are shown in Table B.1.

Table B.1: Voltage, V_3, and charge, q_3, obtained in the plane perpendicular to direction 3 applying a mechanical stress in direction 1, mode 31, and in direction 3, mode 33.

	Mode 31	Mode 33
V_3	$g_{31}\frac{F_1}{W}$	$g_{33}\frac{F_3}{WL}t_c$
q_3	$d_{31}\frac{F_1 L}{t_c}$	$d_{33}F_3$

In a thin PVDF film, the ratio L/t_c is on the order of 1000, while $d_{31} = 23E - 12$ m/V and $d_{33} = -33E - 12$ m/V [104]. Assuming that $F_1 = F_3$, then V_3 and q_3 for the mode 31 will be on the order of 700 times greater than V_3 and q_3 for the mode 33. Therefore, for the same mechanical energy input, more electrical energy output is obtained in mode 31 than in mode 33 when the PVDF piezoelectric films are employed. For other piezoelectric materials, mode 33 excitation can be a better solution than mode 31 if the length, width, and

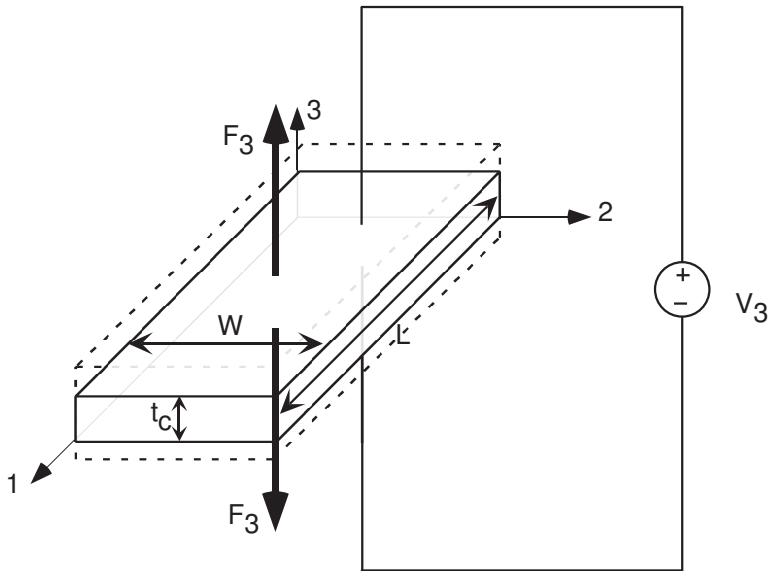

Figure B.3: Mechanical excitation of the piezoelectric film along axis 3.

thickness of the piezoelectric material are similar.

The relations between the piezoelectric constants for the case of the PVDF films in working modes 31 and 33 are given in the next subsections.

B.1.1 Piezoelectrical constants for PVDF in mode 31

The mechanical conditions that requires to operate in mode 31 are that $T_2 = T_3 = 0$ and $S_2 = S_3 = 0$. Therefore, only a mechanical stress is applied in direction 1 (T_1) and the working mode is called length expansion. The four ways employed to express the piezoelectric effect for this particular situation are:

$$\begin{aligned} S_1 &= s_{11}^E T_1 + d_{31} E_3 \\ D_3 &= d_{31} T_1 + \varepsilon_{33}^T E_3 \end{aligned} \tag{B.10}$$

$$\begin{aligned} S_1 &= s_{11}^D T_1 + g_{31} D_3 \\ E_3 &= -g_{31} T_1 + \tfrac{1}{\varepsilon_{33}^T} D_3 \end{aligned} \tag{B.11}$$

$$\begin{aligned} T_1 &= c_{11}^D S_1 - h_{31} D_3 \\ E_3 &= -h_{31} S_1 + \tfrac{1}{\varepsilon_{33}^S} D_3 \end{aligned} \tag{B.12}$$

$$\begin{aligned} T_1 &= c_{11}^E S_1 - e_{31} E_3 \\ D_3 &= e_{31} S_1 + \varepsilon_{33}^S E_3 \end{aligned} \tag{B.13}$$

The relations extracted from the piezoelectric constitutive equations between the piezoelectric constants are summarized in Table 3.3 of Section 3.1.

Table B.2: Relation between piezoelectric constants for PVDF in mode 33.

Relation between piezoelectric constants
$d_{33} = g_{33}\varepsilon_{33}^{T}$
$s_{33}^{E} = \frac{1}{c_{33}^{E}}$
$d_{33} = \frac{e_{33}}{c_{33}^{E}} = e_{33}s_{33}^{E}$
$s_{33}^{D} = \frac{1}{c_{33}^{D}}$
$g_{33} = \frac{h_{33}}{c_{33}^{D}} = h_{33}s_{33}^{D}$
$e_{33} = h_{33}\varepsilon_{33}^{S}$
$\varepsilon_{33}^{S} = \varepsilon_{33}^{T}\left(1 - \frac{d_{33}^{2}}{s_{33}^{E}\varepsilon_{33}^{T}}\right) = \varepsilon_{33}^{T}\left(1 - k_{33}^{2}\right)$
$s_{33}^{D} = s_{33}^{E}\left(1 - \frac{d_{33}^{2}}{s_{33}^{E}\varepsilon_{33}^{T}}\right) = s_{33}^{E}\left(1 - k_{33}^{2}\right)$

B.1.2 Piezoelectrical constants for PVDF in mode 33

The mechanical conditions that requires to operate in mode 33 are that $T_1 = T_2 = 0$ and $S_1 = S_2 = 0$. Therefore, only a mechanical stress is applied in direction 3 (T_3) and the working mode is called thickness expansion. The piezoelectric equations for this particular situation are:

$$\begin{aligned} S_3 &= s_{33}^{E}T_3 + d_{33}E_3 \\ D_3 &= d_{33}T_3 + \varepsilon_{33}^{T}E_3 \end{aligned} \tag{B.14}$$

$$\begin{aligned} S_3 &= s_{33}^{D}T_3 + g_{33}D_3 \\ E_3 &= -g_{33}T_3 + \tfrac{1}{\varepsilon_{33}^{T}}D_3 \end{aligned} \tag{B.15}$$

$$\begin{aligned} T_3 &= c_{33}^{D}S_3 - h_{33}D_3 \\ E_3 &= -h_{33}S_3 + \tfrac{1}{\varepsilon_{33}^{S}}D_3 \end{aligned} \tag{B.16}$$

$$\begin{aligned} T_3 &= c_{33}^{E}S_3 - e_{33}E_3 \\ D_3 &= e_{33}S_3 + \varepsilon_{33}^{S}E_3 \end{aligned} \tag{B.17}$$

The relations extracted from the piezoelectric constitutive equations between the piezoelectric constants in mode 33 are summarized in Table B.2. k_{33} is the piezoelectric coupling constant for working mode 33.

B.2 Ceramic Material

In this section the analysis is limited to poled polycrystalline ceramics which have ∞mm symmetry that is equivalent to 6mm in the hexagonal symmetry system [131]. The representation of Equation 3.1 in a matrix form and its comparison with Equation B.1 motivates that the analysis of these materials can be done as a sub case of the case of polyvinylidene fluoride films.

$$\begin{bmatrix} s_{11}^D & s_{12}^D & s_{13}^D & 0 & 0 & 0 & 0 & 0 & g_{31} \\ s_{12}^D & s_{11}^D & s_{23}^D & 0 & 0 & 0 & 0 & 0 & g_{31} \\ s_{13}^D & s_{23}^D & s_{33}^D & 0 & 0 & 0 & 0 & 0 & g_{33} \\ 0 & 0 & 0 & s_{44}^D & 0 & 0 & 0 & g_{24} & 0 \\ 0 & 0 & 0 & 0 & s_{44}^D & 0 & g_{24} & 0 & 0 \\ 0 & 0 & 0 & 0 & 0 & s_{66}^D & 0 & 0 & 0 \\ 0 & 0 & 0 & 0 & -g_{24} & 0 & \beta_{11}^T & 0 & 0 \\ 0 & 0 & 0 & -g_{24} & 0 & 0 & 0 & \beta_{11}^T & 0 \\ -g_{31} & -g_{31} & -g_{33} & 0 & 0 & 0 & 0 & 0 & \beta_{33}^T \end{bmatrix} \begin{bmatrix} T_1 \\ T_2 \\ T_3 \\ T_4 \\ T_5 \\ T_6 \\ D_1 \\ D_2 \\ D_3 \end{bmatrix} =$$

$$= \begin{bmatrix} S_1 \\ S_2 \\ S_3 \\ S_4 \\ S_5 \\ S_6 \\ E_1 \\ E_2 \\ E_3 \end{bmatrix} \tag{B.18}$$

$$\begin{bmatrix} s_{11}^E & s_{12}^E & s_{13}^E & 0 & 0 & 0 & 0 & 0 & d_{31} \\ s_{12}^E & s_{11}^E & s_{23}^E & 0 & 0 & 0 & 0 & 0 & d_{31} \\ s_{13}^E & s_{23}^E & s_{33}^E & 0 & 0 & 0 & 0 & 0 & d_{33} \\ 0 & 0 & 0 & s_{44}^E & 0 & 0 & 0 & d_{15} & 0 \\ 0 & 0 & 0 & 0 & s_{44}^E & 0 & d_{15} & 0 & 0 \\ 0 & 0 & 0 & 0 & 0 & s_{66}^E & 0 & 0 & 0 \\ 0 & 0 & 0 & 0 & d_{15} & 0 & \varepsilon_{11}^T & 0 & 0 \\ 0 & 0 & 0 & d_{15} & 0 & 0 & 0 & \varepsilon_{11}^T & 0 \\ d_{31} & d_{31} & d_{33} & 0 & 0 & 0 & 0 & 0 & \varepsilon_{33}^T \end{bmatrix} \begin{bmatrix} T_1 \\ T_2 \\ T_3 \\ T_4 \\ T_5 \\ T_6 \\ E_1 \\ E_2 \\ E_3 \end{bmatrix} =$$

$$= \begin{bmatrix} S_1 \\ S_2 \\ S_3 \\ S_4 \\ S_5 \\ S_6 \\ D_1 \\ D_2 \\ D_3 \end{bmatrix} \tag{B.19}$$

Therefore, the same relations obtained for PVDF apply to ceramic piezoelectric materials, taking $\varepsilon_{11} = \varepsilon_{22}$, $d_{15} = d_{24}$, $d_{31} = d_{32}$, $s_{11} = s_{22}$ and $s_{44} = s_{55}$.

Appendix C

Electromechanical Piezoelectric Model for different Working Modes

Two equivalent piezoelectric coupling circuits that relate mechanical and electrical magnitudes of the piezoelectric phenomenon are presented. This Appendix show the relations between the parameters that make together the electromechanical piezoelectric model for the case of PVDF materials with working modes 31 and 33. Moreover, two different sets of state variables are presented for the electromechanical piezoelectric models.

C.1 Electromechanical coupling circuits for mode 31 and state variables F, ν, V and I

Figures C.1(a) and C.1(b) show an electromechanical piezoelectric model, [101], [105], [12] and [102], where the state variables are F, ν, V, and I. From piezoelectric constitutive equations, the following expressions are obtained:

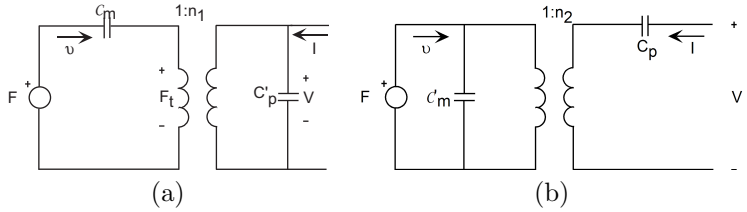

Figure C.1: Piezoelectric coupling circuits, relating mechanical and electrical magnitudes with state variables F, ν, V, and I.

$$\begin{array}{l} \frac{\Delta L}{L} = s_{11}^{E} \frac{F_1}{W t_c} + d_{31} \frac{V_3}{t_c} \\ \frac{Q_3}{WL} = \epsilon_{33}^{T} \frac{V_3}{t} + d_{31} \frac{F_1}{W t_c} \end{array} \tag{C.1}$$

$$\begin{array}{l} \Delta L = L s_{11}^{E} \frac{F_1}{W t_c} + \frac{d_{31} L}{t_c} V_3 \\ Q_3 = \frac{\epsilon_{33}^{T} W L}{t_c} V_3 + \frac{d_{31} L}{t_c} F_1 \end{array} \tag{C.2}$$

$$\begin{array}{l} \Delta L = \mathcal{C}_{m31} F_1 + d_{31} \frac{L}{t_c} V_3 \\ Q_3 = C_p V_3 + d_{31} \frac{L}{t_c} F_1 \end{array} \tag{C.3}$$

Thus, the value of $\mathcal{C}_{m31}$ is:

$$\mathcal{C}_{m31} = \frac{L s_{11}^{E}}{W t_c} \tag{C.4}$$

Thus, the value of C_p is:

$$C_p = \frac{\varepsilon_{33}^{T} A}{t_c} \tag{C.5}$$

Doing the derivative of Equation (C.3), it is obtained:

$$\begin{array}{l} \nu_1 = j\omega \mathcal{C}_{m31} F_1 + j\omega d_{31} \frac{L}{t_c} V_3 \\ I_3 = j\omega d_{31} \frac{L}{t_c} F_1 + j\omega C_p V_3 \end{array} \tag{C.6}$$

From this equation it is obtained the value of F_1 and V_3:

$$F_1 = \frac{\nu}{j\omega \mathcal{C}_{m31}} - \frac{d_{31} L}{\mathcal{C}_{m31} t_c} V_3 \tag{C.7}$$

$$V_3 = \frac{I}{j\omega C_p} - \frac{d_{31} L}{t_c C_p} F_1 \tag{C.8}$$

The following equations are obtained from the analysis of the circuits shown in Figures C.1(a) and C.1(b)

$$F_1 = \frac{\nu}{j\omega \mathcal{C}_{m31}} + F_t \tag{C.9}$$

$$V_3 = \frac{I}{j\omega C_p} + V_t \tag{C.10}$$

Next, it is calculated the transformer ratio for the electromechanical piezoelectric circuit shown in Figures C.1(a) and C.1(b) comparing Equations (C.7) and (C.8) with the previous equations.

$$n_1 = \frac{V_3}{F_t} = -\frac{\mathcal{C}_{m31} t_c}{d_{31} L} \tag{C.11}$$

$$n_2 = \frac{V_t}{F_1} = -\frac{d_{31} L}{t_c C_p} \tag{C.12}$$

The electrical variable I of the two equivalent circuits is analyzed and compared to establish the relation between C'_p and C_p.

$$I_3 = j\omega C'_p V_3 + \nu \frac{L d_{31}}{t_c \mathcal{C}_{m31}} = j\omega d_{31} \frac{L}{t_c} F_1 + j\omega C_p V_3 \tag{C.13}$$

Substituting F_1 in the previous expression for its value in Equation (C.7), it is obtained:

$$j\omega C'_p V_3 = j\omega C_p V_3 - j\omega \frac{d_{31}^2 L^2}{t_c^2 \mathcal{C}_{m31}} V_3 \tag{C.14}$$

Therefore, C'_p and C_p are related by the electromechanical piezoelectric coefficient, k_{31}.

$$C'_p = C_p - \frac{d_{31}^2 L^2}{t_c^2 \mathcal{C}_{m31}} = C_p \left(1 - \frac{d_{31}^2}{s_{11}^E \varepsilon_{33}^T}\right) = C_p \left(1 - k_{31}^2\right) \tag{C.15}$$

Another possible coupling piezolectric model consists in the Norton equivalent circuit of the mechanical part shown in Figure C.1(b) instead of working with the Norton equivalent circuit of the electrical part. The electrical part of the circuit is analyzed and compared with Equation (C.6) to determine the relation between $\mathcal{C}'_{m31}$ and $\mathcal{C}_{m31}$.

$$\nu_1 = j\omega \mathcal{C}_{m31} F_1 + j\omega d_{31} \frac{L}{t_c} V_3 = j\omega \mathcal{C}'_{m31} F_1 + I \frac{d_{31} L}{t_c C_p} \tag{C.16}$$

$$j\omega \mathcal{C}'_{m31} F_1 = j\omega \mathcal{C}_{m31} F_1 - j\omega \frac{L^2 d_{31}^2}{t_c^2 C_p} F_1 \tag{C.17}$$

Therefore, $\mathcal{C}'_{m31}$ and $\mathcal{C}_{m31}$ are also related by the electromechanical coefficient k_{31}.

$$\mathcal{C}'_{m31} = \mathcal{C}_{m31} \left(1 - \frac{L^2 d_{31}^2}{t_c^2 C_p \mathcal{C}_{m31}}\right) = \mathcal{C}_{m31} \left(1 - k_{31}^2\right) \tag{C.18}$$

The relation between the variables of the two equivalent piezoelectric coupling circuits have been determined, as well as, the transformer ratio.

C.1.1 Connection of a Load to the Electromechanical Coupling Circuit

The objective of this section is to determine under which conditions it is achieved the maximum average power of a piezoelectric PVDF film when it is connected to a resistive load, see Figure C.2. Thus, it will be calculated the value of V_3 for the case that a load is connected to the piezoelectric material.

The current flowing through the transformer, I_t, is equal to the current flowing through the resistor, I, and the current flowing through the capacitor $I_{C'_p}$.

$$I_t = I + I_{C'_p} \tag{C.19}$$

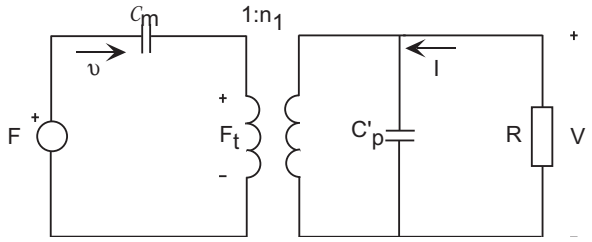

Figure C.2: Piezoelectric coupling circuits, relating mechanical and electrical magnitudes.

I_t is substituted by the product of the transfer ratio of the transformer and $\nu_1 d_{31}$ and I and $I_{C'_p}$ for the division between its voltage and electrical impedance.

$$\frac{\nu_1 d_{31} L}{\mathcal{C}_{m31} t_c} = \frac{V_3}{R} + j\omega C'_p V_3 \tag{C.20}$$

Then, the expression for V_3 is:

$$V_3 = \frac{\nu_1 d_{31} L R}{\mathcal{C}_{m31} t_c \left(1 + j\omega C'_p R\right)} \tag{C.21}$$

Substituting in Equation (C.21), ν_1 and $\mathcal{C}_{m31}$ for Equation (C.4) and $j\omega\Delta L$, respectively, it is obtained:

$$V_3 = \frac{j\omega \Delta L R d_{31} L}{L s_{11}^E / \left(W t_c\right) t_c \left(1 + j\omega R C'_p\right)} = \frac{j\omega R A S_1 Y_{11} d_{31}}{1 + j\omega R \frac{\varepsilon_{33}^T A}{t_c} \left(1 - k_{31}^2\right)} \tag{C.22}$$

The average dissipated power on the load resistor is expressed by Equation (C.23) for a piezoelectric beam with average strain S_1, under a sinusoidal mechanical excitation of angular frequency ω, that gives rise to a sinusoidal voltage waveform with amplitude $|V_3|$.

$$\langle P_{31} \rangle = \frac{\left|V_3^2\right|}{2R} = \frac{\left(d_{31} S_1 A \omega\right)^2 R}{2 s_{11}^E \left(1 + \omega^2 R^2 C_p'^2\right)} \tag{C.23}$$

This expression has a maximum when Equation (C.24) is verified, corresponding to a resistor matching the internal impedance of the piezoelectric film.

$$R = \frac{1}{\omega C'_p} = \frac{1}{\omega \varepsilon_{33}^T \left(1 - k_{31}^2\right) A / t_c} \tag{C.24}$$

Equation (C.25) expresses the value for the maximum average power.

$$\langle P_{max31} \rangle = \frac{d_{31}^2 S_1^2 A^2 \omega}{4 s_{11}^E C'_p} \tag{C.25}$$

C.2 Electromechanical coupling circuits for mode 33 and state variables F, ν, V and I

The state variables employed in the analysis of this section are F, ν, V, and I instead of the state variables T, $\dot{S}$, E, and $\dot{D}$. The analysis of this section is made when the force applied to the piezoelectric element is done along axis 3 instead of along axis 1. The electromechanical equivalent circuit employed is the same shown in Section C.1. From piezoelectric constitutive equation, the following expressions are derived:

$$\begin{array}{l} \frac{\Delta t_c}{t_c} = s_{33}^E \frac{F_3}{A} + d_{33} \frac{V_3}{t_c} \\ \frac{Q_3}{A} = \epsilon_{33}^T \frac{V_3}{t} + d_{33} \frac{F_3}{A} \end{array} \tag{C.26}$$

Arranging the previous expressions, it is obtained:

$$\begin{array}{l} \Delta t_c = t_c s_{33}^E \frac{F_3}{A} + d_{33} V_3 \\ Q_3 = \epsilon_{33}^T \frac{A V_3}{t_c} + d_{33} F_3 \end{array} \tag{C.27}$$

Doing the derivative of Equation (C.27), it is obtained:

$$\begin{array}{l} \nu_3 = j\omega t_c s_{33}^E \frac{F_3}{A} + j\omega d_{33} V_3 \\ I_3 = \epsilon_{33}^T \frac{A V_3}{t_c} + d_{33} F_3 \end{array} \tag{C.28}$$

Comparing the previous equations with the following expressions calculated from the analysis of the electromechanical equivalent circuit, the expressions for $\mathcal{C}_{m33}$ and C_p are deduced.

$$\begin{array}{l} \nu_3 = j\omega \mathcal{C}_{m33} F_3 + j\omega d_{33} V_3 \\ I = j\omega d_{33} F_3 + j\omega C_p V_3 \end{array} \tag{C.29}$$

Thus, the value of $\mathcal{C}_{m33}$ is:

$$\mathcal{C}_{m33} = \frac{t_c s_{33}^E}{A} \tag{C.30}$$

The value of C_p is:

$$C_p = \frac{\varepsilon_{33}^T A}{t_c} \tag{C.31}$$

From these equations, it is obtained the expression for F_3 and V_3:

$$F_3 = \frac{\nu}{j\omega \mathcal{C}_{m33}} - \frac{d_{33} V_3}{\mathcal{C}_{m33}} \tag{C.32}$$

$$V_3 = \frac{I}{j\omega C_p} - \frac{d_{33} F_3}{C_p} \tag{C.33}$$

Next, it is calculated the transformer turn ratios for the electromechanical piezoelectric circuit comparing equations C.32 and C.33 with the following equations obtained from the analysis of the circuit.

$$F_3 = \frac{\nu}{j\omega \mathcal{C}_{m33}} + F_t \tag{C.34}$$

$$V_3 = \frac{I}{j\omega C_p} + V_t \tag{C.35}$$

The transformer turn ratio for the electromechanical equivalent circuit of Figure C.1(a) in working mode 33 is:

$$n_1 = \frac{V_3}{F_t} = -\frac{\mathcal{C}_{m33}}{d_{33}} \tag{C.36}$$

The transformer turn ratio for the electromechanical equivalent circuit of Figure C.1(b) in working mode 33 is:

$$n_2 = \frac{V_t}{F_3} = -\frac{d_{33}}{C_p} \tag{C.37}$$

The electrical part of the two equivalent electromechanical circuits is analyzed and compared to determine the relation between C'_p and C_p.

$$I = j\omega C'_p V_3 + \nu \frac{d_{33}}{\mathcal{C}_{m33}} = j\omega d_{33} F_3 + j\omega C_p V_3 \tag{C.38}$$

Reorganizing the previous expression and substituting ν for its value in Equation (C.29), the relation is found.

$$C'_p = C_p - \frac{d_{33}^2}{\mathcal{C}_{m33}} = C_p \left(1 - \frac{d_{33}^2}{s\varepsilon_{33}^T}\right) = C_p \left(1 - k_{33}^2\right) \tag{C.39}$$

The mechanical part of the two equivalent electromechanical circuits is analyzed and compared to determine the relation between C'_{m33} and C_{m33}.

$$\nu = j\omega \mathcal{C}_{m33} F_3 + j\omega d_{33} V_3 = j\omega \mathcal{C}'_{m33} F_3 + I \frac{d_{33}}{C_p} \tag{C.40}$$

The value of I is replaced by its value in Equation (C.29) to obtain the relation.

$$\begin{aligned} \mathcal{C}'_{m33} &= \mathcal{C}_{m33} \left(1 - \frac{d_{33}^2}{C_p \mathcal{C}_{m33}}\right) = \mathcal{C}_{m33} \left(1 - \frac{d_{33}^2 t_c A}{\varepsilon A t_c s_{33}^E}\right) = \mathcal{C}_{m33} \left(1 - \frac{d_{33}^2}{\varepsilon s_{33}^E}\right) = \\ &= \mathcal{C}_{m33} \left(1 - k_{33}^2\right) \end{aligned} \tag{C.41}$$

The electromechanical coupling coefficient relates both sets of variables as in the working mode 31.

C.2.1 Connection of a Load to the Electromechanical Coupling Circuit

Next, it will be calculated the value of V_3 for the case that a load is connected to the piezoelectric material. The Kirchoff analysis of the current flowing in the electrical part of the electromechanical coupling circuit gives the following expression:

$$I_t = I + I_{C'_p} \tag{C.42}$$

where I_t, I and $I_{C'_p}$ are the current flowing through the transformer, the resistive load and C'_p, respectively.

I_t is substituted by the product of the transfer ratio of the transformer and $\nu_3 d_{33}$ and I and $I_{C'_p}$ for the division between its voltage and electrical impedance.

$$\frac{\nu_3 d_{33}}{\mathcal{C}_{m33}} = \frac{V_3}{R} + j\omega C'_p V_3 \tag{C.43}$$

Substituting in Equation (C.43), ν_3 and $\mathcal{C}_{m33}$ for Equation (C.30) and $j\omega\Delta t_c$, respectively, it is obtained:

$$V_3 = \frac{j\omega\Delta t_c R d_{33} A}{s^E_{33}/t_c \left(1 + j\omega R C'_p\right)} = \frac{j\omega R A S_3 Y_{33} d_{33}}{1 + j\omega R \frac{\varepsilon^T_{33} A}{t_c}\left(1 - k^2_{33}\right)} \tag{C.44}$$

The dissipated power on the load resistor is expressed by Equation (C.45) for a piezoelectric beam with average strain S_3, under a sinusoidal mechanical excitation of angular frequency ω, that gives rise to a sinusoidal voltage waveform with amplitude $|V_3|$.

$$\langle P_{33} \rangle = \frac{\left|V_3^2\right|}{2R} = \frac{\left(d_{33} S_3 A \omega\right)^2 R}{2 s^E_{33}\left(1 + \omega^2 R^2 C'^2_p\right)} \tag{C.45}$$

This expression has a maximum when Equation (C.46) is verified, corresponding to a resistor matching the internal impedance of the piezoelectric film.

$$R = \frac{1}{\omega C'_p} = \frac{1}{\omega \varepsilon^T_{33}\left(1 - k^2_{33}\right) A/t_c} \tag{C.46}$$

Equation (C.47) expresses this value of the maximum average power.

$$\langle P_{max33} \rangle = \frac{d^2_{33} S^2_3 A^2 \omega}{4 s^E_{33} C'_p} \tag{C.47}$$

C.3 Electromechanical piezoelectric model for mode 31 and state variables T, $\dot{S}$, E and $\dot{D}$

Figures C.3(a) and C.3(b) show an electromechanical piezoelectric model where the state variables are F, ν, V, and I. The transformer relates mechanical

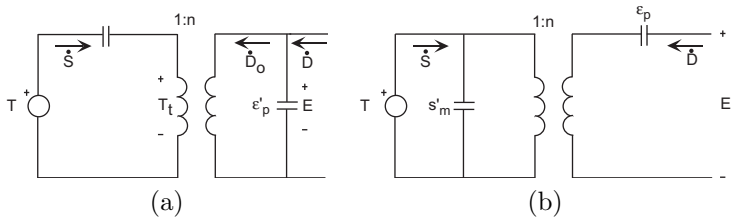

Figure C.3: Piezoelectric coupling circuits, relating mechanical and electrical magnitudes.

magnitudes (stress) and electrical magnitudes (electric field). If the piezoelectic constitutive equations are transformed to the Fourier domain, the following equations are obtained:

$$\begin{aligned} \dot{S}_1 &= j\omega s_{11}^E T_1 + j\omega d_{31} E_3 \\ \dot{D}_3 &= j\omega d_{31} T_1 + j\omega \varepsilon_{33}^T E_3 \end{aligned} \tag{C.48}$$

This equation can be expressed also using Young's modulus, Y, that is defined as the mechanical stress obtained when a strain is applied.

$$\begin{aligned} \dot{S}_1 &= j\omega \tfrac{1}{Y_{11}} T_1 + j\omega d_{31} E_3 \\ \dot{D}_3 &= j\omega d_{31} T_1 + j\omega \varepsilon_{33}^T E_3 \end{aligned} \tag{C.49}$$

The equations derived from the circuit represented by Figure C.3(a) are:

$$\tfrac{\dot{S}_1}{j\omega s_m} + T_t - T_1 = 0 \dot{D}_3 - j\omega E_3 \varepsilon'_p - \dot{D}_{3o} = 0 \tag{C.50}$$

The transformer turns ratio between the mechanical and the electrical part of the piezoelectric equivalent circuit relates both sides. For Figure C.3(a), the relation between the electrical and mechanical parts is given by:

$$\dot{S}_3 = -n_1 \dot{D}_{3o} \tag{C.51}$$

$$E_3 = n_1 T_t \tag{C.52}$$

Equation (C.49) can be expressed as:

$$\frac{\dot{S}_1 Y_{11}}{j\omega} = T_1 + E_3 Y_{11} d_{31} \tag{C.53}$$

Comparing Equations (C.50) and (C.53), it is deduced that:

$$T_t = -E_3 Y_{11} d_{31} \tag{C.54}$$

Therefore, turns ratio of the transformer can be expressed as a function of the piezoelectric constants.

$$n_1 = \frac{E_3}{T_t} = -\frac{1}{Y_{11} d_{31}} \tag{C.55}$$

The value of s_m can be easily determined from Equation (C.50).

$$s_m = \frac{1}{Y_{31}} \tag{C.56}$$

The value of
$dotD_{3o}$ is calculated combining Equations (C.55) and (C.51):

$$\dot{D}_{3o} = \dot{S}_1 Y_{11} d_{31} \tag{C.57}$$

The expression of ε'_p as a function of the piezoelectric constants is calculated employing the following expression that is derived from the analysis of the electrical part of the circuit of Figure C.1(a).

$$\dot{D}_3 = j\omega E_3 \varepsilon'_p + \dot{S}_1 Y_{11} d_{31} \tag{C.58}$$

Substituting in the previous Equation the value of $\dot{D}_3$ by the value given by Equation (C.49), it is obtained:

$$j\omega E_3 \varepsilon'_p = j\omega \varepsilon_{33}^T E_3 + j\omega d_{31} T_1 - \dot{S}_1 Y_{11} d31 \tag{C.59}$$

Reordering the previous equation and employing the first expression of Equation (C.49), it is deduced:

$$j\omega E_3 \varepsilon'_p = j\omega \varepsilon_{33}^T E_3 + d_{31} Y_{11} \left(-j\omega d_{31} E_3\right) \tag{C.60}$$

Thus, the value for ε'_p is calculated using the relation between piezoelectric constants $\frac{d_{31}^2}{s_{11}^E \varepsilon_{33}^T} = k_{31}^2$ that appears in Table 3.3.

$$\begin{aligned} \varepsilon'_p = \varepsilon_{33}^T - d_{31}^2 Y_{11} = \varepsilon_{33}^T \left(1 - \frac{d_{31}^2 Y_{11}}{\epsilon_{33}^T}\right) = \\ = \varepsilon_{33}^T \left(1 - \frac{d_{31}^2}{s_{11}^E \varepsilon_{33}^T}\right) = \varepsilon_{33}^T \left(1 - k_{31}^2\right) \end{aligned} \tag{C.61}$$

Another possibility for the representation of the piezoelectric coupling circuit is shown in Figure C.3(b). The relation of the components of this circuit and the piezoelectric constants are calculated below. Moreover, it is also calculated its relation with the components of the equivalent circuit represented in Figure C.3(a).The turns ratio of the transformer, n_2, is calculated employing the equations extracted from the analysis of the circuit shown in Figure C.3(b).

$$\begin{aligned} \dot{S}_1 = j\omega s'_m T_1 - n_2 \dot{D}_3 \\ E_3 = j\omega \varepsilon_p \dot{D}_3 + n_2 T_1 \end{aligned} \tag{C.62}$$

The previous equation can be also expressed as:

$$\dot{D}_3 = j\omega\varepsilon_p E_3 - j\omega\varepsilon_{33}^T n_2 T_1 \tag{C.63}$$

Comparing the above expression with the value of $\dot{D}$ from Equation (C.49), it is obtained that the value of the transformer ratio is:

$$n_2 = -d_{31}/\varepsilon_{33}^T \tag{C.64}$$

The value of ε_p is:

$$\varepsilon_p = \varepsilon_{33}^T \tag{C.65}$$

The component ε_p of the circuit of Figure C.3(b) is related with the component ε_p' of the circuit of Figure C.3(a).

$$\varepsilon_p = \varepsilon_p' \left(1 - k_{31}^2\right) \tag{C.66}$$

In order to determine the value of s_m', it is employed the expression for $\dot{S}_1$ of Equation (C.62).

$$\dot{S}_1 = j\omega T_1 s_m' + \frac{d_{31}}{\varepsilon_{33}^T}\dot{D}_3 \tag{C.67}$$

When the above expression is equaled to the expression of $\dot{S}_1$ given in Equation (C.49), it is gotten the value of s_m' as a function of the piezoelectric constants.

$$j\omega T_1 s_m' + \frac{d_{31}}{\varepsilon_p}\dot{D}_3 = j\omega\frac{T_1}{Y_{11}} + j\omega d_{31} E_3 \tag{C.68}$$

Reordering the previous expression and employing the second expression that appears in Equation (C.49), the value of s_m' is obtained.

$$s_m' = \frac{1}{Y_{11}} - \frac{d_{31}^2}{\varepsilon} = \frac{1}{Y_{11}}\left(1 - \frac{d_{31}^2 Y_{11}}{\varepsilon_{33}^T}\right) = \frac{1}{Y_{11}}\left(1 - k_{31}^2\right) \tag{C.69}$$

Comparing Equation (C.56) and Equation (C.69), it is deduced that s_m and s_m' are related as the other components of the two equivalent circuits through the electromechanical coupling coefficient.

$$s_m' = s_m\left(1 - k_{31}^2\right) \tag{C.70}$$

C.3.1 Connection of a Load to the Electromechanical Coupling Circuit

The objective of this section is to determine under which conditions it is achieved the maximum average power of a piezoelectric PVDF film when it is connected to a resistive load, see Figure C.4. Thus, it will be calculated the value of V_3 for the case that a load is connected to the piezoelectric material. From the analysis of the circuit, the following equations are deduced.

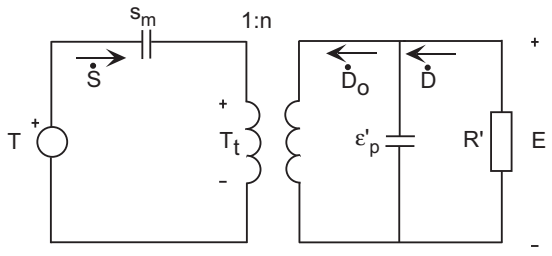

Figure C.4: Piezoelectric coupling circuit relating mechanical and electrical magnitudes with a resistive load.

$$-\left(\dot{D}-\dot{D}_o\right)C_p+\dot{D}_3R'=\dot{D}_o \tag{C.71}$$

$$\dot{S}_1Y_{11}d_{31}=-\dot{E}_3\varepsilon'_p-\frac{E_3}{R'} \tag{C.72}$$

Then, the expression for V_3 taking into account the relation $E_3=V_3/t_c$ and using Equation (C.72) and Equation (C.72) is calculated.

$$V_3=-\frac{j\omega R'S_1Y_{11}d_{31}t_c}{j\omega R'\varepsilon_{33}^T\left(1-k_{31}^2\right)+1} \tag{C.73}$$

Since the state variables in the electrical part of the circuit are E, and $\dot{D}$ instead of V and I, the load is represented as R'. There is a relation between R' and the resistive load R. This relation is calculated comparing Equation (C.75) derived from the circuit of Figure C.2 and Equation (C.74) derived from Figure C.4.

$$\frac{E_3}{=}-\dot{D}_3R' \tag{C.74}$$

$$V_3=-I_3R \tag{C.75}$$

In the previous equation, the state variables V and I are substituted for E and $\dot{D}$, respectively.

$$\dot{D}_3=-E_3\frac{t_c}{RA} \tag{C.76}$$

where $A=WL$.

Therefore, comparing Equation (C.74) with Equation (C.76), the existing relation between R' and R is found.

$$R'=R\frac{A}{t_c} \tag{C.77}$$

Substituting the result obtained from R' in Equation (C.73), it is obtained:

$$V_3 = -\frac{j\omega RAS_1 Y_{11} d_{31}}{j\omega RA/t_c \epsilon_{33}^T (1-k_{31}^2)+1} = -\frac{j\omega RAS_1 e_{31}}{j\omega RA/t_c \epsilon_{33}^T (1-k_{31}^2)+1} \tag{C.78}$$

The optimum value of R, R_{opt}, is given by the following expression. When $R = R_{opt}$ the value of V_3 is maximum.

Hence, the same results are obtained employing state variables T, $\dot{S}$, E, and $\dot{D}$ instead of state variables F, ν, V, and I, demonstrating that both models are equivalents.

C.4 Electromechanical piezoelectric model for mode 33 and state variables T, $\dot{S}$, E and $\dot{D}$

If the piezoelectic constitutive equations are transformed to the Fourier domain, the following equations are obtained:

$$\begin{aligned} \dot{S}_3 &= j\omega s_{33}^D T_3 + j\omega d_{33} E_3 \\ \dot{D}_3 &= j\omega d_{33} T_3 + j\omega \varepsilon_{33}^T E_3 \end{aligned} \tag{C.79}$$

The first equation can be expressed using Young's modulus, Y, instead of the compliance s^D.

$$\begin{aligned} \dot{S}_3 &= j\omega \tfrac{1}{Y_{33}} T_3 + j\omega d_{33} E_3 \\ \dot{D}_3 &= j\omega d_{33} T_3 + j\omega \varepsilon_{33}^T E_3 \end{aligned} \tag{C.80}$$

The transformer between the mechanical and the electrical part of the piezoelectric equivalent circuit is calculated in the same way that in the previous section. The result obtained is:

$$n_2 = -\frac{1}{Y_{33} d_{33}} \tag{C.81}$$

The value of s_m is:

$$s_m = \frac{1}{Y_{33}} \tag{C.82}$$

The value of ε_p':

$$\begin{aligned} \varepsilon_p' &= \epsilon_{33}^T - d_{33}^2 Y_{33} = \varepsilon_{33}^T \left(1 - \frac{d_{33}^2 Y_{33}}{\varepsilon_{33}^T}\right) = \varepsilon_{33}^T \left(1 - \frac{d_{33}^2}{s_{33}^E \varepsilon_{33}^T}\right) = \\ &= \varepsilon_{33}^T \left(1 - k_{33}^2\right) \end{aligned} \tag{C.83}$$

where k_{33} is the mechanical coupling factor for the thickness expansion working mode.

Therefore,

$$k_{33}^2 = \frac{d_{33}^2 Y_{33}}{\varepsilon_{33}^T} \tag{C.84}$$

Another possibility for the representation of the piezoelectric coupling circuit is shown in Figure C.3(b). In this case, the turns ratio of the transformer, n_2, is:

$$n_2 = -d_{33}/\epsilon_{33}^T \tag{C.85}$$

The component ε_p of the electromechanical circuit expressed as a function of the piezoelectric constants is:

$$\varepsilon_p = \epsilon_{33}^T \tag{C.86}$$

ε_p and ε_p' are related through the electromechanical coupling coefficient.

$$\varepsilon_p = \varepsilon_p' \left(1 - k_{33}^2\right) \tag{C.87}$$

In order to determine the value of s_m', it is employed the following expression that is extracted from the analysis of the circuit represented by Figure C.3(b):

$$\dot{S} = j\omega T s_m' + \frac{d}{\varepsilon}\dot{D} \tag{C.88}$$

The value of s_m' as a function of Y_{33} is:

$$s_m' = \frac{1}{Y_{33}} - \frac{d_{33}^2}{\epsilon} = \frac{1}{Y_{33}}\left(1 - \frac{d_{33}^2 Y_{33}}{\epsilon_{33}^T}\right) = \frac{1}{Y_{33}}\left(1 - k_{33}^2\right) \tag{C.89}$$

s_m and s_m' are related through the electromechanical coupling coefficient in working mode 33, k_{33}.

$$s_m' = s_m \left(1 - k_{33}^2\right) \tag{C.90}$$

The analysis of the connection of a resistive load to the electromechanical coupling circuit is not done since it has been demonstrated in Section C.3.1 that this calculation is equivalent to the one done for working mode 33 employing state variables F, ν, V, and I.

Appendix D

Acceleration Measurements on the Human Body

Figure D.1 shows the acceleration measurements of X-axis and Y-axis of an accelerometer placed on an ankle while a person was walking. Figure D.2 and Figure D.3 show a zoom of the previous figure for X-axis and Y-axis, respectively. Figures D.4 and D.5 show the acceleration spectrum for the same activity and location for X-axis and Y-axis, respectively, obtained applying a Hamming window and the FFT algorithm to the measured data. The two main peaks of the acceleration spectrum are at a frequency of 0.8 Hz and 1.6 Hz for both axis.

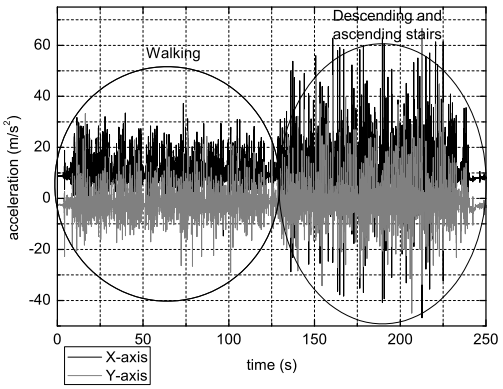

Figure D.1: Acceleration measurements obtained by placing the sensor node on the ankle while a person was walking and descending and ascending stairs with T_s=0.013s.

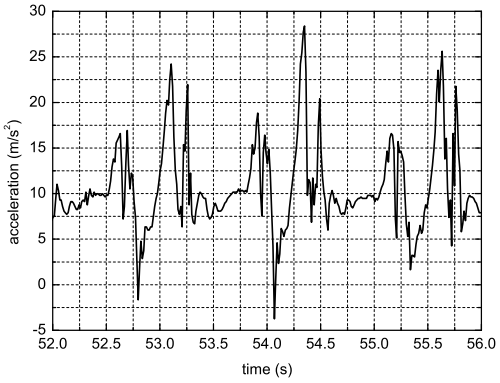

Figure D.2: X-axis acceleration measurements obtained by placing the sensor node on the ankle while a person was walking with T_s=0.013s.

Figure D.6 shows the acceleration measurements of X-axis and Y-axis of an accelerometer placed on a wrist while a person was walking. Figure D.7 and Figure D.8 show a zoom of the previous figure for X-axis and Y-axis, respectively.Figure D.9 shows the spectrum of the acceleration measurements of Y-axis. The highest peak is at 0.8 Hz.

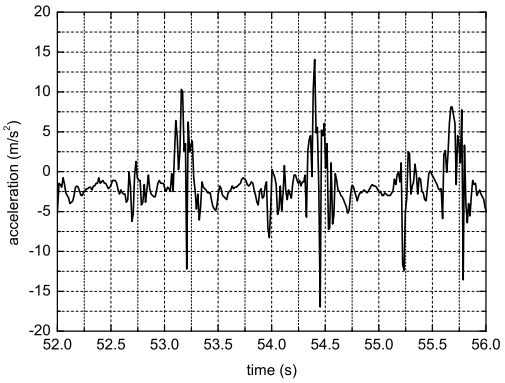

Figure D.3: Y-axis acceleration measurements obtained by placing the sensor node on the ankle while a person was walking with T_s=0.013s.

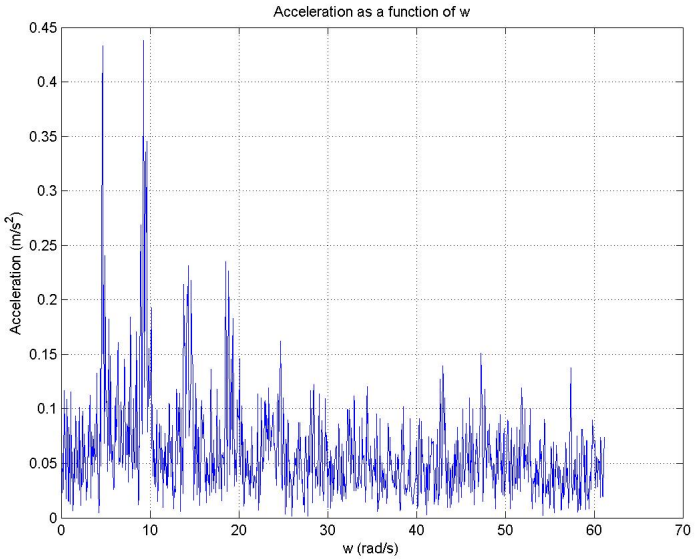

Figure D.4: Acceleration spectrum calculated from measurements obtained by placing an accelerometer on the ankle of a person that was walking with T_s=0.013s for X-direction.

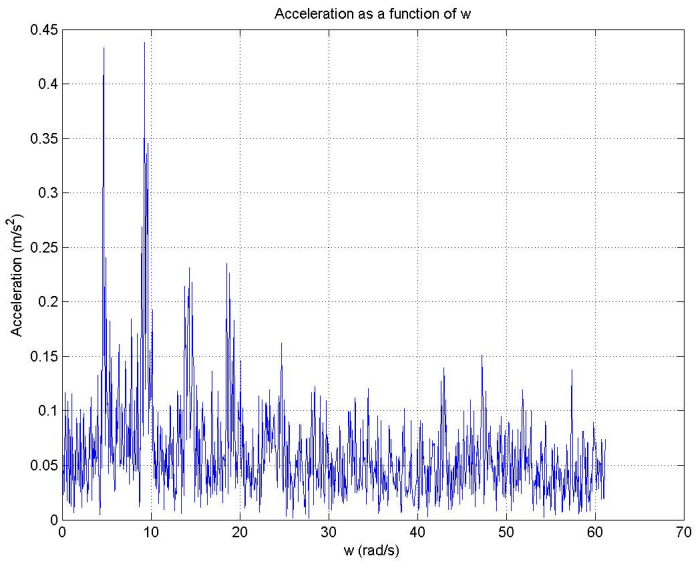

Figure D.5: Acceleration spectrum calculated from measurements obtained by placing an accelerometer on the ankle of a person that was walking with T_s=0.013s for Y-direction.

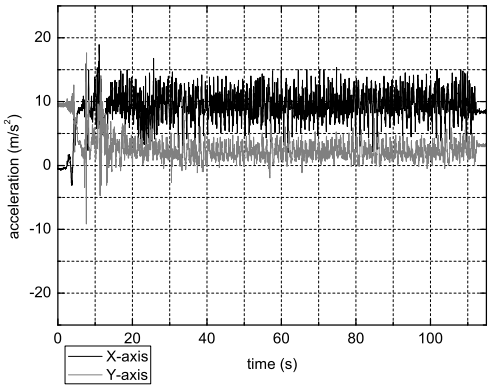

Figure D.6: Acceleration measurements obtained by placing the sensor node on the wrist while a person was walking with T_s=0.013s.

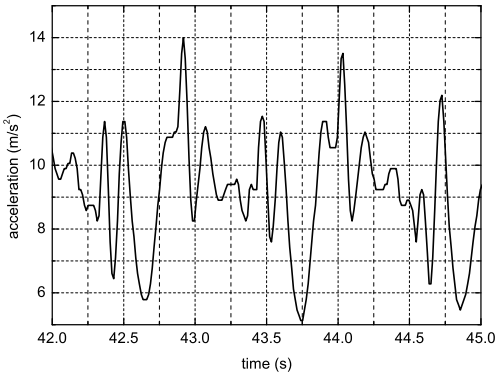

Figure D.7: X-axis acceleration measurements obtained by placing the sensor node on the wrist while a person was walking with T_s=0.013s.

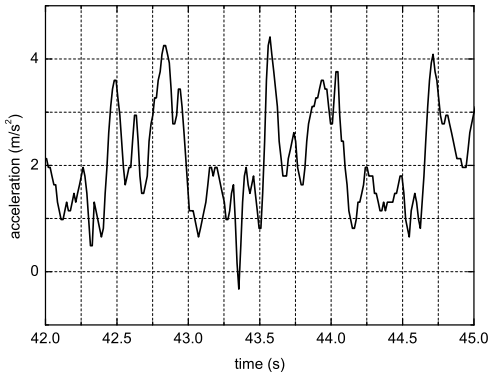

Figure D.8: Y-axis acceleration measurements obtained by placing the sensor node on the wrist while a person was walking with T_s=0.013s.

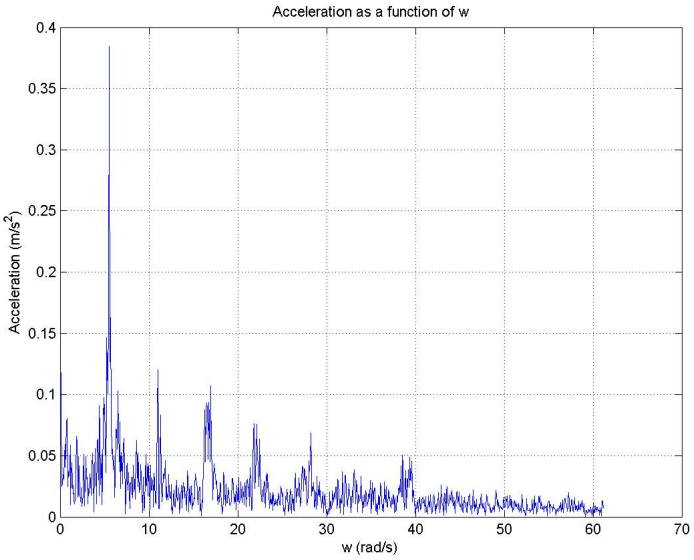

Figure D.9: Acceleration spectrum calculated from measurements obtained by placing an accelerometer on the wrist of a person that was walking with T_s=0.013s for Y-direction.

Appendix E

Characterization of Thermoelectric Modules (TEMs)

Table E.1 and Table E.2 show the measurement obtained employing two different thermogenerators. The thermogenerators were connected to different resistive loads: R_2, R_3, R_4 and R_5 while the hot side of the TEG was heated. The data shown has been obtained after waiting two hours in order to assure stabilized temperatures at both sides of the TEG [132]. The parameters measured were the voltage of the TEG in open circuit, V_{oc}, the voltages on the resistive loads connected to the TEG (V_2, V_3, V_4 and V_5) as well as the temperature at the hot side, T_H, and cold side, T_C.

Table E.1: Measurements obtained from the 17 A 1015 H 200 Peltron thermogenerator.

R_2 (Ω)	2.26	2.25	2.25	2.25	2.25	2.25
R_3 (Ω)	11.03	11.03	11.02	11.03	11.03	11.03
R_4 (Ω)	113.90	113.89	113.89	113.89	113.89	113.89
R_5 (Ω)	1185.13	1185.12	1185.15	1185.14	1185.12	1185.11
V_{oc} (mV)	55.09	83.43	110.17	132.46	167.49	214.74
V_2 (mV)	33.82	50.81	66.46	79.13	99.11	126.06
V_3 (mV)	50.07	75.67	99.71	119.59	150.86	193.03
V_4 (mV)	54.56	82.61	109.06	131.10	165.71	212.41
V_5 (mV)	55.03	83.33	110.04	132.30	167.28	214.47
T_H ($^\circ C$)	38.93	48.93	58.86	68.79	78.74	88.69
T_C ($^\circ C$)	30.32	34.87	39.59	45.22	49.60	54.23

From these tables, it can be deduced the value of the parameters α_m and R_m. The values of these parameters is not constant and depend on the absolute

Table E.2: Mesurements obtained from the 128 A 1030 Peltron thermogenerator.

R_2 (Ω)	2.25	2.26	2.26	2.26	2.26	2.26
R_4 (Ω)	113.89	113.89	113.89	113.90	113.90	113.90
R_5 (Ω)	1185.13	1185.13	1185.11	1185.10	1185.11	1185.12
V_{oc} (mV)	333.70	530.66	743.18	960.17	1178.59	1394.76
V_2 (mV)	47.50	72.91	98.70	123.38	146.71	168.38
V_4 (mV)	306.240	485.29	677.36	872.27	1067.17	1258.80
V_5 (mV)	330.55	525.43	735.58	950.02	1165.71	1379.03
T_H $(°C)$	39.06	49.09	59.13	69.16	79.18	89.23
T_C $(°C)$	32.35	37.73	42.58	47.44	52.26	57.17

temperature of one side and on the temperature gradient.

Table E.3: Parameters calculated from the measurements obtained for the 17 A 1015 H 200 Peltron thermogenerator.

α (V/K)	R_m (Ω)	T_H $(°C)$	T_C $(°C)$	ΔT
0.00643	1.418	38.928	30.321	8.607
0.00593	1.443	48.929	34.870	14.059
0.00572	1.476	58.860	39.589	19.271
0.00562	1.516	68.793	45.217	23.576
0.00575	1.554	78.737	49.603	29.135
0.00623	1.586	88.688	54.234	34.454

Table E.4: Parameters calculated from the measurements obtained for the 128 A 1030 Peltron thermogenerator.

α (V/K)	R_m (Ω)	T_H $(°C)$	T_C $(°C)$	ΔT
0.04971	10.213	39.058	32.345	6.713
0.0467	10.649	49.093	37.728	11.364
0.04489	11.066	59.132	42.578	16.554
0.04421	11.478	69.158	47.442	21.716
0.04377	11.891	79.182	52.256	26.926
0.04351	12.302	89.227	57.173	32.054

Tables E.5 and E.6 show the data given by the manufacturer for the 17 A 1015 H 200 and 128 A 1030 Peltron TEGs, respectively.

Table E.5: Electrical and thermal parameters for the TEG 17 A 1015 H200.

Symbol	Description	Value	Units
Q_{max}	Maximum amount of heat that can that can be absorbed at TEMs cold plate at I_{max} and ΔT=0.	3.5	W
ΔT_{max}	Largest temperature differential between the hot and cold side plates of a TEM for the given value of T_h	67	K
V_{max}	DC voltage that delivers the ΔT_{max} at the supplied I_{max}	2.1	V
I_{max}	Input current that produces ΔT_{max} across a TEM	2.5	A
T_{max}	Maximum temperature at the hot side	473	K
R_i	Internal resistance	0.7	Ω
α_m	Seebecks coefficient	0.0065	V/K
k_m	Thermal conductance	0.039	W/K
Θ_m	Thermal resistance	25.57	K/W
C_m	Heat capacity	0.61	J/K
Z	Figure of Merit	1.54e-3	K^{-1}
	Dimensions	11.5x11.5x3.2	

Table E.6: Electrical and thermal parameters for the TEG PKE 128 A 1030.

Symbol	Description	Value	Units
Q_{max}	Maximum amount of heat that can that can be absorbed at TEMs cold plate at I_{max} and ΔT=0.	14	W
ΔT_{max}	Largest temperature differential between the hot and cold side plates of a TEM for the given value of T_h	65	K
V_{max}	DC voltage that delivers the ΔT_{max} at the supplied I_{max}	15	V
I_{max}	Input current that produces ΔT_{max} across a TEM	1.5	A
T_{max}	Maximum temperature at the hot side	398	K
R_i	Internal resistance	7.7	Ω
α_m	Seebecks coefficient	0.049	V/K
k_m	Thermal conductance	0.157	W/K
Θ_m	Thermal resistance	6.38	K/W
Z	Figure of Merit	1.99e-3	K^{-1}
	Dimensions	25x25x5.2	mm
	Weight	10	g

Appendix F

Battery

The design of the power management system to power portable devices from energy harvesting sources is complicated due to the low voltage ranges in the case of thermoelectric and inductive transducers or due to the low current ranges in the case of piezoelectric generators. If a battery requires to be charged with energy harvesting transducers, it is necessary an accurate battery model to predict its behaviour and to give information about the state of charge (SOC) of the battery. The SOC of the battery is employed to estimate if the energy harvesting system is working in energy neutral operation. As it is explained in Chapter 6, next sections enter into more detail in the battery electrical model and the state of charge topics. Moreover, the measurement procedure to extract the parameters of the battery electrical model is also detailed.

F.1 State of Charge

The SOC is defined as the percentage of the maximum possible charge that is present inside the battery [91]. The main methods for the determination of the SOC are:

1. Direct measurement. The most used direct measurement method is the battery voltage measurement. This method implies the measurement of the voltage on the battery and is less expensive and requires less computing power than the coulomb counting method. It is the method employed for example in mobile phone applications. While it is true that a given cell's voltage level will continually drop during discharge, the voltage level's relationship to remaining charge varies greatly over cell temperature and discharge rate [133]. Therefore, this method is not appropriate for example for Li-ion and NiMH cells since the voltage on the battery at a given SOC varies with the value of the discharge current as can be seen in Figures F.5 and F.6. The error in SOC estimation can be corrected, if the temperature and the discharge rate of the battery are also measured and

compared with previously memorized data using look-up tables or functions [91]. However, this will make the SOC estimation more complicated and expensive than the coulomb counting method without providing any significant advantages.

2. Coulomb counting. This method implies an accurate measurement of the current flowing into or out of the battery and an integration of this current to calculate the SOC [91, 95, 133]. Therefore, this method takes into account that the capacity of a battery changes with the discharge current. If it is considered that the current is constant, then the SOC is defined as [95]:

$$SOC = \frac{ICA - C_{EMPTY}}{C_{FULL} - C_{EMPTY}} \times 100 \tag{F.1}$$

where $ICA = I \times t$ is the charge accumulated or removed from the battery, C_{FULL} is the capacity of the battery when it is charged completely C_{EMPTY} is the capacity that remains in the battery when it is considered that is discharged completely. In this case the battery is first charged at constant current, $1C$, until it reaches the maximum voltage on the battery and then it is charged at constant voltage until the charge current fell below $C/20$. In [95], the ICA register is reset to the value of C_{EMPTY} when the battery is fully discharged and it is reset to the value of C_{FULL} when the battery is fully charged. Summarizing, if $ICA = C_{EMPTY}$, the $SOC = 0\%$ and if $ICA = C_{FULL}$, the $SOC = 100\%$.

If it is considered that $C_{EMPTY} = 0$, then $C_{FULL} = C_{AVAILABLE}$ and Equation (F.1) can be expressed as Equation (F.2). Moreover, the available capacity depends on the temperature and the value of the current when it is charged or discharged and this is the reason for expressing $C_{AVAILABLE}$ as a function of these two variables in Equation (F.2).

$$SOC = \frac{I \times t}{C_{AVAILABLE}(I, T)} \times 100 \tag{F.2}$$

h where $C_{AVAILABLE}(I, T)$ is the available capacity of the battery when it has been completely charged at $1C$ and then discharged with a constant current value I at a temperature T, I is the constant current employed to charge or discharge the battery and t is the time employed for the process.

An improvement of Equation (F.2) is done with Equation (F.3) since it is possible to calculate the SOC when different currents and temperatures are employed in the process of charging or discharging the battery with the introduction of a new variable, the initial state of charge, $SOC_{initial}$.

$$SOC = SOC_{initial} + \frac{I \times t}{C_{AVAILABLE}(I, T)} \times 100 \tag{F.3}$$

where $SOC_{initial}$ is the previous state of charge of the battery, I is the current flowing into (positive sign) or out of the battery (negative sign), and t is the time employed to charge or discharge the battery with a current I. The sign of I is positive when the battery is being charged and is negative when the battery is being discharged.

Temperature and discharge rates have high effects in the capacity of a Li-Ion battery. Other effects like the self-discharge of the battery are not relevant with this kind of chemistry.

[91] presents a new algorithm to predict the SOC of a battery based on the Coulomb counting method. The proposed algorithm operates in five different states: initial state, equilibrium state, transitional state, discharge state and charge state.

3. Adaptive systems. This method is based on a comparison that is made whenever possible between the estimated values with observed battery behavior [91].

A topic related with the calculation of the state of charge of batteries is the capacity of the cells that, as it is explained and observed in Section F.3 for the case of the Lithium-Ion cells, varies greatly depending on the temperature and discharge rate. Moreover, it is only necessary to keep track of the present cell temperature and discharge rate when determining remaining capacity [95] since most other conditions like heat losses during charging process or self-discharge have little or no effect on charge capacity. Thus, all these conditions can be ignored for the calculus of the capacity.

Theoretically, the capacity should be independent of the discharge rate since an identical amount of energy is dispensed during different times. Due to energy loss that occurs inside the battery and a drop in voltage that causes the battery to reach the low-end voltage cut-off sooner with high discharge rates, the capacity reading is lower in these cases. The discrepancy in capacity readings with different C-rates largely depends on the internal resistance of the battery.

The temperature is also an important factor that modifies the capacity of the battery. At room and high temperatures, the lithium cells have a great capacity. At low temperatures the capacity decrease drastically.

F.2 Electrical Models

This section gives a summary of different equivalent circuits that model the behavior of batteries and it is focused specially in the model proposed by Chen et al. in [3] since it is the model implemented in [13] (Chapter 13). These models are a combination of voltage sources, resistors and capacitors and are classified in three different categories: Thevenin, impedance, and runtime-based models [3].

The right circuit shown in Figure F.1 is a Thevenin battery model. The electrical components and signals of this circuit are: V_{oc}, the battery open-circuit voltage, V_{Batt},the battery voltage, I_{bat}, the battery current, R_{series}, the

constant part of the internal resistance that is caused by the connector, the electrodes and the electrolyte of the battery and two RC parallel networks. The two RC networks predict the battery response to transient load events. There are two exponential decay constants: a fast constant determined by R_{tran_S} and C_{tran_S} and a slow constant determined by R_{tran_L} and C_{tran_L}. R_{tran_S} and C_{tran_S} (slow exponential decay constant) describe the effects on the surface of the electrodes whereas $R_{tran_L}$and C_{tran_L} (fast exponential decay constant) describe diffusion processes in the electrolyte [134]. This model is not very accurate when it is not taken into account that the value of the electrical components depends on the state of charge of the battery [3].

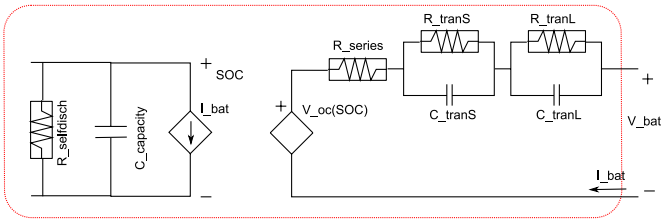

Figure F.1: Electrical model of the battery [3]

There are another models like the impedance-based electrical model that is applied to lithium batteries [135]. Nonlinear electrical modes presents a battery equivalent circuit with the following components: V_b, battery voltage, i_b, current source, V_oc, open circuit voltage is the voltage across R_p and C_b, C_b, battery capacity R_p, self-discharge resistance [135, 136].

The runtime models use a complex circuit network and are able to simulate battery runtime and the DC voltage response for a constant discharge current in a simulator. A complete model that is a combination of the exposed model is implemented by Chen et al. to obtain a battery model that can predict battery runtime and I-V performance [3].

The battery electrical model proposed by Chen et al. see Figure F.1, is divided in two circuits. The left circuit called battery lifetime estimates the state of charge of the battery whereas the right circuit named voltage-current characteristics is a RC network based in the Thevenin electrical battery models. The voltage value of V_{SOC} relates both circuits using the state of charge of the battery. This voltage is equivalent to the SOC of the battery and it has a value between zero ($SOC = 0$, battery discharged) and one volt ($SOC = 1$, battery fully charged) and it at so much per one. In the circuit that models the battery lifetime, the capacitor $C_{capacity}$ corresponds to the capacity of the battery and the resistor $R_{selfdisch}$ characterizes the self-discharge energy loss. However, for the purpose of the electrical model here presented is not necessary to include this parameter into our model since in Li-Ion batteries, it can be ignored. The values of the second circuit of the battery model: $V_{oc}(SOC)$, R_{series}, R_{tran_S}, C_{tran_S}, R_{tran_L}, and C_{tran_L} depend on the state of charge of the battery.

The value of $C_{Capacity}$ represents the capacity of the battery and its value is defined by the following expression as:

$$C_{capacity} = 3600 Capacity f_1(Cycle) f_2(Temp) \tag{F.4}$$

where $C_{Capacity}$is the nominal capacity of the battery expressed in Ahr, $f_1(Cycle)$ is a cycle-number dependent correlation factor and $f_2(Temp)$ a temperature dependent correlation factor. However, there is no correlation factor due to the value of the discharge current in [3]. Moreover, it is specified that $C_{Capacity}$ will not change with current variation since energy is conserved. It is explained that the usable capacity is reduced when the discharge current is increased due to different SOC value at the end of discharge for different currents owing to different voltage drops across internal resistor ($R_{series} + R_{trans} + R_{tran_L}$) and the same end-of-discharge voltage.

F.3 Battery Measurements and Parameters Calculation of the Electrical Model

This section shows the necessary measurements done with a Lithium polymer battery in order to calculate the parameters of the electrical model presented in the previous section. The battery characterized, see Figure F.2, was the model 602030 from Bullith with a nominal capacity of 75 mAh and a voltage range between 1.8 V and 2.8 V. All the measurements were done with the batteries placed inside a a CTS temperature chamber T-40/50 [137], see Figure F.3. The battery measurement setup is described in [22] (Chapter 13).

Figure F.2: Lithium polymer battery, model 602030 from Bullith

The method employed to calculate the parameters of the electrical model is the same one used in [3]. This method consists on the calculation of the electrical parameters of the battery electrical model as a function of the state of charge of the battery. The method consists in completely charging the battery and then discharging it each time with different current values to evaluate the dependence of its parameters with the discharge current employed. The battery is discharged

Figure F.3: Measurement setup for battery characterization including a climate chamber.

with constant current in order to observe the voltage drop and the exponential response to extract the value of the parameters of the electrical model. When the battery is being discharged, the SOC varies, and so do, the parameters of the electrical model. For this reason, the parameters of the electrical model are calculated at different values of SOC when it is constant (in the relaxation time, when the current is equal to zero). Therefore, the first measurements to do consist on the charge and discharge of the battery at different discharge currents in order to calculate the available capacity for each discharge current. The usual method to fully charge a Lithium battery consists first in charge the battery with a constant current (between $0.1C$ to $1C$) until it reaches a value equal to its maximum voltage. Then, the battery is charged with a constant voltage until the current reaches a value lower than $0.1C$. At this moment, it is considered that the battery is completely charged. Figure F.4 shows how the 602030 Lithium polymer battery from Bullith is first charged at $1C$ until it reaches its maximum voltage of 2.8 V and then it is charged at this voltage until the charge current is equal to 7.5 mA. The figure also shows the discharge curve of the voltage on the battery when the discharge current is 75 mA.

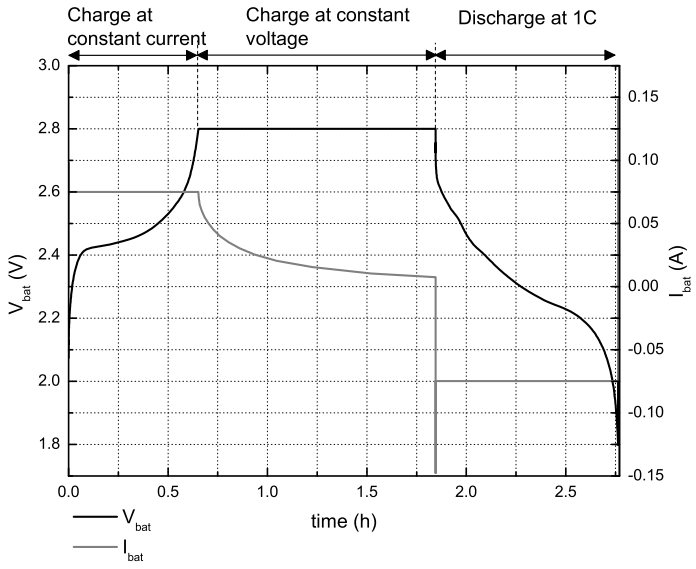

Figure F.4: Li-Ion battery charging and discharging stages.

Figures F.5 and F.6 show the measured discharging characteristics with different curves, each one with a different discharge current value ($2C$, $1C$ and $0.5C$), of the battery voltage as a function of the nominal capacity at 20 °C for two different batteries. Figure F.7 shows two different curves of voltage as a function of nominal capacity for $2C$ and $1C$ discharge current at 0 °C.

The Bullith battery is charged with $1C$ in the temperature chamber at 20 °C. A discharge profile is configured to discharge the battery with every pulse at different discharge currents and obtain several points of the parameters as a function of the state of charge. It is necessary to assure that the relaxation time is at least equal to the slow time constant value to obtain an appropriate fitting. Also, during a time at least equal to the fast time constant it is necessary to store enough data in order to be able to realize the fitting process. Some of the results obtained are shown in Figures F.8 and F.9.

From the analysis of the electrical battery model of Figure F.1, it is deduced Equation (F.5). The fitting process is realized employing Matlab [138] and the EasyFit toolbox [139] employing a known expression, that contains a voltage drop and two exponential expressions where the coefficients have to be calculated. The results obtained are shown from Figure F.10 to Figure F.15 with different discharge currents at 20 °C as a function of the state of charge of the battery.

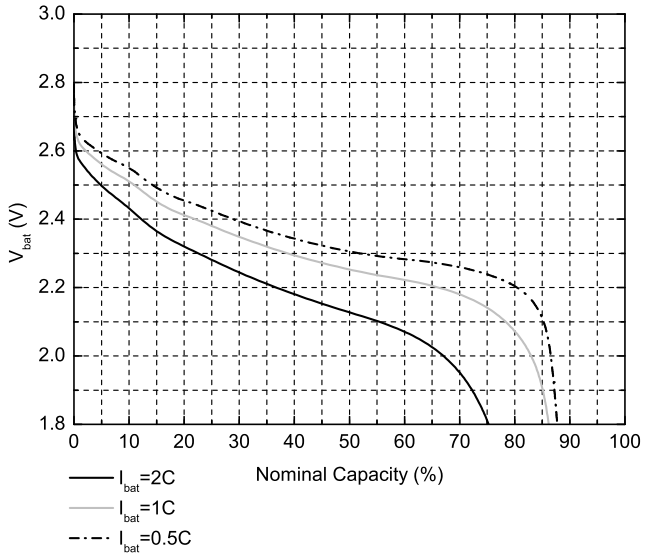

Figure F.5: Capacity that can be extracted from one battery sample at 20 °C.

$$V_{bat} = V_{oc} + I_{bat}R_{series} + I_{bat}R_{tran_S}\left(e^{-t/\tau_{tran_S}} - 1\right) + I_{bat}R_{tran_L}\left(e^{-t/\tau_{tran_L}} - 1\right) \quad \text{(F.5)}$$

The open circuit voltage of the battery, V_{oc}, as a function of the state of charge of the battery is shown in Figure F.10. Six different waveforms from two different batteries are represented with discharge current values of $2C$, $1C$ and $0.5C$. When the state of charge of the battery decreases, the open circuit voltage also decreases. Figure F.11 shows the series resistance of the battery as a function of its state of charge. The series resistance is almost constant from state of charge 0.9 to 0.2. R_{tran_S} as a function of the state of charge is displayed in Figure F.12 with an approximately constant value from a state of charge of 0.1 to fully charge and a similar value for all the discharge currents under consideration.

Figure F.13 shows R_{tran_L} versus the state of charge. The value of this component is almost constant from a state of charge of 0.4 to 0.9 for the different discharge currents and batteries used. Nevertheless, this value is not approximately equal for the different discharge currents and batteries.

Figures F.14 and F.14 show the response of C_{tran_S} and C_{tran_L} versus the

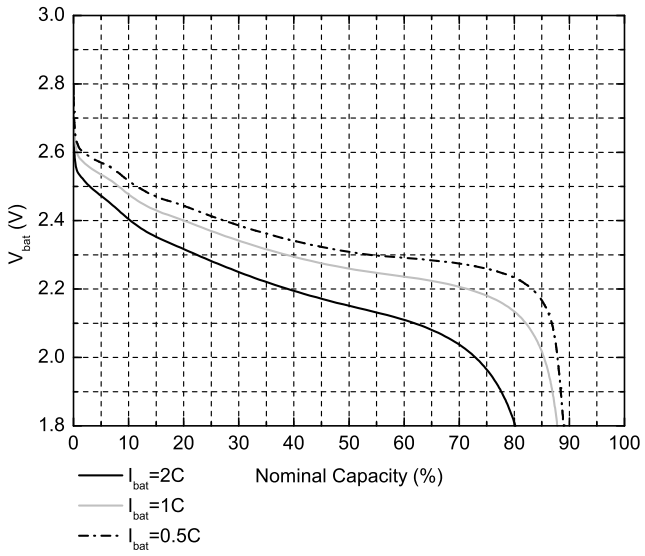

Figure F.6: Capacity that can be extracted from one battery sample at 20 °C.

state of charge of the battery. The value of these two components of the electrical model of the battery depends strongly on the discharge current employed.

This measurements allow to create a Verilog-A model for this battery that can be employed in energy harvesting system simulations like the ones done in Chapters 6 and 13 allowing to have realistic simulations and predict which is the minimum capacity of the battery and which is its minimum state of charge.

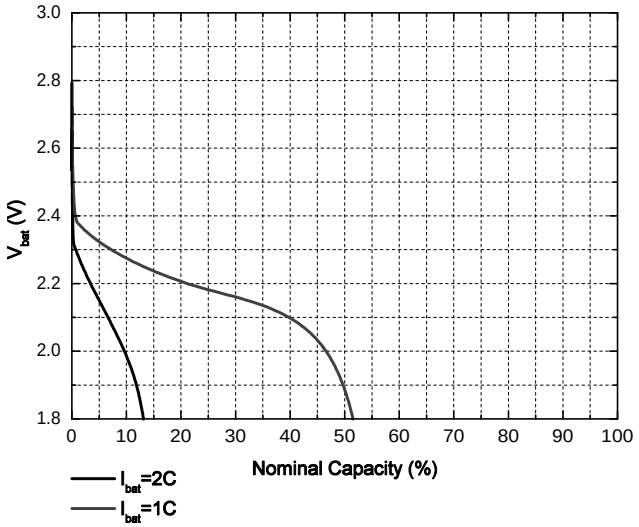

Figure F.7: Capacity that can be extracted from one battery sample at 0 °C.

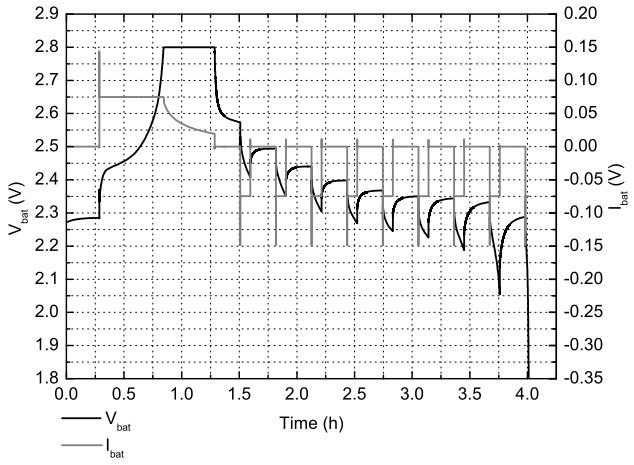

Figure F.8: Battery voltage and current during charge stage and discharge pulses at $1C$.

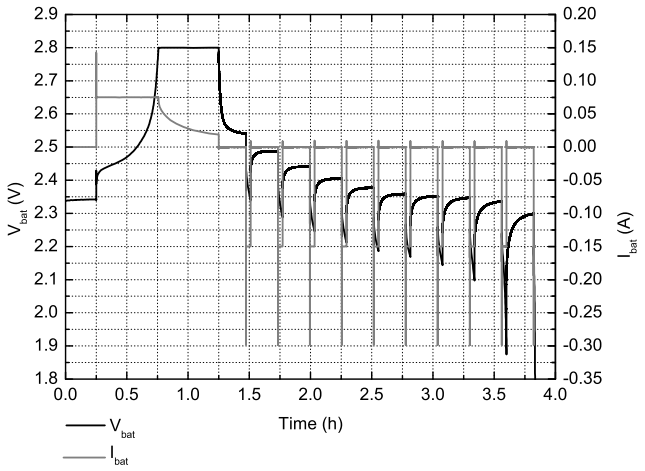

Figure F.9: Battery voltage and current during charge stage and discharge pulses at $2C$.

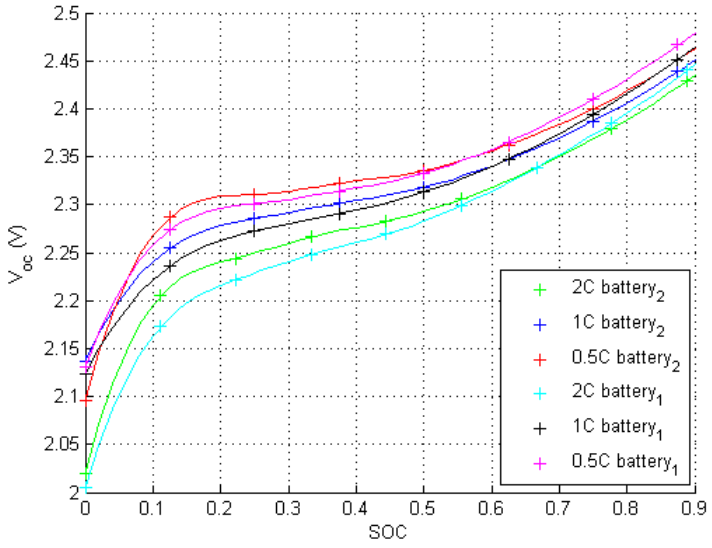

Figure F.10: V_{oc} extracted parameter for the Bullith lithium battery 602030 at 20 °C.

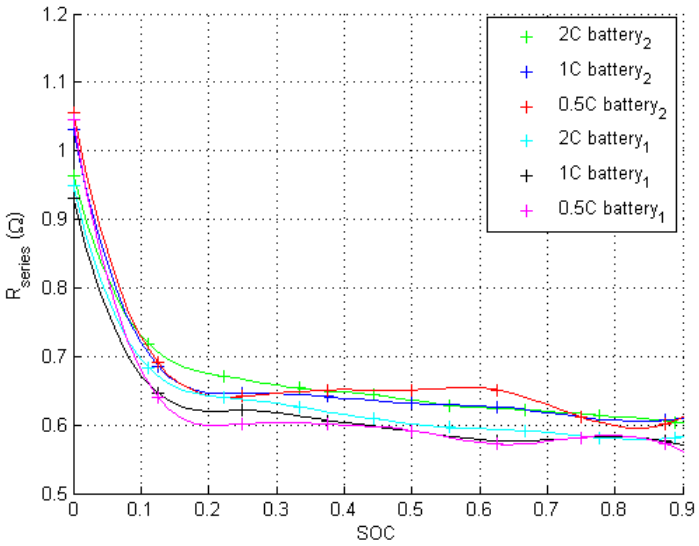

Figure F.11: R_{series} extracted parameter for the Bullith lithium battery 602030 at 20 °C.

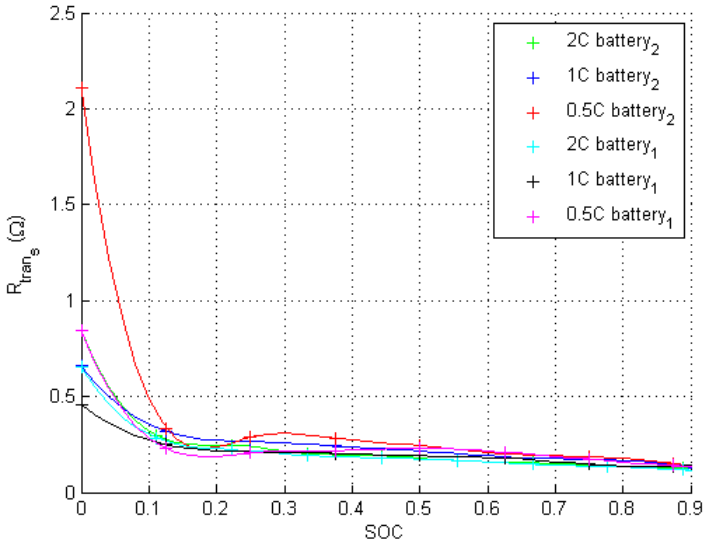

Figure F.12: R_{trans} extracted parameter for the Bullith lithium battery 602030 at 20 °C.

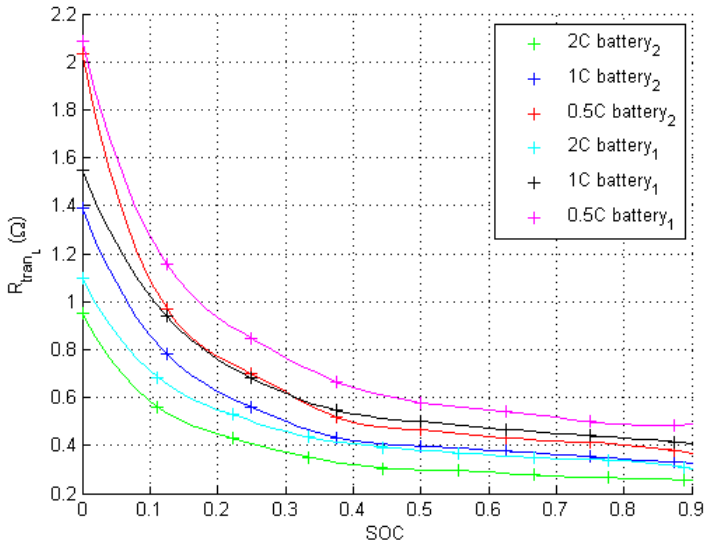

Figure F.13: R_{tran_L} extracted parameter for the Bullith lithium battery 602030 at 20 °C.

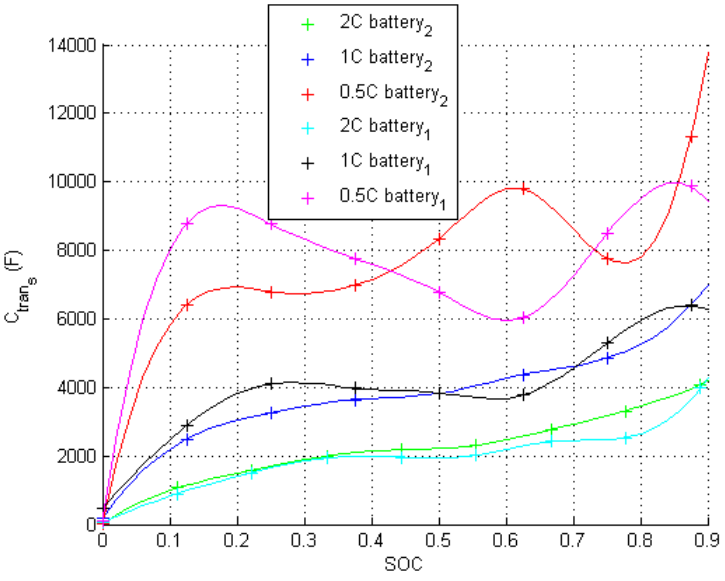

Figure F.14: C_{trans} extracted parameter for the Bullith lithium battery 602030 at 20 °C.

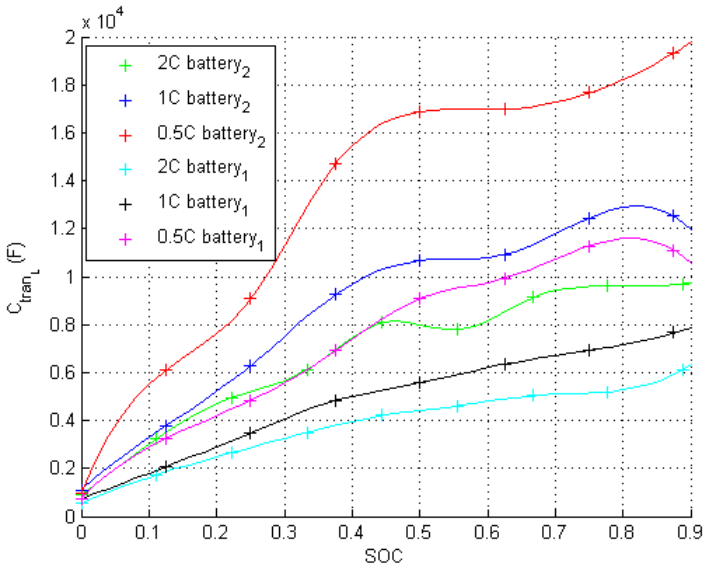

Figure F.15: C_{tran_L} extracted parameter for the Bullith lithium battery 602030 at 20 °C.

Bibliography

[1] J. A. Chavez, J. A. Ortega, J. Salazar, A. Turo, and M. J. Garcia, ""SPICE model of thermoelectric elements including thermal effects"," *Instrumentation and Measurement Technology Conference, 2000. IMTC 2000. Proceedings of the 17th IEEE*, vol. 2, pp. 1019–1023, May 2000.

[2] S. Lineykin and S. Ben-Yaakov, ""SPICE compatible equivalent circuit of the energy conversion processes in thermoelectric modules"," *Electrical and Electronics Engineers in Israel, 2004. Proceedings. 2004 23rd IEEE Convention of*, pp. 346–349, September 2004.

[3] M. Chen and G. Rincón-Mora, "Accurate electrical battery model capable of predicting runtime and I-V performance," *IEEE Transactions on Energy Conversion*, vol. 21, no. 2, pp. 504–511, June 2005.

[4] T. Starner, "The challenges of wearable computing: Part 1," *Micro, IEEE*, vol. 21, no. 4, pp. 44–52, 2001.

[5] ——, "The challenges of wearable computing: Part 2," *Micro, IEEE*, vol. 21, no. 4, pp. 54–67, 2001.

[6] T. Zimmerman, "Personal area networks (PAN): Near-field intra-body communication," Master's thesis, Massachusetts Institute of Technology, September 1995.

[7] ——, "Personal area networks: Near-field intrabody communication," *IBM Systems Journal*, vol. 35, no. 3&4, pp. 609–617, 1996.

[8] F. Gesellschaft, Body Area Network. [Online]. Available: http://www.ban.fraunhofer.de/

[9] P. Lukowicz, H. Junker, M. Stäger, T. von Büren, and G. Tröster, "WearNET: A Distributed Multi-Sensor System for Context Aware Wearables," in *Proceedings of the 4th International Conference on Ubiquitous Computing, Ubicomp 2002*, September 2002, pp. 361–370.

[10] I. Oppermann, L. Stoica, A. Rabbachin, Z. Shelby, and J. Haapola, "Uwb wireless sensor networks: Uwen - a practical example," *IEEE Communications Magazine*, vol. 42, no. 12, pp. S27–S32, 2004.

[11] S. Roundy, E. Leland, J. Baker, E. Carleton, E. Reilly, E. Lai, B. Otis, J. Rabaey, P. Wright, and V. Sundararajan, "Improving power output for vibration-based energy scavengers," *Pervasive Computing, IEEE*, vol. 4, no. 1, pp. 28–36, 2005.

[12] S. Roundy, P. K. Wright, and J. M. Rabaey, *Energy scavenging for wireless sensor networks with special focus on vibrations.* Kluwer Academic Publishers, 2004.

[13] L. Mateu and F. Mol, "System-level simulation of a self-powered sensor with piezoelectric energy harvesting," in *Proceedings for the SENSORCOMM 2007 Conference*, Valencia, October 2007.

[14] F. Pecheux, C. Lallement, and A. Vachoux, ""VHDL-AMS and Verilog-AMS as alternative hardware description languages for efficient modeling of multidiscipline systems"," *Computer-Aided Design of Integrated Circuits and Systems, IEEE Transactions on*, vol. 24, no. 2, pp. 204–225, 2005.

[15] Ptolemy Project, http://ptolemy.eecs.berkeley.edu.

[16] Nordic Semiconductor., http://www.nvlsi.no.

[17] Enocean, http://www.enocean.com.

[18] L. Mateu and F. Moll, "Review of Energy Harvesting Techniques for Microelectronics," in *Proceedings of SPIE Microtechnologies for the new millenium*, May 2005, pp. 359–373.

[19] ——, "Optimum piezoelectric bending beam structures for energy harvesting using shoe inserts," *J. of Intelligent Material Systems and Structures*, vol. 16, no. 10, pp. 835–845, 2005.

[20] ——, "Appropriate charge control of the storage capacitor in a piezoelectric energy harvesting device for discontinuous load operation," *Sensors and Actuators A: Physical*, vol. 132, no. 1, pp. 302–310, 2006.

[21] L. Mateu, C. Villavieja, and F. Moll, "Physics-Based Time-Domain Model of a Magnetic Induction Microgenerator," *Magnetics, IEEE Transactions on*, vol. 43, no. 3, pp. 992–1001, March 2007.

[22] L. Mateu, C. Codrea, N. Lucas, M. Pollak, and P. Spies, "Human Body Energy Harvesting Thermogenerator for Sensing Applications," in *Proceedings for the SENSORCOMM 2007 Conference*, October 2007.

[23] A. Reinders, "Options for photovoltaic solar energy systems in portable products," in *proceedings of TCME 2002, Fourth International symposium*, 22-26 April 2002, pp. –.

[24] M. Veefkind and S. F. J. Flipsen, "Gathering data on the energy to be harvested with portable consumer products, method and equipment," in *Proceedings of the ISES EuroSun Congress*, 2004, pp. –.

[25] M. Veefkind, "Industrial design and PV-power, challenges and barrieres," in *Proceedings of the ISES Solar World Congress*, 2003, pp. –.

[26] k. Lin, J. Yu, J. Hsu, S. Zahedi, D. Lee, J. Friedman, A. Kansal, V. Raghunathan, and M. Srivastava, "Demo abstract: Heliomote: Enabling long-lived sensor networks through solar energy harvesting," in *In Proceedings of ACM SenSys 2005*, November 2005.

[27] ATA LABS. [Online]. Available: http://atlalabs.com/

[28] E. de Benito, ""inventores españoles desarrollan un marcapasos solar"," *El País*, September 2004.

[29] P. Fairley, "Solar-cell rollout," *Technology Review*, pp. 35–40, July-August 2004.

[30] A. Kansal, J. Hsu, S. Zahedi, and M. B. Srivastava, "Power management in energy harvesting sensor networks," Networked and Embedded Systems Laboratory, UCLA, Tech. Rep. TR-UCLA-NESL-200603-02, 2006. [Online]. Available: http://nesl.ee.ucla.edu/fw/kansal/kansal_tecs.pdf

[31] P. D. Mitcheson, T. C. Green, E. M. Yeatman, and A. S. Holmes, ""Architectures for vibration-driven micropower generators"," *J. of Microelectromechanical Systems*, vol. 13, no. 3, June 2004.

[32] C. V. C. Bouten, K. T. M. Koekkoek, M. Verduin, R. Kodde, and J. D. Janssen, "A triaxial accelerometer and portable data processing unit for the assessment of daily physical activity," *IEEE Trans. on Biomedical Engineering*, vol. 44, no. 3, pp. 136–147, March 1997.

[33] C. Williams, C. Shearwood, M. Harradine, P. Mellor, T. Birch, and R. Yates, "Development of an electromagnetic micro-generator," *Circuits, Devices and Systems, IEE Proceedings*, vol. 148, no. 6, pp. 337–342, December 2001.

[34] W. Li, Z. Wen, P. Wong, G. Chan, and P. Leong, "A micromachined vibration-induced power generator for low power sensors of robotic systems," in *Proceedings of Eight International Symposium on Robotics with Applications*, June 2000, pp. 16–21.

[35] N. N. H. Ching, G. M. H. Chan, W. J. Li, H. Y. Wong, and P. H. W. Leong, "PCB integrated micro generator for wireless systems," in *Intl. Symp. on Smart Structures and Microsystems*, 19-21 October 2000.

[36] R. Amirtharajah and A. Chandrakasan, "Self-powered low power signal processing," in *Proceedings of the Symposium on VLSI Circuits Digest of Technical Papers*, 1997.

[37] S. Yuen, J. Lee, W. Li, and P. Leong, "An AA-sized vibration-based microgenerator for wireless sensors," *IEEE Pervasive Computing*, vol. 6, no. 1, pp. 64–72, January-March 2007.

[38] S. Meninger, J. Mur-Miranda, R. Amirtharajah, A. P. Chandrasakan, and J. H. Lang, "Vibration to electric energy conversion," *IEEE Trans. on VLSI*, vol. 9, no. 1, February 2001.

[39] S. Roundy, P. Wright, and J. Rabaey, "A study of low level vibrations as a power source for wireless sensor nodes," *Computer Communications*, vol. 26, no. 11, pp. 1131–1144, 2003.

[40] S. Roundy, B. P. Otis, Y.-H. Chee, J. M. Rabaey, and P. Wright, "A 1.9 ghz rf tansmit beacon using environmentally scavenged energy," in *Proceedings of the ISPLED 2003*, 2003.

[41] S. Roundy, P. Wright, and K. Pister, "Micro-electrostatic vibration-to-electricity converters," in *Proceedings of ASME International Mechanical Engineering Congress and Exposition IMECE2002*, vol. 220, November 2002, pp. 17–22.

[42] T. Sterken, K. Baert, R. Puers, and S. Borghs, "Power extraction from ambient vibration," in *Proceedings of the Workshop on Semiconductor Sensors*, Nov. 2002, pp. 680–683.

[43] M. Miyazaki, H. Tanaka, T. N. G. Ono, N. Ohkubo, T. Kawahara, and K. Yano, "Electric-energy generation using variable-capacitive resonator for power-free lsi: efficiency analysis and fundamental experiment," in *Proceedings of the ISLPED 03*, 25-27 August 2003, pp. 193–198.

[44] H. Hu, H. Xue, and Y. Hu, "A spiral-shaped harvester with an improved harvesting element and an adaptive storage circuit," *IEEE Transactions on Ultrasonics, Ferroelectrics and Frequency Control*, vol. 54, no. 6, pp. 1177–1187, June 2007.

[45] G. Ottman, H. Hofmann, A. Bhatt, and G. Lesieutre, "Adaptive piezoelectric energy harvesting circuit for wireless remote power supply," *IEEE Trans. on Power Electronics*, vol. 17, no. 2, pp. 669–676, September 2002.

[46] G. Ottman, H. Hofmann, and G. Lesieutre, "Optimized piezoelectric energy harvesting circuit using step-down converter in discontinuous conduction mode," *IEEE Trans. on Power Electronics*, vol. 18, no. 2, pp. 696–703, March 2003.

[47] P. Mitcheson, T. Green, and E. Yeatman, "Power processing circuits for electromagnetic, electrostatic and piezoelectric inertial energy scavengers," *Microsystem Technologies*, vol. 13, no. 11, pp. 1629–1635, 2007.

[48] B. Stark, P. Mitcheson, P. Miao, T. Green, E. Yeatman, and A. Holmes, "Power processing issues for micro-power electrostatic generators," in *Power Electronics Specialists Conference, 2004.PESC 04.2004 IEEE 35th Annual*, vol. 6, 2004, pp. 4156–4162.

[49] S. Angrist, *Direct Energy Conversion*. Allyn & Bacon, 1982.

[50] Thermoelectrics.com, http://www.thermoelectrics.com.

[51] M. A. Ryan and J.-P. Fleurial, "Where there is heat, there is a way. thermal to electric power conversion using thermoelectric microconverters," *The Electromechanical Society Interface*, vol. 11, no. 2, pp. 30–33, 2002.

[52] T. Starner, ""Human-powered Wearable Computing"," *IBM Systems Journal*, vol. 35, no. 3&4, 1996.

[53] V. Leonov and P. Fiorini, "Thermal Matching of a Thermoelectric Energy Scavenger with the Ambience," in *Proceedings of the 5th European Conference on Thermoelectrics*, September 2007.

[54] V. Leonov, T. Torfs, P. Fiorini, and C. Van Hoof, "Thermoelectric Converters of Human Warmth for Self-Powered Wireless Sensor Nodes," *Sensors Journal, IEEE*, vol. 7, no. 5, pp. 650–657, 2007.

[55] D.T.S. GmbH, http://www.dts-generator.com.

[56] M. Stordeur and I. Stark, "Low power thermeoelctric generator - self-sufficient energy supply for micro systems," in *Proceedings of the 16th International Conference on Thermoelectrics*, 1997, pp. 575–577.

[57] I. Stark and M. Stordeur, "'new micro thermoelectric devices based on bismuth telluride-type thin solid films'," in *Proceedings of the 18th International Conference on Thermoelectronics*, 1999, pp. 465–472.

[58] J. Stevens, "Optimized thermal design of small δt thermoelectric generators," in *Proceedings of the 34th Intersociety Energy Conversion Engineering Conference*, 1999.

[59] Seiko Instruments Inc., http://www.sii.co.jp/info/eg/thermic_main.html.

[60] M. Kishi, H. Nemoto, T. Hamao, M. Yamamoto, S. Sudou, M. Mandai, and S. Yamamoto, "Micro thermoelectric modules and their application to wristwatchesas an energy source," *Thermoelectrics, 1999. Eighteenth International Conference on*, pp. 301–307, 1999.

[61] I. Stark, "Thermal energy harvesting with thermo life," in *Proceedings of the International Workshop on Wearable and Implantable Body Sensor Networks (BSN'06)*, 2006.

[62] C. Tsui, H. Shao, W. Ki, and F. Su, "Ultra-low voltage power management circuit and computation methodology for energy harvesting applications," *Proceedings of the 2006 conference on Asia South Pacific design automation*, pp. 96–97, 2006.

[63] J. Damaschke, "Design of a low-input-voltage converter for thermoelectric-generator," *Industry Applications, IEEE Transactions on*, vol. 33, no. 5, pp. 1203–1207, 1997.

[64] B. Strassner and K. Chang, "A circularly polarized rectifying antenna array for wireless microwave power transmission with over 78% efficiency," in *Microwave Symposium Digest, 2002 IEEE MTT-S International*, vol. 3, 2–7 June 2002, pp. 1535–1538.

[65] J. Hagerty, F. Helmbrecht, W. McCalpin, R. Zane, and Z. Popovic, "Recycling ambient microwave energy with broad-band rectenna arrays," *IEEE Transactions on microwave theory and techniques*, vol. 52, no. 3, March 2004.

[66] A. Lal and J. Blanchard, "The daintiest dynamos," *IEEE Spectrum*, vol. 41, no. 9, pp. 36–41, September 2004.

[67] T. Jones, "Triboelectric charging common objects," 2004, http://www.ece.rochester.edu/ jones/demos/charging.html.

[68] V. Kaajakari and A. Lal, "Electrostatic batch assembly of surface MEMS using ultrasonictriboelectricity," in *Micro Electro Mechanical Systems, 2001. MEMS 2001. The 14th IEEE International Conference on*, 2001, pp. 10–13.

[69] Berkeley mica motes, http://www.xbow.com.

[70] Berkeley Operating System for motes, http://www.btinyos.net.

[71] *Advances in Human-Powered Energy Systems in Consumer Products.* INTERNATIONAL DESIGN CONFERENCE - DESIGN 2004, 18-21 May 2004.

[72] A. Applewhite, "It takes a village," *IEEE Spectrum*, pp. 40–45, September 2003.

[73] Windstream Power Systems Inc., http://www.windstreampower.com/.

[74] J. Drake, "The greatest shoe on earth," *wired*, vol. 9, no. 02, pp. 90–100, Feb. 2001.

[75] R. J. Kuipers, "Engineering a human powered mp3 player," Master's thesis, Delft University of Technology, 2003.

[76] Freeplay, http://www.freeplayenergy.com/.

[77] A. Stevels and A. J. Jansen, ""Renewable energy in portable radios: an environmental benchmarking study"," *The Journal of Sustainable Product Design*, January 1998.

[78] Atkin Design and Development Ltd., http://www.atkin.info.

[79] T. Starner, "Wearable computing for the developing world," *Pervasive Computing, IEEE*, vol. 4, no. 3, pp. 87–91, 2005.

[80] T. Starner and J. Paradiso, "Human generated power for mobile electronics," in *Low-Power Electronics*, C. Piguet, Ed. CRC Press, 2005, no. 45, pp. –.

[81] F. Moll and A. Rubio, "An approach to the analysis of wearable body-powered systems," in *Mixed Signal Design Workshop*, June 2000.

[82] N. S. Shenck, "A demonstration of useful electric energy generation from piezoceramics in a shoe," Master's thesis, Massachussets Institute of Technology, 1997.

[83] N. Shenck and J. Paradiso, "Energy scavenging with shoe-mounted piezoelectrics," *Micro, IEEE*, vol. 21, no. 3, pp. 30–42, 2001.

[84] R. Pelrine, R. Kornbluh, Q. Pei, and J. Joseph, "High-speed electrically actuated elastomers with strain greater than 100%," *Science Magazine*, vol. 287, pp. 836–839, February 2000.

[85] S. Ashley, "Artificial muscles," *Scientific American*, vol. 289, no. 4, pp. 52–59, October 2003.

[86] J. Kymissis, C. Kendall, J. Paradiso, and N. Gershenfeld, "Parasitic power harvesting in shoes," in *Second IEEE International Conference on Wearable Computing*, 1998, pp. 132–139.

[87] J. Y. Hayashida, "Unobtrusive integration of magnetic generator systems into common footwear," Master's thesis, Massachusetts Institute of Technology, 2000.

[88] T. von Büren, P. Mitcheson, T. Green, E. Yeatman, A. Holmes, and G. Troster, "Optimization of inertial micropower Generators for human walking motion," *Sensors Journal, IEEE*, vol. 6, no. 1, pp. 28–38, 2006.

[89] J. Paradiso, "Renewable energy sources for the future of mobile and embedded computing," in *Invited talk given at the Intel Computing Continuum Conference, San Francisco, California.*

[90] Thermo Life Energy Corp. [Online]. Available: http://www.poweredbythermolife.com/

[91] V. Pop, H. Bergveld, P. Notten, and P. Regtien, "State-of-the-art of battery state-of-charge determination," *Measurement Science and Technology*, vol. 16, pp. R93–R110(1), December 2005.

[92] Z. Chen, "High pulse power system through engineering battery-capacitor combination," vol. 2, 2000, pp. 752–755.

[93] Battery University, http://www.batteryuniversity.com/parttwo-55.htm.

[94] D. Linden and T. Reddy, *Handbook of Batteries*. 3rd ed. McGraw-Hill, 2001, vol. 3.

[95] M. D. Semiconductor, "Application note 131. lithium-ion cell fuel gauging with dallas semiconductor battery monitor ics." Maxim Dallas Semiconductor" Application Note, March 2001.

[96] S. Davis, "Battery power management: Optimal battery performance calls for different soulutions in different applications," June 2004. [Online]. Available: http://electronicdesign.com/Files/29/8079/8079_01.pdf

[97] S. Park, A. Savvides, and M. Srivastava, "Battery capacity measurement and analysis using lithium coin cell battery." ACM Press New York, NY, USA, 2001, pp. 382–387.

[98] Y.-S. Hwang, S.-C. Wang, F.-C. Yang, and J.-J. Chen, "New compact cmos li-ion battery charger using charge-pump technique for portable applications," *IEEE Transactions on Circuits and Systems- I: Regular Papers*, vol. 54, no. 4, pp. 705–712, April 2007.

[99] I. Buchmann, *Batteries in a portable world; a handbook on rechargeable batteries for non-engineers*. Burnaby: Cadex Electronics, 1997.

[100] P. Barrade, "Energy storage and applications with supercapacitors," 2003.

[101] M. Rossi, *Acoustics and Electroacoustics*. Norwood, MA: Artech House, Inc., 1988.

[102] S. Platt, S. Farritor, and H. Haider, "On low-frequency electric power generation with pzt ceramics," *Mechatronics, IEEE/ASME Transactions on*, vol. 10, no. 2, pp. 240–252, April 2005.

[103] A. D. Aguil, "Sistema d'adquisici d'ones generades per lmines piezoelctriques al caminar," Master's thesis, ETS Enginyeria de Telecomunicaci, UPC, May 2007.

[104] *Piezo Film Sensors Technical Manual*, Measurement Specialities, http://www.msiusa.com.

[105] S. Roundy, "Energy scavenging for wireless sensor nodes with a focus on vibration to electricity conversion," Ph.D. dissertation, niversity of California, 2003.

[106] W. Li, T. Ho, G. Chan, P. Leong, and H. Y. Wong, ""Infrared signal transmission by a laser-micromachined, vibration-induced power generator"," in *Circuits and Systems, 2000. Proceedings of the 43rd IEEE Midwest Symposium on*, vol. 1, 2000, pp. 236–239 vol.1.

[107] T. von Büren, P. Mitcheson, T. Green, E. Yeatman, A. Holmes, and G. Troster, ""Optimization of inertial micropower Generators for human walking motion"," *Sensors Journal, IEEE*, vol. 6, no. 1, pp. 28–38, 2006.

[108] R. Amirtharajah and A. Chandrakasan, "Self-powered signal processing using vibration-based power generation," *Solid-State Circuits, IEEE Journal of*, vol. 33, no. 5, pp. 687–695, 1998.

[109] "Adxl202 low-cost *pm*2g dual-axis accelerometer with duty cycle output," October 2000. [Online]. Available: http://www.analog.com/en/prod/0,2877,ADXL202,00.html

[110] J. Matson, "Application note - calibrating the adxl210 accelerometer," Tech. Rep., December 1999.

[111] P. Lukowicz, H. Junker, and G. Troster, "Automatic calibration of body worn acceleration sensors," *Proceedings of the second international Pervasive Computing conference*, pp. 176–181, 2004.

[112] A. Krohn, M. Beigl, C. Decker, U. Kochendorfer, P. Robinson, and T. Zimmer, "Inexpensive and Automatic Calibration for Acceleration Sensors," *LECTURE NOTES IN COMPUTER SCIENCE*, vol. 3598, p. 245, 2005.

[113] Thermoelectrics.com, http://www.thermoelectrics.com/introduction.htm.

[114] D. Mitrani, J. Tome, J. Salazar, A. Turo, M. Garcia, and J. Chavez, "Methodology for extracting thermoelectric module parameters," *Instrumentation and Measurement, IEEE Transactions on*, vol. 54, no. 4, pp. 1548–1552, August 2005.

[115] S. Lineykin and S. Ben-Yaakow, "Analysis of thermoelectric coolers by a spice-compatible equivalent-circuit model," *IEEE Power Electronics Letters*, vol. 3, no. 2, pp. 63–66, June 2005.

[116] Peltron GmbH Peltier-Technik, http://www.peltron.de.

[117] "Texas instruments," http://www.ti.com/.

[118] L. Mateu, C. Codrea, N. Lucas, M. Pollak, and P. Spies, "Energy Harvesting for Wireless Communication Systems Using Thermogenerators," in *Proceedings of the XXI Conference on Design of Circuits and Integrated Systems (DCIS)*, november 2006.

[119] L. Mateu, M. Pollak, and P. Spies, "Electrical characterization of a piezoelectric film-based power generator for autonomous wearable devices," in *Procedings of the PowerMEMS Conference*, November 2007.

[120] T. Torfs, V. Leonov, C. Van Hoof, and B. Gyselinckx, "Body-Heat Powered Autonomous Pulse Oximeter," in *Sensors, 2006. 5th IEEE Conference on*, October 2007, pp. 427–430.

[121] V. Leonov, T. Torfs, N. Kukhar, C. V. Hoof, and R. Vullers, "Small-size BiTe Thermopiles and a Thermoelectric Generator for Wearable Sensor Nodes," in *Proceedings of the 5th European Conference on Thermoelectrics*, September 2007.

[122] Sanyo Eneloop Ready to use Rechargeable Battery, http://www.eneloop.info.

[123] Bullith Batteries, http://www.bullith.de.

[124] A. Kansal, D. Potter, and M. B. Srivastava, "Performance aware tasking for environmentally powered sensor networks," in *SIGMETRICS '04/Performance '04: Proceedings of the joint international conference on Measurement and modeling of computer systems.* New York, NY, USA: ACM Press, 2004, pp. 223–234.

[125] Advanced Linear Devices, Inc., http://www.aldinc.com.

[126] NXP founded by Philips, http://www.nxp.com/pip/BSH105.html.

[127] A. Omole, "Analysis, Modeling and Simulation of Optimal Power Tracking of Multiple-Modules of Paralleled Solar Cell Systems," Master's thesis, Florida State University, College of Engineering, 2006.

[128] Y. Lim and D. Hamill, "Simple maximum power point tracker for photovoltaic arrays," *Electronics Letters*, vol. 36, no. 11, pp. 997–999, 2000.

[129] C. Villavieja, I. Gelado, N. Navarro, M. Gil, L. Mateu, F. Martorell, and F. Moll, "Experimental Runtime Power Consumption Measurements in WSN," in *Proceedings of the UCAMI*, vol. 5, 2005.

[130] T. Ikeda, *Fundamentals of Piezoelectricity.* Oxford: Oxford Science Publications, 1990.

[131] A. Moulson and J. Herbert, *Electroceramics. Materials Properties Applications.* London: Chapman & Hall, 1997.

[132] A. Jacquot, "Bilder vom thg-aufbau," 2006.

[133] M. D. Semiconductor, "Inaccuracies of estimating remaining cell capacity with voltage measurements alone," Maxim Dallas Semiconductor," Application Note, April 2001.

[134] B. Schweighofer, K. Raab, and G. Brasseur, "Modeling of high power automotive batteries by the use of an automated test system," *Instrumentation and Measurement, IEEE Transactions on*, vol. 52, no. 4, pp. 1087–1091, 2003.

[135] S. Buller, M. Thele, R. De Doncker, and E. Karden, "Impedance-based simulation models of supercapacitors and Li-ion batteries for power electronic applications," *Industry Applications, IEEE Transactions on*, vol. 41, no. 3, pp. 742–747, 2005.

[136] Z. Salameh, M. Casacca, and W. Lynch, "A mathematical model for lead-acid batteries," *Energy Conversion, IEEE Transactions on*, vol. 7, no. 1, pp. 93–98, 1992.

[137] Clima Temperatur Systeme CTS, http://www.cts-umweltsimulation.de.

[138] The MathWorks, http://www.mathworks.com/.

[139] EasyFit:: Distribution Fitting Made Easy, http://www.mathwave.com/products/easyfit.html.